The Dissertation Committee for Morgan Cole Williamson Certifies that this is the approved version of the following Dissertation:

Electrical Bias Driven Effects for Spintronic Applications:

Ferromagnetic and Antiferromagnetic Materials

Committee:

Maxim Tsoi, Supervisor

Alex Demkov

John Markert

Elaine Li

Jianshi Zhou

Electrical Bias Driven Effects for Spintronic Applications:

Ferromagnetic and Antiferromagnetic Materials

by

Morgan Cole Williamson

Dissertation

Presented to the Faculty of the Graduate School of

The University of Texas at Austin

in Partial Fulfillment

of the Requirements

for the Degree of

Doctor of Philosophy

The University of Texas at Austin

May 2019

Το Λόγος: The Rejected Cornerstone

Acknowledgements

First, I would like to thank my advisor Dr. Tsoi for his dedication to my progress as a graduate student and the substantial time he has spent with me sharing his disciplined approach to scientific investigation. I wish to thank our collaborators, including Drs. J. P. Wang, Weigang Wang, Gang Cao, and Jianshi Zhou for providing many excellent samples. I also extend thanks to my committee for graciously agreeing to attend my defense. I appreciate having been able to share this time in graduate school with my colleagues Shida Shen, Ashish Gangshettiwar, and Max de Rozieres. Thanks also go to my undergraduate advisor Dr. Florin who was instrumental in my admission to the UT Austin graduate school. I'd also like to thank Jack Clifford, Allan Schroeder, Kenny Schneider, Edwin Baez, and the rest of the machine shop staff who all have been very friendly and generous without fail. I also appreciate Dr. Heidi Seinige, who trained me upon my arrival in Dr. Tsoi's lab. I want to thank my dear friends including Pastor Merritt and Judge Powers at Westbank Bible Church for all the encouragement. Lastly, I'd like to thank my family for their ongoing, day by day support.

Abstract

Electrical Bias Driven Effects for Spintronic Applications:

Ferromagnetic and Antiferromagnetic Materials

Morgan Cole Williamson, PhD

The University of Texas at Austin, 2019

Supervisor: Maxim Tsoi

The ever-present demand for computing technology advancement has not only compelled progress toward the refinement of conventional CMOS routes, but has also driven new, less orthodox schemes whose advantages lie in branching out to access more of a system's degrees of freedom. Spintronics, one such alternative scheme now adopted by Intel and Samsung (among others), is being proven out for memory applications in mass production. Spintronics is a field of study that exploits electron spin as well as charge for encoding binary information. Although still using nanomagnets to store data, spintronics transcends previous hard disk drive technology by pursuing nonvolatile solid-state magnetic memory. In this work, we investigate voltage controlled magnetic anisotropy in magnetic tunnel junctions and study the transition metal oxide $Sr_3Ir_2O_7$ for use in antiferromagnetic spintronics, which aims at high speed, high density memory applications.

In the antiferromagnetic Mott insulator $Sr_3Ir_2O_7$, we study the effects of an applied bias on its transport properties. For instance, we demonstrate that the bias can produce changes in the materials' resistivity, including a reversible resistive switching, consistent

with electric field driven lattice distortions. The strong spin-orbit coupling in $Sr_3Ir_2O_7$ locking the crystal structure to the magnetic moments suggests that any structural transition is important for controlling the magnetic order of AFM devices. We use time-based measurements to study the thermal activation behavior of the resistive switching process in $Sr_3Ir_2O_7$ and acquire information about the energy barrier associated with the transition, including dependence on applied bias and temperature. We also demonstrate that the high bias switching state displays an increased noise pattern indicative of a dynamical state. Our observations support the possibility of controlling magnetic order in TMOs using electrical bias.

We also quantify the effects of VCMA in both perpendicular and in-plane MTJs using ferromagnetic resonance. In perpendicular MTJs, we observe a linear dependence of VCMA on applied voltage with a maximum virtual field of 40 mT and a saturation of the effect above 2 V. The effect of VCMA shows a quadratic dependence for in-plane MTJs with a maximum virtual field of 20 mT. With the mainstream adoption of MRAM, efforts studying VCMA and other electric field driven effects will be crucial to increasing the energy efficiency and viability of future spintronic memory devices.

Table of Contents

I N T R O D U C T I O N

SPINTRONICS

0.1 Development

The discovery of giant magnetoresistance (GMR) in 1988[1] spurred scientific investigation of a plethora of diverse physical effects and device geometries that sought to enhance the utility of magnetic memory devices. The field of study that ensued was called spintronics as a contraction of spin-based electronics.[2] As shown in Figure 0.1, it is characterized by the interconnection between a system's magnetic state and its transport properties, enabling reading by sensing the magnetic state and writing by specific transport mechanisms.[3, 4]

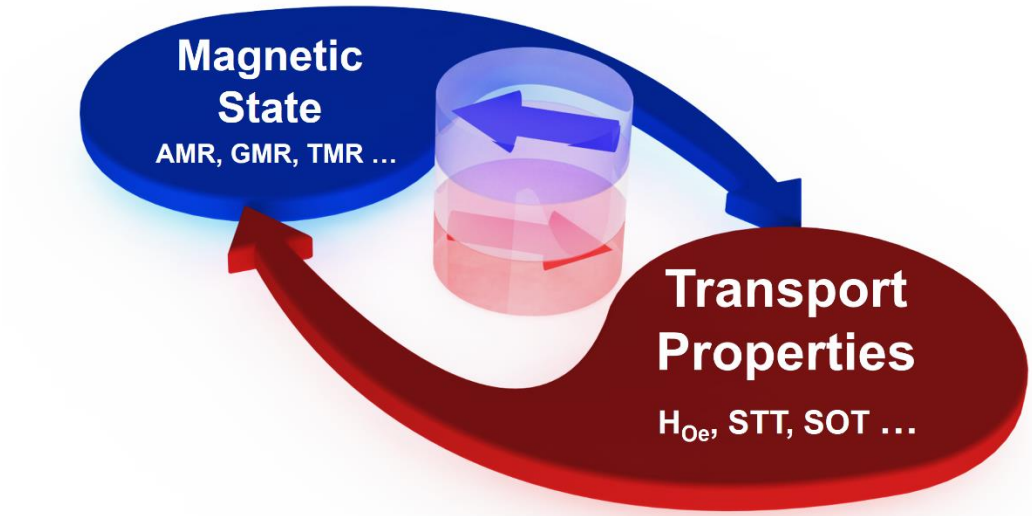

Figure 0.1: The interconnection between magnetic state and transport properties that characterizes spintronic systems (magnetic tunnel junction (MTJ) in middle) enables reading by effects such as anisotropic magnetoresistance (AMR), GMR, and tunneling magnetoresistance (TMR). Writing is implemented by transport mechanisms such Oersted fields, spin-transfer torque (STT), or spin-orbit torque (SOT).

The first significant application of GMR focused on improving the read heads in hard disk drives (HDDs). However, a more ambitious endeavor commenced afterward to forge solid-state magnetic memory, circumventing the mechanical shock vulnerabilities of the armatures in hard disk drives.[5] Spintronic devices have not only been successfully demonstrated for digital memory, but also for radio frequency (rf) applications. Solid-state magnetic memory devices are uniquely advantageous for their combination of nonvolatility and frequent rewrite applications due to their virtually unlimited write endurance. Additionally, magnetic storage, unlike charge-based storage (FLASH), is radiation-hard specifically suiting space applications. These advantages among others have prompted the adoption of spintronic embedded memory in the marketplace. Everspin Technologies,

which has been the leading company offering magnetic random access memory (MRAM) solutions, recently announced the availability of its first 28 nm 1 Gb STT-MRAM samples. Samsung is also now offering their first embedded MRAM product with 1 Gb chips expected to be production ready in late 2019. Intel is following suit by presenting their unique FinFET-based STT-MRAM products. Effects such as spin-transfer torque and voltage controlled magnetic anisotropy have sustained ongoing efforts to increase control, density, and energy efficiency of devices with significant success. Although currently in a nascent state of development, further improvements in device speed, density, and robustness are now sought using exclusively antiferromagnetic materials. Nevertheless, the driving force behind spintronics is the continually demonstrated goal of harnessing the increased latitude that spin affords for further refinement of device capability and physical understanding.

0.2 Ferromagnetic Spintronics

Magnetic Tunnel Junctions

Crucial to the manifestation of compelling solid-state magnetic memory, the magnetic tunnel junction (MTJ) is a device that has played a central role in the development of spintronics. MTJs consist of two ferromagnetic layers separated by an insulating layer thin enough to allow electron tunneling. Sourcing a probe current across the device reveals if it is in a low or high resistance state, where the low (high) resistance state is defined by the magnetizations of the two ferromagnetic layers being parallel (antiparallel).

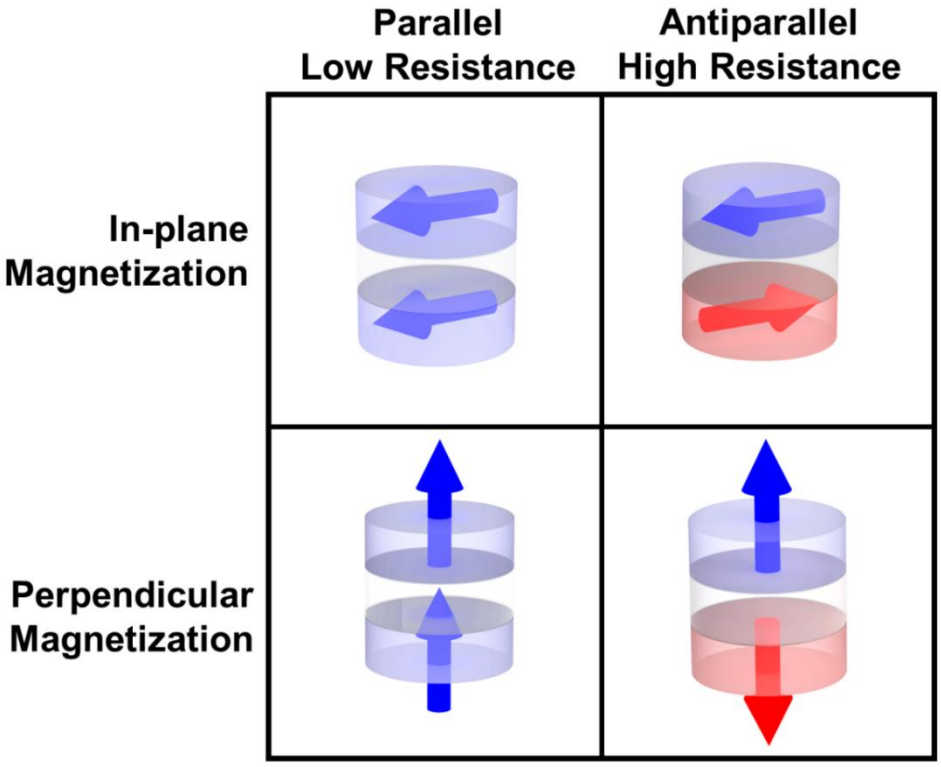

Figure 0.2: Different geometries (in-plane and perpendicular magnetization) and different resistance states (parallel and antiparallel) of dominant designs of MTJs.

The MTJ was a breakthrough that not only demonstrated the improvement of HDD read heads but also suggested the feasibility of solid-state magnetic memory due to the large discriminatory capability of representing binary digits by the MTJ's high and low resistance states (100% magnetoresistance ratio (MR), or more for specialized devices).

$$MR = \frac{R_{High} - R_{Low}}{R_{High}} \tag{0.1}$$

Spin-transfer Torque

Controlling the magnetic state of MTJ-based memory, tantamount to writing information to the cell, is an essential function of magnetic random access memory (MRAM). GMR provided the early method for reading, but a potent and efficient mechanism for writing was by no means assured. Throughout the 1990's work progressed on manifesting ever more practical MRAM with robust writing mechanisms. Early iterations of MRAM architectures relied on currents carried by proximal wires to switch the direction of the magnetization by Oersted fields, providing an effective, but inefficient means of writing to memory. However, at the turn of the millennium an exciting new mechanism was predicted and subsequently observed in magnetic multilayers: spin-transfer torque (STT).[6, 7, 8] The effect was demonstrated in precursor devices to MTJs called spin valves in which the insulating layer is replaced by a conducting nonmagnetic layer.

The advent of STT reduced the complexity of MRAM micro circuitry due to the fact that the same circuit could be used for both reading and writing, albeit with different current magnitudes. STT possesses favorable scaling qualities as the strength of the effect relies on current density, therefore the smaller devices are manufactured the more efficient they become. Figure 0.3 depicts an STT-MRAM cell architecture utilizing one transistor per MTJ.

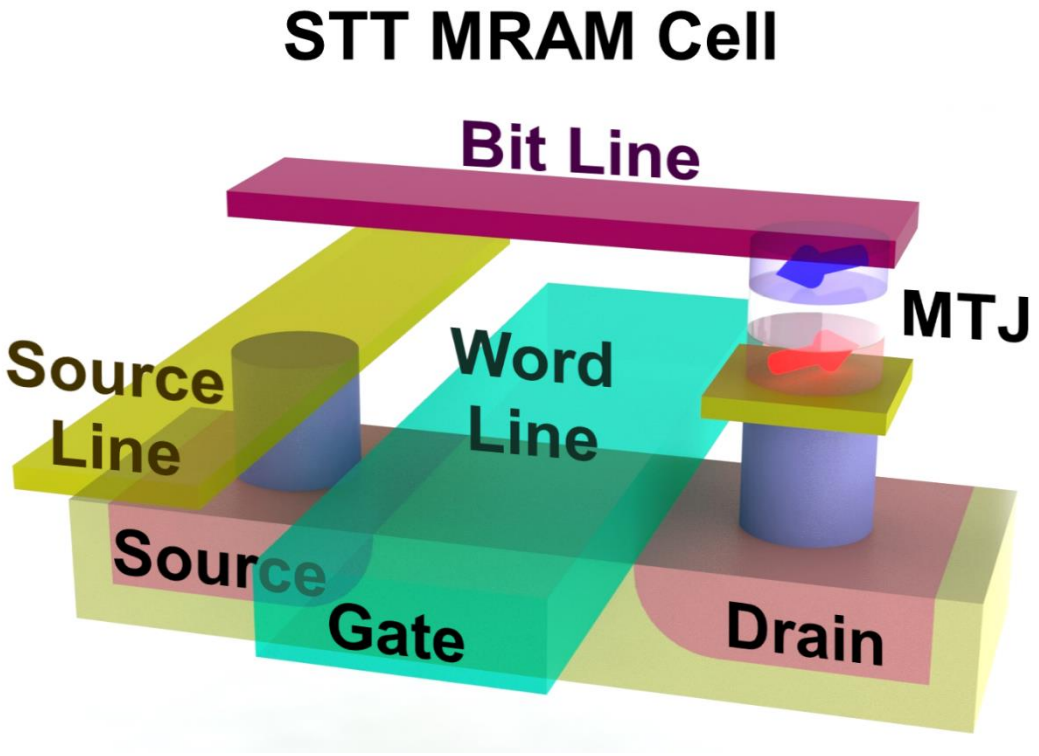

Figure 0.3: Single-MTJ-single-transistor implementation of a single MRAM cell relying on STT for writing. (Not to scale)

The spin-transfer torque effect is caused by current carrying electrons that are spin polarized by their host ferromagnetic material interacting with the magnetization of a subsequent ferromagnetic layer (typically CoFeB), often across a nonmagnetic (spin valve) or insulating (MTJ) spacer (typically MgO). Figure 0.4 shows the relevant contributors to STT, where from left to right we have an electron spin polarized along the dashed line interacting with the magnetization vector, generating the spin-transfer torque at right angles to both the current and the magnetization. In addition to STT, the spin polarized electrons also impart a field-like torque which becomes relevant when we discuss ferromagnetic resonance. The right side of Figure 0.4 shows the outgoing electron having now been spin

polarized according to its new host material, where the spin transfer torque vectors in green are equal and opposite, satisfying Newton's third law.

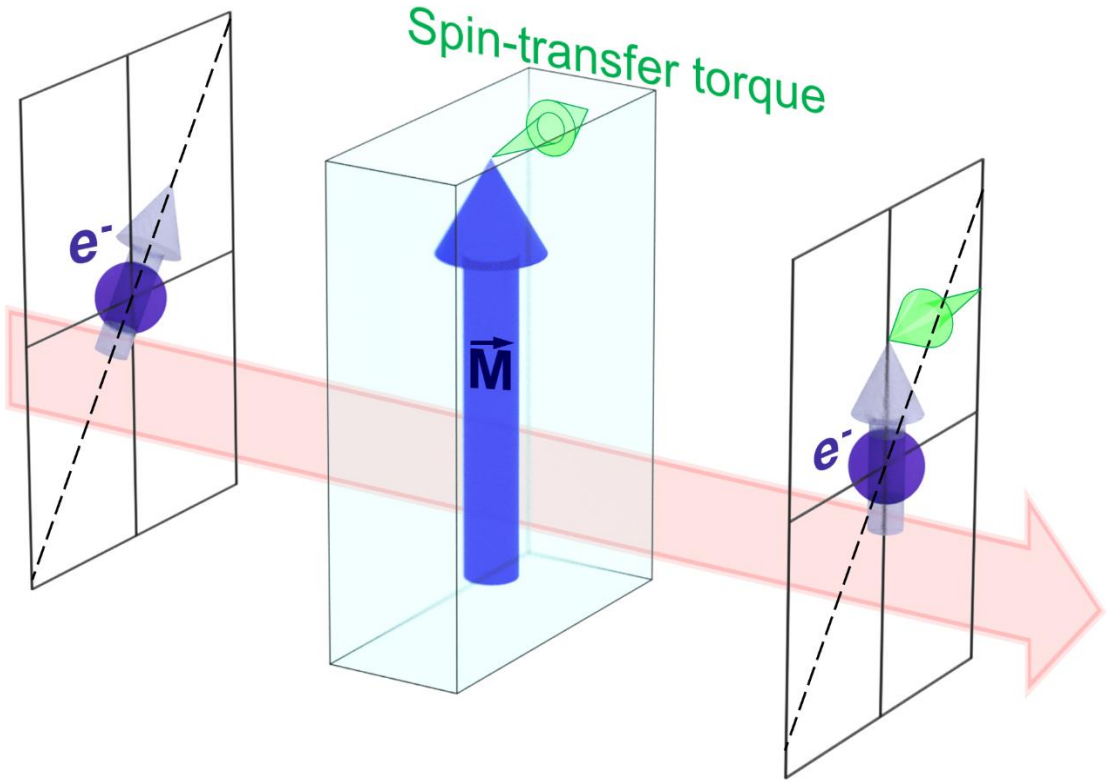

Figure 0.4: Spin-transfer torque effect is caused by incoming spin-polarized electrons (violet) interacting with the magnetization (blue) of the material in question. STT vector (green) points in a direction mutually orthogonal to current and magnetization. The outgoing electron is shown having undergone the shift in spin polarization to conform to its new host material. STT is used to tilt the magnetization of the free layer in MTJs to switch from/to high and low resistance states.

Ferromagnetic Resonance

Since the core of MRAM is about the dynamics of magnetic moments (magnetization) in MTJs, the information that would be provided by receptive measurement techniques would be key for further enhancement of spintronics. Ferromagnetic resonance, one such technique, is a powerful spectroscopic method that is able to probe the magnetization and reveal microscopic magnetic anisotropies in physical systems. FMR can be analyzed using the Landau-Lifshitz-Gilbert (LLG) equation,

$$\dot{\vec{M}} = \gamma \vec{M} \times \vec{B}_{eff} - \frac{\alpha}{M} \vec{M} \times \dot{\vec{M}} \qquad (0.2)$$

the magnetization of a material precesses about an applied magnetic field. Where the M is the magnetization, γ is the gyromagnetic ratio, B_{eff} is the local effective magnetic field, and α is a precessional damping parameter.[9] The dynamics of the LLG equation leading to ferromagnetic resonance are discussed in depth in another work by the author.[10] The practical utility of FMR has been borne out for decades in numerous enlightening studies on magnetic materials. Kittel conducted many seminal measurements using FMR partly spurred by the increase in importance of RADAR.[11] FMR is a powerful method of probing magnetic anisotropies which reveal themselves as local virtual magnetic fields in the material. Instead of using a microwave cavity for FMR excitation and a bolometer for absorption measurements as in Kittel's day, the advent of STT allowed investigators to excite and probe FMR completely electrically. The method used in this work utilizes a dc offset bias as well as an applied ac signal to electrically excite FMR. Electrical excitation and measurement enables more control and flexibility in FMR studies. Figure 0.5 depicts the geometry of FMR excitation. The blue inverted cone represents the precessional cone upon which the magnetization (blue) slides. The sum of the applied magnetic field and

virtual anisotropic fields combine to form B_{eff} about which the magnetization rotates according to the LLG equation. Additionally, non-ideal systems have a variety of effects which inject damping resulting in an excitation dissipating torque (red). The effects of current are generally composed of two orthogonal components: the spin-transfer torque (gray) and a field-like torque (magenta), so called because it acts in the same direction as an applied magnetic field.

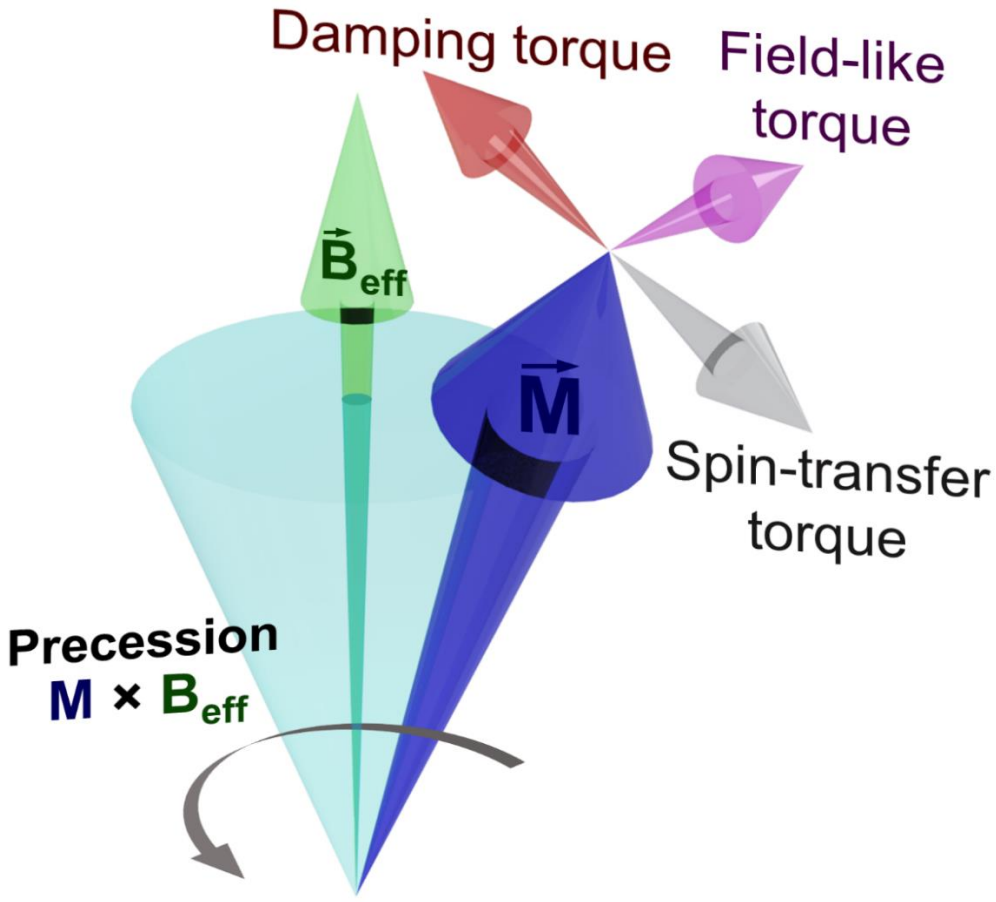

Figure 0.5: Precessional cone (cyan) of ferromagnetic resonance depicting the local effective magnetic field (green) and its effect on the dynamics of the magnetization (blue). Relevant torques on the magnetization are also shown including damping, STT (anti-damping), and the field-like torque.

STT can be incorporated into the LLG equation in the following way,

$$\dot{\vec{M}} = \gamma \vec{M} \times \vec{B}_{eff} - \frac{\alpha}{M} \vec{M} \times \dot{\vec{M}} + \eta \frac{I}{eMM'} \vec{M} \times \left(\overrightarrow{M'} \times \vec{M} \right) \qquad (0.3)$$

where η is a parameter describing the strength of STT, e is the electron charge, M' is the magnetization polarization direction of the incoming electrons.[12]

Ferromagnetic resonance is not only important as a measurement technique for gaining physical insight on magnetic systems, but also because the magnetization switching process in MTJs follows a precessionary evolution as shown in Figure 0.6.

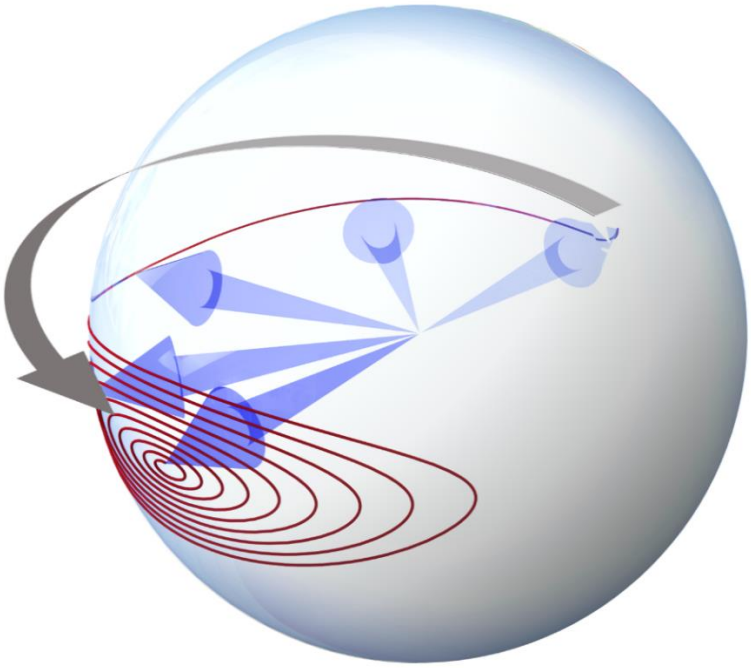

Figure 0.6: Depiction of the precessionary evolution of the MTJ free layer magnetization switching (blue) when supplied with a substantial half-phase STT. Damping spiral can be seen as the magnetization evolves to a direction 180° from its initial state.

Voltage Controlled Magnetic Anisotropy

The success of STT-based MRAM hoisted the device mode to within reach of competing with SRAM, DRAM, and FLASH memory modes. However, one aspect i.e. energy efficiency, especially in writing which requires large current densities, was lacking in STT-MRAM. During the 2000s, spintronic developers took a page from the book of transistor developers in the middle of the 20th century: moving on from current controlled bipolar junction transistors to voltage controlled MOSFETs. Multiferroic systems, which possess coupling between magnetism and electric fields became promising for lowering dissipated energy, despite limiting the number of materials able to be incorporated. At the same time a simpler method of integrating higher voltage and lower currents into MRAM systems developed: voltage controlled magnetic anisotropy (VCMA).[13–16]

Increasing the thickness of the tunneling barrier inherently raises resistance which in turn increases (decreases) the voltage (current). Simply increasing resistance across an MTJ would not be expected to have a beneficial effect, indeed the STT would decrease along with current. However, measurements revealed a voltage-based modulation of the local magnetic anisotropy at higher voltages. This VCMA has the effect of lowering (or raising) the energy barrier between the two resistance states, enabling a decrease in the required STT current. An alternative way to probe VCMA discussed in this work is to increase the size of the MTJ, thereby decreasing the current density and increasing the relative visibility of the VCMA effect.

Multiple mechanisms have been proposed for the origin of VCMA, none commanding consensus.[17] The mechanism with the most support implicates an electric field induced redistribution of charge in a select few of the magnetic material d orbitals (typically CoFeB) at the metal-insulator interface as shown in Figure 0.7.

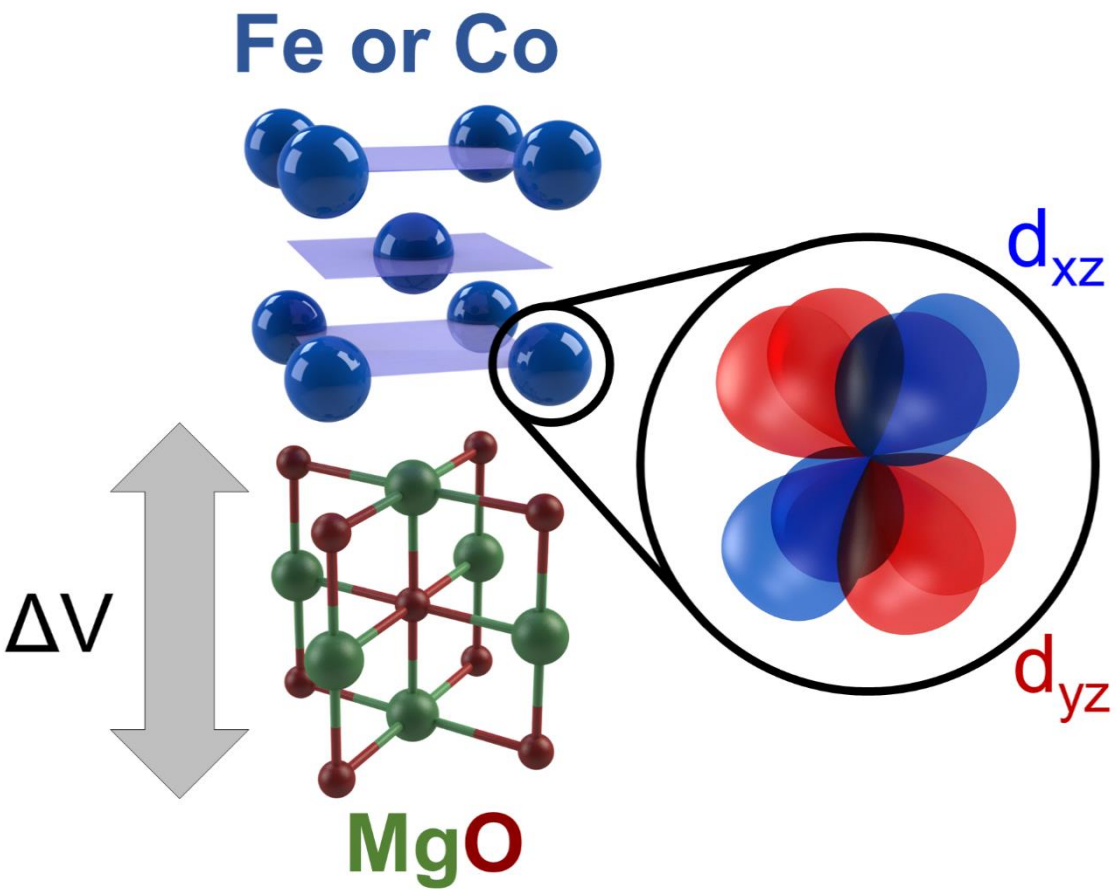

Figure 0.7: Voltage controlled magnetic anisotropy (VCMA) is thought to be caused by an applied electric field induced redistribution of charge at the metal-insulator interface mainly within the d_{xz} and d_{yz} orbitals of the magnetic material.

In the practical application of VCMA to MRAM (sometimes denoted MeRAM for Magnetoelectric RAM) two regimes have developed which seek to capitalize on separate emphases: speed and energy efficiency. As shown in Figure 0.8, the regimes can be separated simply by defining a critical voltage which forces the energy barrier between the two resistance states to zero. With sophisticated timing control a voltage pulse greater than the critical voltage lasting one half of the precessional period and consisting of both VCMA and STT effects can switch an MTJ free layer with speeds (<1 ns, <1 fJ) competing with

SRAM (1 ns, 10 fJ). On the other hand, a less intense pulse can significantly lower the energy barrier while providing a STT that along with thermal fluctuations switches the MTJ free layer in a matter of precessional cycles. Thermally assisted switching requires less energy than precessional switching and competes with DRAM write speeds (100 µs, 1 pJ). Also, due to its nonvolatile nature, MRAM has the possibility of competing with FLASH (100 µs, 1 nJ). [18–20]

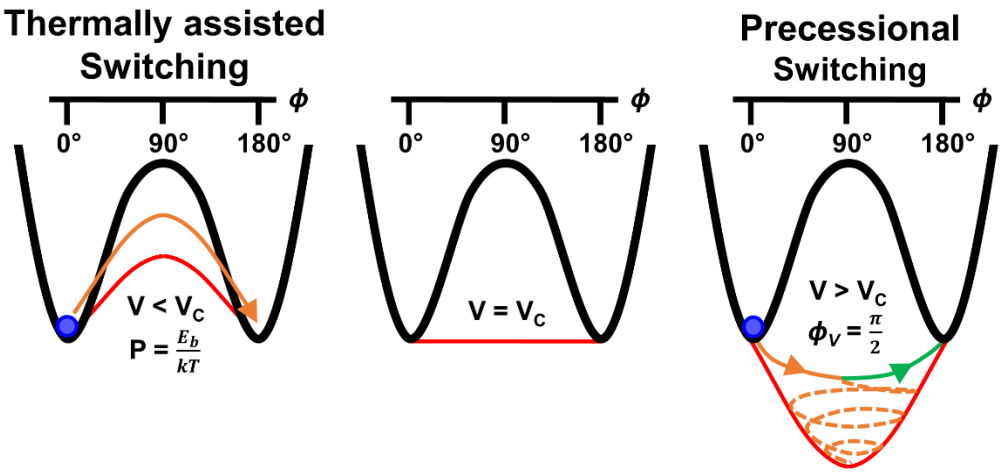

Figure 0.8: Thermally assisted and precessional switching regimes in VCMA assisted STT MRAM devices. Blue circle represents magnetization direction, which is resting in an energy well adjacent to the switching energy barrier in black. In the middle, a critical voltage is defined such that the height of the energy barrier is zero (red). On the left, a voltage lower that V_C is applied inducing thermally assisted switching with probability P. On the right, a supercritical voltage is applied causing the magnetization to precess about a new energy minimum. A half period (ϕ_v) voltage pulse (orange) causes the magnetization to precessionally switch. The dashed orange line represents the path of precession for a constant supercritical voltage.

Work continued in the 2010s to find material combinations that increased the modulation strength of VCMA, enabling the application of similar voltages for augmented

local virtual fields. VCMA continues to be a topic of interest to many and influences the design of commercial MRAM.

As mentioned previously, two MTJ geometries, in-plane and perpendicular, have dominated fabricated devices. Each geometry is produced by varying the amount of relative authority that local shape anisotropy possesses. Due to the thin film nature of MTJ devices shape anisotropy plays a substantial role in pinning the magnetization vector in the film plane. MTJ devices exhibiting such geometries are in-plane magnetized MTJs (iMTJs). However, if the film is extremely thin (about < 2nm) interfacial anisotropy can overtake shape anisotropy causing the magnetization to be orthogonal to the film plane, indicating perpendicular magnetized MTJs (pMTJs).

Figure 0.9 shows the quantitative effects of including shape and VCMA into the ferromagnetic resonance condition in both pMTJs and iMTJs. In isotropic media with no anisotropies, the LLG equation results in a relatively simple linear resonance condition with the form of Kittel's equation shown in the green box,

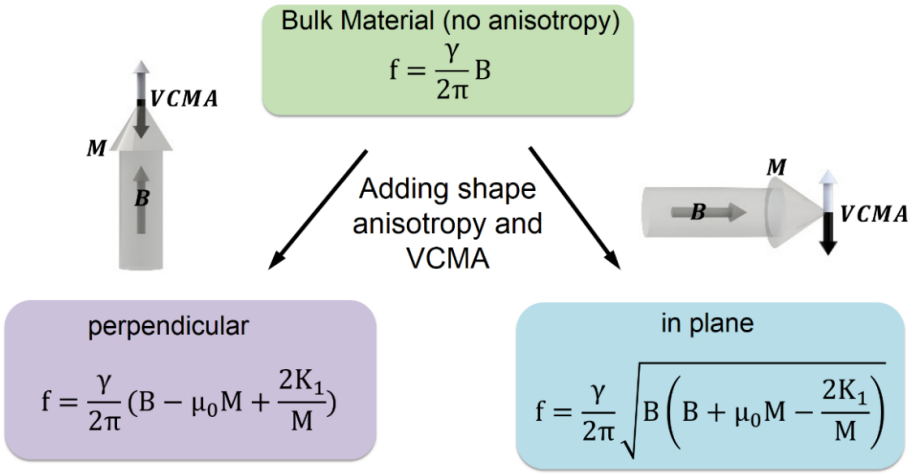

Figure 0.9: VCMA influence on FMR is shown to be markedly different for perpendicular magnetization geometries compared to in-plane magnetization geometries.

where μ_0 is the permeability of free space and K_1 is the VCMA energy density. In the case of pMTJs (purple box), the applied B field, the shape anisotropy virtual field, the VCMA virtual field all line up in the same direction. This alignment results in a retention of the linear frequency-field relationship as in isotropic media. For iMTJs (blue box) the story is slightly more complex. Due to the in-plane shape anisotropy, Kittel's equation takes on a square root form where the resonance frequency becomes proportional to a geometric average of two field terms. The first is the applied magnetic field; the second is the sum of the applied magnetic field, the shape anisotropy virtual field, and the VCMA virtual field. The arrows depicting applied field, magnetization and VCMA field suggest that the effect of VCMA will have different signatures for pMTJs and iMTJs. We shall investigate these signatures in Chapters 3 and 4 of this work.

0.3 Antiferromagnetic Spintronics

Antiferromagnetic (AFM) materials have long been used as passive components for spintronic devices, most notably in conjunction with constraining the fixed layer of MTJs. However, purely antiferromagnetic spintronic devices have the capability of ensuring significant benefits over ferromagnetic devices including THz switching speeds, enhanced scalability, and robustness against perturbing magnetic fields.

The magnetic ordering of a material is an intrinsic property that can generally be categorized in one of the following conditions: paramagnetic, diamagnetic, ferromagnetic, ferrimagnetic, and antiferromagnetic. For the purposes in this work we will focus on ferromagnetic and antiferromagnetic ordering.

As shown in Figure 0.10, the magnetic moments of the electrons in a ferromagnetic material are aligned. The local coupling that causes the moments to align forms domains the size of which is determined by the minimization of surface area and volumetric energies competing to establish balance. Antiferromagnetic materials host magnetic moments ordered in such a way as to cancel the net magnetic moment within a unit cell. The simplest antiferromagnetic ordering (collinear) is shown in Figure 0.10, but more complex configurations requiring more than two moments to cancel the net moment are commonplace.

The origin of the benefits of antiferromagnetic materials for spintronic applications is fundamentally tied to the magnetic order. High precessional speeds (and therefore switching speeds) are caused by exchange fields that can exceed 1 tesla due to neighboring moments. As shown previously in Kittel's equation, precessional frequency increases as B_{eff} increases.[21] Also, due to AFM material's zero net magnetic moment, devices may be placed extremely close to one another while avoiding interfering cross-talk. And lastly,

AFM materials are resistant to external magnetic fields due to the strength and compensating nature of the exchange fields.

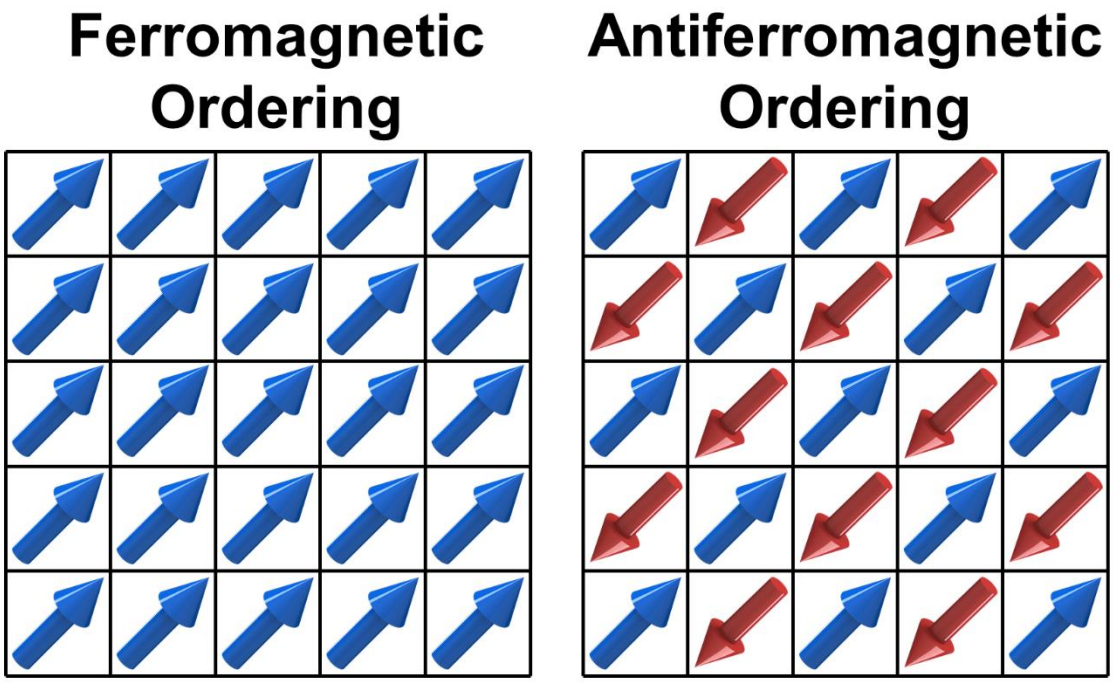

Figure 0.10: Magnetic ordering of ferromagnetic and antiferromagnetic (AFM) materials. Simplest case of AFM order composed of anti-aligned moments on lattice sites.

However, the very qualities that provide the isolatory benefits of AFM materials lead to difficulties in intentional manipulation of their magnetic states for spintronic applications. Work has focused on using the spin-orbit coupling (SOC) in materials as a complex lever for exerting control over AFM order especially in transition metal oxides (TMOs) which exhibit strong SOC. Spin-orbit coupling refers to the atomic interaction between an electron's spin and its orbital angular momentum. Furthermore, as discussed with ferromagnetic spintronics, electric field, as opposed to current controlled devices offer

more assuring opportunities for high energy efficiency implementions.[22] As a result, AFM insulators fulfill spintronic application criteria more favorably than AFM metals. A class of TMOs called iridates has proven to be a rich source of fundamental understanding for such effects and has nascent potential for AFM spintronics.

Two AFM species of Ruddlesden-Popper series iridates ($Sr_{n+1}Ir_nO_{3n+1}$) which have been the subjects of focus in our lab, namely Sr_2IrO_4 and $Sr_3Ir_2O_7$,[23] have potential for spintronic applications due to the comparable energy scales of spin-orbit coupling, crystal field splitting, and electron correlations. As in many transition metal compounds crystal field splitting is responsible for the formation of the e_g and t_{2g} bands. The combined effects of strong spin-orbit coupling and Coulomb repulsion of the distended atomic orbitals result in a splitting of the localized states from the $5d^5$ (t_{2g}) band forming a J_{eff} = ½ Mott-type insulating gap as shown in Figure 0.11.

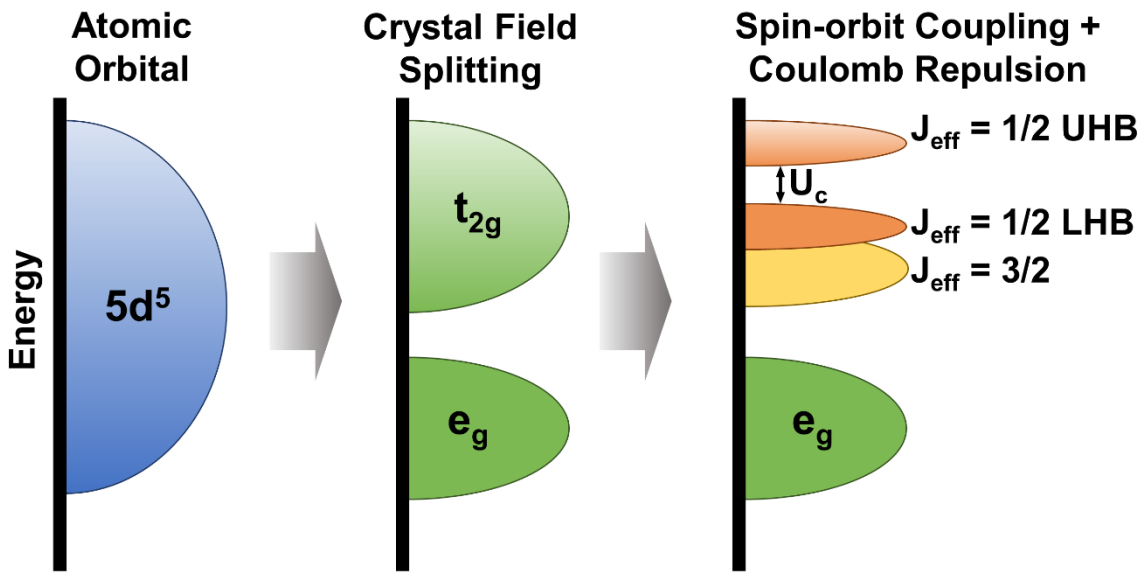

Figure 0.11: Atomic orbital splitting due to multiple effects including crystal field splitting, spin-orbit coupling, and Coulomb repulsion. U_c is the Coulomb potential gap separating the upper and lower Hubbard bands, UHB and LHB, respectively.

In this way Sr_2IrO_4 ($Sr_3Ir_2O_7$) is a Mott insulator with a Néel temperature of 240 K (285 K).[24] Previous work in our group found an electrically tunable band gap in both iridates as well as anisotropic magnetoresistance in Sr_2IrO_4.[25, 26, 27] The electrically tunable transport found in $Sr_2IrO_4$was attributed to electric field induced lattice distortions causing electronic band structure modification in 2015 by Drs. Cheng Wang and Maxim Tsoi. The same mechanism was promoted upon observation of similar behavior in $Sr_3Ir_2O_7$. Subsequently, electric bias induced lattice distortion has garnered more support[28] and was confirmed by x-ray diffraction measurements.[29]

In this work, we focus on the transport characteristics of the second iridate $Sr_3Ir_2O_7$. Development of magnetically dynamic materials such as iridates and TMOs in general may

elicit the manifestation of devices analogous to AFM-MTJs incorporating the benefits of exclusively AFM spintronic devices as depicted in Figure 0.12.

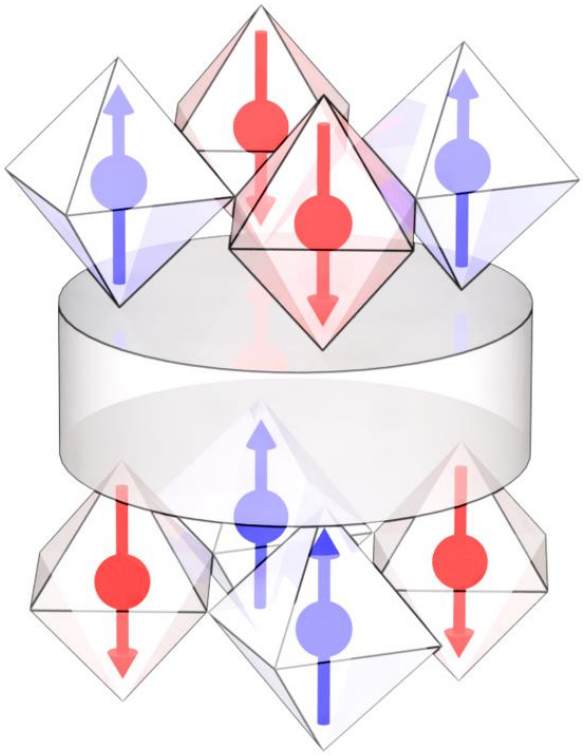

Figure 0.12: Further development of materials with strong spin-orbit coupling may realize devices with similar importance to MTJ with AFM materials.

0.4 References

[1] M. N. Baibich, J. M. Broto, A. Fert, F. Nguyen Van Dau, F. Petroff, P. Etienne, G. Creuzet, A. Friederich, and J. Chazelas, *Phys. Rev. Lett.* **61**, 2472 (1988).

[2] M. Flatte, *IEEE Transactions on Electron Devices* **54**, 5 (2007).

[3] V. Baltz, A. Manchon, M. Tsoi, T. Moriyama, T. Ono, and Y. Tserkovnyak, *Rev. Mod. Phys.* **90**, 015005 (2018).

[4] A. H. MacDonald and M. Tsoi, *Phil. Trans. R. Soc. A* **369**, 3098-3114 (2011).

[5] C. Chappert, A. Fert, F. N. Van Dau, *Nat. Mater.* **6**, 813–823 (2007).

[6] J. C. Slonczewski, *J. Magn. Magn. Mater.* **159**, (1996).

[7] M. Tsoi, A. G. M. Jansen, J. Bass, W.-C. Chiang, M. Seck, V. Tsoi, and P. Wyder, *Phys. Rev. Lett.* **80**, 42 (1998).

[8] M. Tsoi, A. G. M. Jansen, J. Bass, W.-C. Chiang, M. Seck, V. Tsoi, and P. Wyder, *Nature* **406** (1998).

[9] H. Seinige, *Current-driven Non-linear Magnetodynamics in Magnetic Nano-devices.* Austin: U of Texas, 2016.

[10] M. Williamson, *Ferromagnetic Resonance in Magnetic Tunnel Junctions under High DC Biases*. Austin: U of Texas, 2016

[11] C. Kittel, Phys. Rev. **73**, 2 (1948).

[12] A. A. Tulapurkar, Y. Suzuki, A. Fukushima, H. Kubota, H. Maehara, K. Tsunekawa, D. D. Djayaprawira, N. Watanabe, and S. Yuasa, *Nature* **438,** 339–342 (2005).

[13] F. Matsukura, Y. Tokura, and H. Ohno, Nature Nanotechnology 10 (2015).

[14] T. Nozaki, Y. Shiota, S. Miwa, S. Murakami, F. Bonell, S. Ishibashi, H. Kubota, K. Yakushiji, T. Saruya, A. Fukushima, S. Yuasa, T. Shinjo and Y. Suzuki, Nature Physics 8 (2012).

[15] T. Maruyama, Y. Shiota, T. Nozaki, K. Ohta, N. Toda, M. Mizuguchi, A. A. Tulapurkar, T. Shinjo, M. Shiraishi, S. Mizukami, Y. Ando, and Y. Suzuki, *Nature Nanotechnology* **4** (2009).

[16] W. G. Wang, C. L. Chien, *J. Phys. D: Appl. Phys.* **46** (2013).

[17] D. Odkhuu, W. S. Yun, S. H. Rhim, S. C. Hong, *J. Magn. Magn. Mater.* **414,** 126 (2016).

[18] H. Lee, A. Lee, S. Wang, F. Ebrahimi, P. Gupta, P. Khalili Amiri, K. L. Wang, *IEEE Transactions on Magnetics* **54**, 4 (2018).

[19] P. Khalili Amiri, J. G. Alzate, X. Q. Cai, F. Ebrahimi, Q. Hu, K. Wong, C. Grèzes, H. Lee, G. Yu, X. Li, M. Akyol, Q. Shao, J. A. Katine, J. Langer, B. Ocker, and K. L. Wang, *IEEE Transactions on Magnetics* **51**, 11 (2015).

[20] K. L. Wang, H. Lee, P. Khalili Amiri, *IEEE Transactions on Nanotechnology* **14**, 6 (2015).

[21] C. Kittel, *Phys. Rev* **82**, 565 (1951).

[22] P. Wadley, B. Howells, J Železný, C. Andrews, V. Hills, R. P. Campion, V. Novák, K. Olejník, F. Maccherozzi, S. S. Dhesi, S. Y. Martin, T. Wagner, J. Wunderlich, F. Freimuth, Y. Mokrousov, J. Kuneš, J. S. Chauhan1, M. J. Grzybowski, A. W.

Rushforth, K. W. Edmonds, B. L. Gallagher, T. Jungwirth, *Science* **351**, 6273 (2016).
[23] G. Cao *at al.*, *Phys. Rev. B* **66**, 214412 (2002).
[24] N. F. Mott, *Adv. Phys.* **13**, 325 (1964).
[25] C. Wang, H. Seinige, G. Cao, J.-S. Zhou, J. B. Goodenough, and M. Tsoi, *Phys. Rev. B* **92**, 115136 (2015).
[26] H. Seinige, M. Williamson, S. Shen, C. Wang, G. Cao, J.-S. Zhou, J. B. Goodenough, and M. Tsoi, *Phys. Rev. B* **94**, 214434 (2016).
[27] C. Wang, H. Seinige, G. Cao, J.-S. Zhou, J. B. Goodenough, and M. Tsoi, *Phys. Rev. X* **4**, 041034 (2014).
[28] B. Kim, P. Liu, and C. Franchini, *Phys. Rev. B* **95**, 024406 (2017).
[29] G. Cao, J. Terzic, H.D. Zhao, H. Zheng, L. E. De Long, and P. S. Riseborough, *Phys. Rev. Lett.* **120**, 017201 (2018).

C H A P T E R I

VCMA IN PERPENDICULAR MAGNETIC TUNNEL JUNCTIONS

1.1 pMTJs

Control and manipulation of magnetic moments is one of the central themes of research in spintronics which uses the moments in various practical devices, e.g. to retain data in magnetic memory applications. For instance, the spin-transfer torque (STT) phenomenon[1–3] offers unprecedented spatial and temporal control in random access memory (STT-RAM) devices based on magnetic tunnel junctions (MTJs).

Furthermore, a particular device geometry, that of perpendicularly magnetized MTJs (pMTJs) has come to dominate production STT-RAM devices due to its increased thermal stability, azimuthally symmetric magnetization deviations, and denser packing.

The pMTJ geometry is defined by the magnetizations of both the free and fixed layers being perpendicular to the film plane. This geometry is achieved by depositing circular patterns of extremely thin magnetic layers (< 2 nm), activating interfacial anisotropy that effectively constrains the magnetizations to the two perpendicular states (up or down). Interfacial anisotropy is a local effect maximized in the proximity of the magnetic/insulating layer interface caused by the reordering of charge at the material discontinuity. By differentiating the free and fixed layers by their respective thicknesses, we are able to tune the relative strength of the competing forces of shape anisotropy (promoting in-plane magnetization) and interfacial anisotropy (promoting perpendicular magnetization). In such a way, the thinner layer becomes the pinned layer.

Unlike interfacial anisotropy, which is constant after device growth, voltage controlled magnetic anisotropy (VCMA) is adjustable. Today, VCMA[4–9] attracts considerable attention as a novel method to control and manipulate magnetizations in low power and fast switching MTJs.

Ferromagnetic resonance (FMR) is a standard spectroscopic technique which is used to probe anisotropies in magnetic materials. Here we use FMR to probe magnetodynamics in CoFeB/MgO/CoFeB MTJ pillars which allows us to quantify the effect of magnetic anisotropies in the MTJs and, in particular, VCMA. Specifically, we evaluated MTJs with perpendicular magnetizations and large (20 μm) diameters.

1.2 Experimental Setup

The pMTJs were grown at the University of Arizona[10] with the following composition: Ta (6nm)/Ru (10 nm)/Ta (6 nm)/CoFeB (0.7 nm/MgO (1.9 nm)/CoFeB (1.6 nm)/Ta (10 nm)/Ru (20 nm) and were patterned using optical photolithography into pillars

with 20 μm diameter. Connections from the source and measurement instruments to the device were made by wire bonding to patterned contact pads. The MTJ pillars have a resistance-area product of 3.8 $M\Omega \cdot \mu m^2$ and demonstrate tunneling magnetoresistance (TMR) ratios of about 100% at room temperature.

In our experiments, we apply a magnetic field (up to 270 mT) perpendicular to the MTJ layers and both rf and dc currents using a bias tee (see experimental schematic in Figure 1.1(a). The maximum dc bias of ±2.1 V (8 mA) results in an electric field developing across the tunneling barrier of ±1.1 V/nm. Amplitude modulated microwaves (20% modulation depth; frequency range from 9-14 GHz) are supplied to the sample from an rf generator. The high frequency microwaves are constrained to an oscillating envelope determined by the low frequency amplitude modulation (< 1 kHz). The amplitude modulation is required as a reference signal for the lock-in amplifier, which serves as a voltmeter tuned precisely to the low frequency amplitude modulation. In this way the lock-in amplifier is able to reject vast amounts of noise resulting in a high signal to noise ratio useful for detecting FMR. The actual amplitude of rf current across MTJs can be determined by comparing the increase in the MTJ's resistance produced by Joule heating from the dc and microwave currents. We estimate the rf currents across our large samples to be about 0–4 mA when power output is set to -20–(17) dBm at the generator.

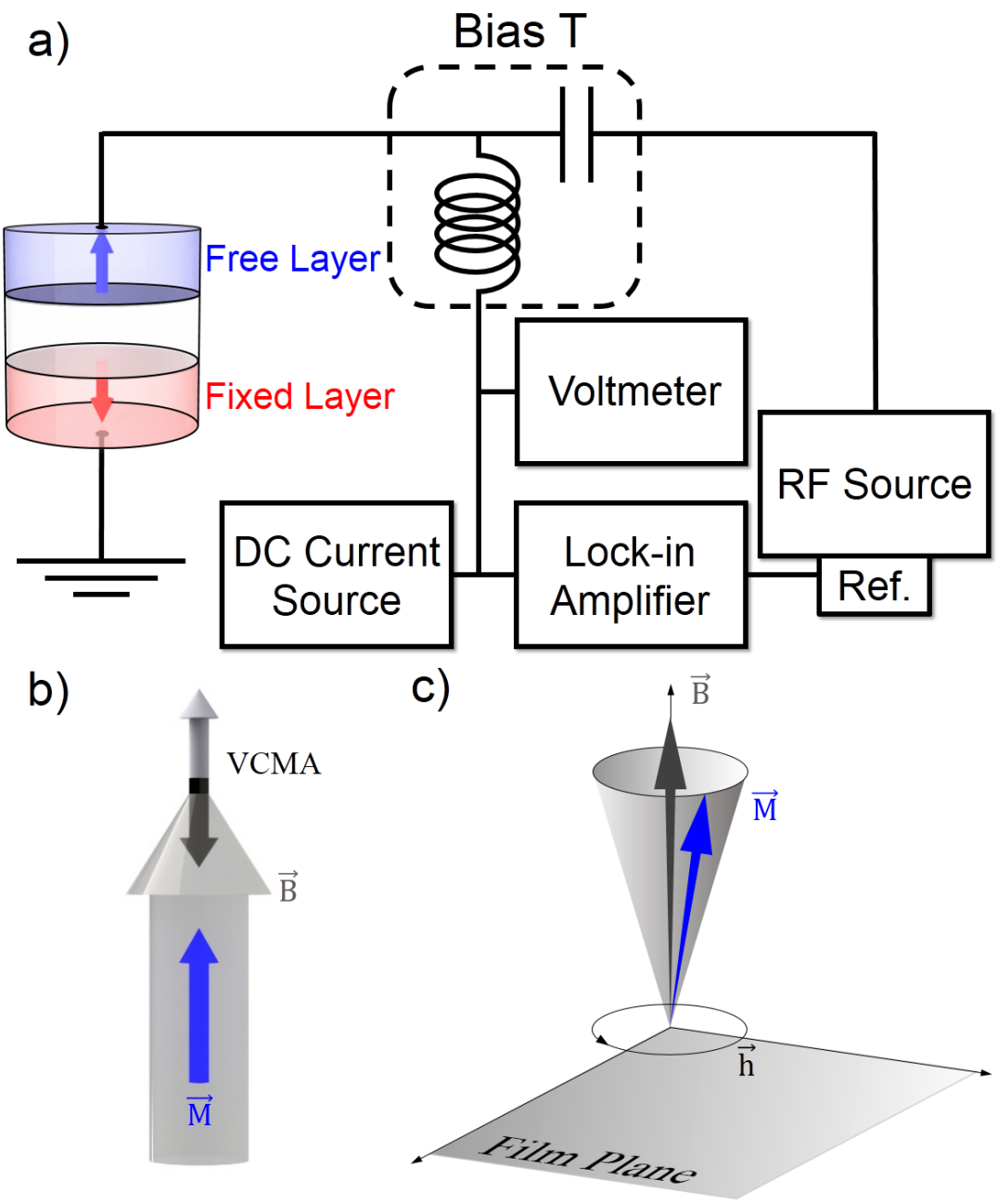

Figure 1.1: (a) Schematic of the experimental setup. (b) The relative orientation of the free-layer magnetization M, applied magnetic field B, and VCMA field. (c) FMR dynamics: the precessional M cone is shown relative to the film plane (xy-plane).

When a combined rf and dc bias is applied to the device, the resulting dc voltage across the contact includes V_{dc} produced by the dc bias and a small rectified V_ω produced by the microwaves. The latter provides a means to probe bias-driven magnetodynamics[7–9, 14–17] as $|V_\omega|$ peaks at resonance. We detect dc and rectified (resonance) voltage across MTJs using techniques already described.[3, 16, 17] At room temperature we have measured the rectified voltage V_ω as a function of an external magnetic field B applied perpendicular to the film plane. Such $V_\omega(B)$ spectra were measured at different frequencies and power levels of the applied microwaves and different dc bias currents. The electrical bias is expected to produce an effective VCMA field which acts along the gradient of the potential, i.e. parallel or antiparallel to the applied B (see Figure 1.1(b)). Both shape anisotropy and VCMA can be quantified by their influence on the resonance behavior of the precessing magnetization (see Figure 1.1(c)).

1.3 Results

Figure 1.2(a) shows a representative $V_\omega(B)$ FMR spectrum. FMR (peak in V_ω) of the free layer is clearly visible at ±90 mT. The large (off-scale) signal around 20 mT is due to the MTJ being in the antiparallel state. Note that the current density applied to the MTJ is too low to support the excitation of STT-FMR; we thus suggest VCMA as the dominant contributor to the FMR excitation[8,9] in our experiments.

The frequency-field relationship for FMR of the MTJ's free layer can be modeled by Kittel's equation. For a perpendicularly magnetized MTJ the equation takes the form:

$$f = \frac{\gamma}{2\pi}\left(B - M + \frac{2\mu_0 K_1}{M}\right) \qquad (1.1)$$

where γ is the gyromagnetic ratio, B is the applied field, M is the saturation magnetization and K_1 denotes the VCMA energy density modeled as (first order) uniaxial anisotropy.

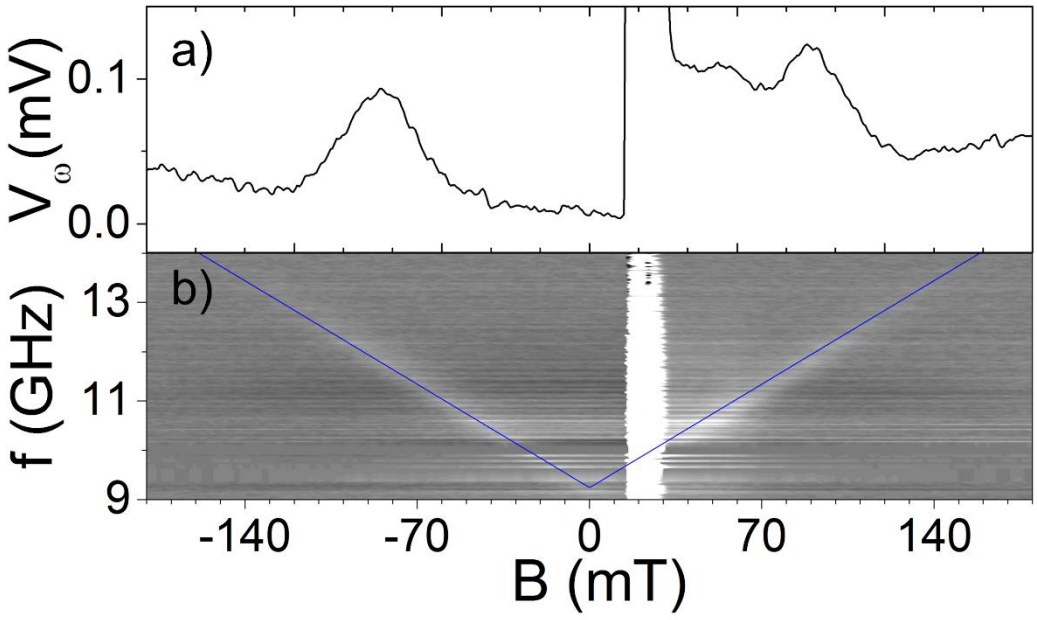

Figure 1.2: (a) FMR $V_\omega(B)$ spectrum for a MTJ with out-of-plane magnetization recorded at 0.2 mA (0.8 V) dc bias and 12.4 GHz rf current at 19 dBm. (b) The grey density plot shows FMR spectra at different frequencies (brighter color indicates larger V_ω). Solid blue curve is the Kittel's fit (Eq. 1.1).

Figure 1.2(b) shows an example of the frequency-field relationship observed in our pMTJ. The grey density plot shows the frequency dependence of the spectrum from Figure 1.2(a) (brighter color indicates larger V_ω). Using Eq. 1.1 we were able to successfully fit the observed frequency-field relationship (see blue curve in Figure 1.2(b)). When a dc bias is applied, we observe a shift of the resonance field as a function of the voltage (see Figure 1.3).

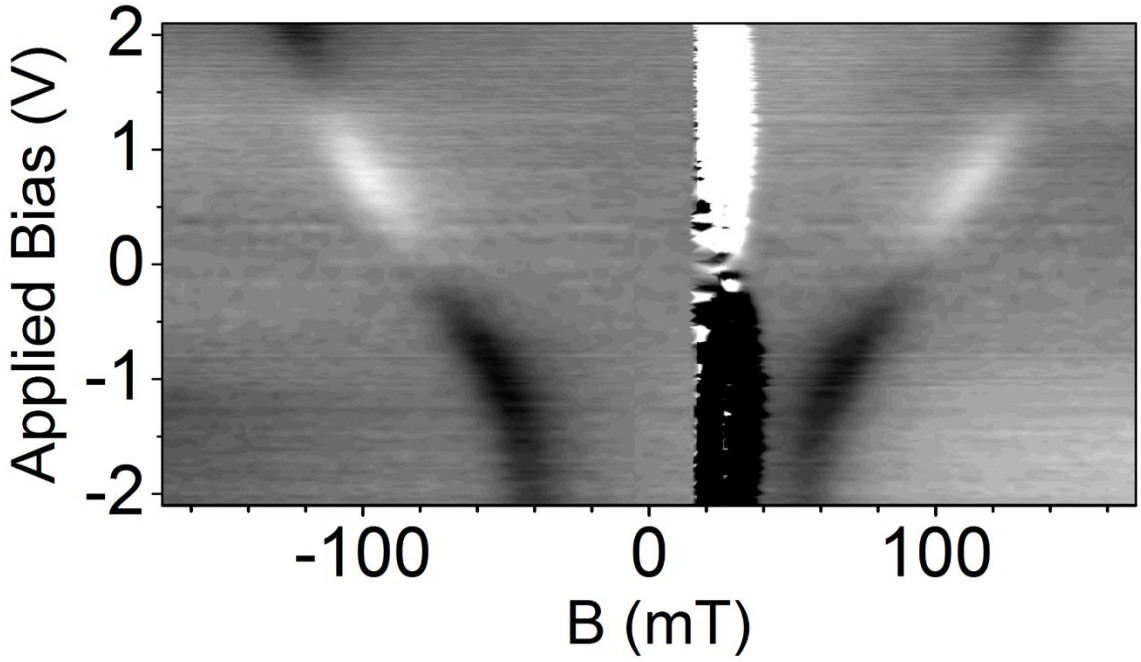

Figure 1.3: FMR spectra at 12.4 GHz with different biases applied (brighter color indicates larger V_ω). Slanted, slightly curved features indicate free layer resonance at both positive and negative magnetic fields. Off-scale feature around 20 mT (40 mT) due to device switching to (from) antiparallel state.

For relatively small voltages (up to 1 V) the shift is linear with respect to the applied bias and can be attributed to the out-of-plane VCMA induced by the dc bias.[7–9, 11–13] By measuring FMR spectra at different dc biases we were able to quantify VCMA as we show next.

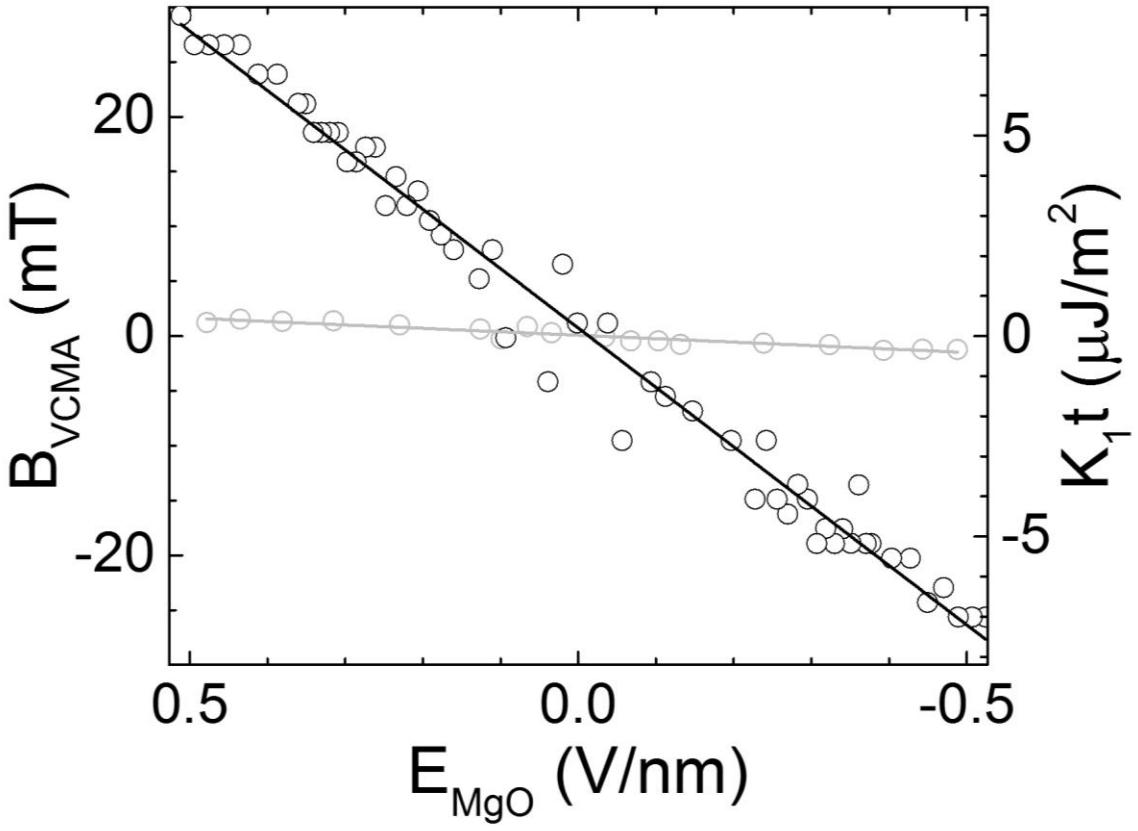

Figure 1.4: Shift of the resonance/coercive field (black/gray symbols; left scale) and the VCMA energy density per unit area (black symbols; right scale) plotted as a function of applied bias. Solid lines are corresponding linear fits.

Figure 1.4 shows the dependence of the resonance field and VCMA energy density per unit area on the applied voltage bias. Open circles show the experimental values extracted from the bias dependent $V_\omega(B)$ spectra (not shown) as in Figure 1.3. The increase in data scatter around zero bias is due to a small resonance signal at low biases; the rectified V_ω is proportional to the bias in the low voltage linear regime.[8, 9, 14–17] For our linear fit to the data in Figure 1.4 gives a slope of 15 mT-nm/V for the resonance field which agrees very well with the negative bias region in the work by Miura et al.[9] and corresponds to a

slope of 7.8 μJ-nm/V-m^2 for the magnetic anisotropy energy. The observed linear shift is consistent with the VCMA picture based on the bias-induced electron migration across the MgO/CoFeB interface.[11–13] However, other compelling mechanisms have been proposed.[18–22]

It is interesting to compare the above FMR-VCMA results with measurements of bias-dependent coercive field, which are sometimes used to quantify VCMA as in Figure 1.5. In coercive field measurements we sweep magnetic field (in this case, downsweep) and measure the coercivity indicated by the magnetoresistance switching to/from the high resistance state. By observing the coercive field at different biases we are able to describe the VCMA effective field variation with respect to applied bias. In Figure 1.5, interestingly, the voltage is observed to modulate the coercive field more (less) when switching from (to) the high resistance state.

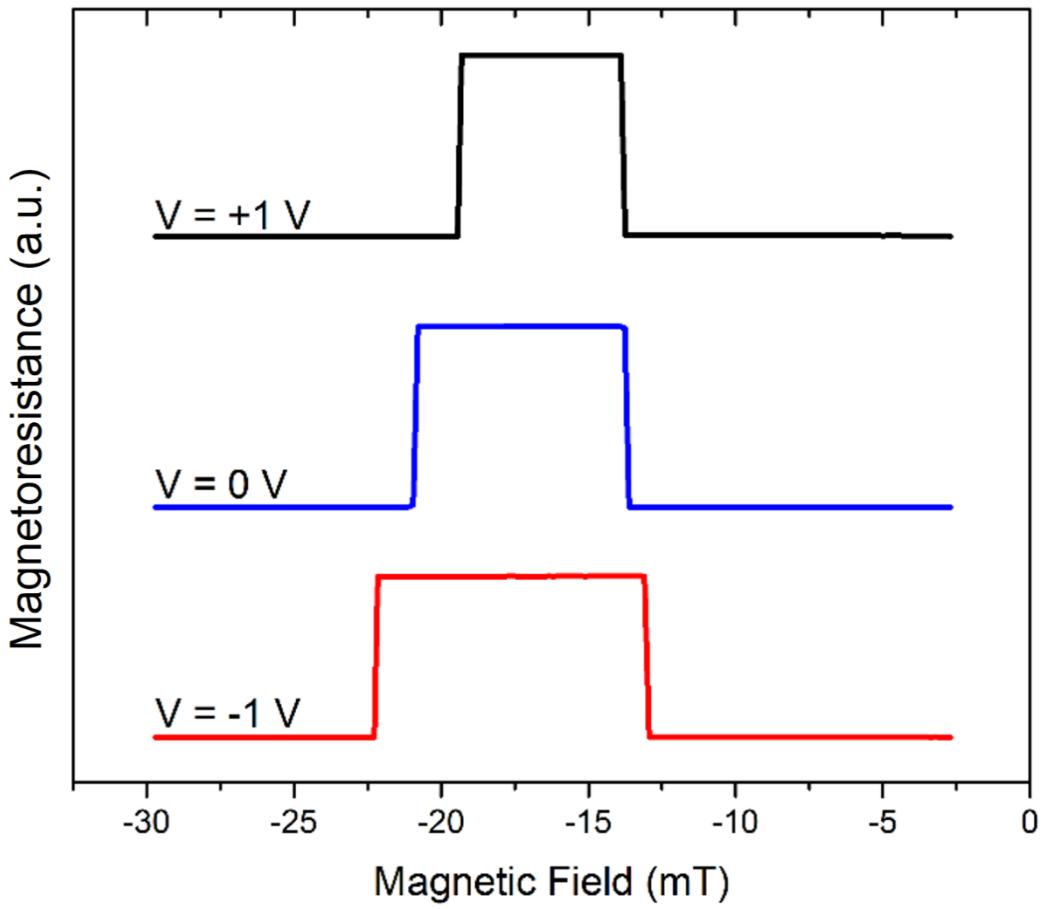

Figure 1.5: Shift of the coercive field for a pMTJ at different biases indicating the VCMA effect.

Furthermore, Figure 1.4 shows the coercive field of the free layer (gray symbols; left scale) measured as a function of the applied bias voltage in the same MTJ. The linear fit to the coercive-field data (gray line in Figure 1.4) gives a slope of 0.84 mT-nm/V which is about 18 times smaller than the FMR result. We tentatively attribute this difference to the difference between the precession of a saturated magnetic moment and the switching process in a macroscopic (20 µm) multidomain film. The switching process in such a large pillar is likely dominated by the nucleation of magnetic domains which in aggregate seem to be less influenced by the VCMA effective field.

Furthermore, if we increase the applied bias to a maximum of ±2.1 V we observe the first hints of saturation of the VCMA effect. In Figure 1.6, the data show that at positive maximum bias the shift of the coercive field remains linear. However, beyond a bias of -1 V the effectiveness of the applied bias to shift the coercive field weakens until around 1.3 V where a turning point occurs demonstrating that further increase in negative bias decreases the coercive field up to 2.1 V.

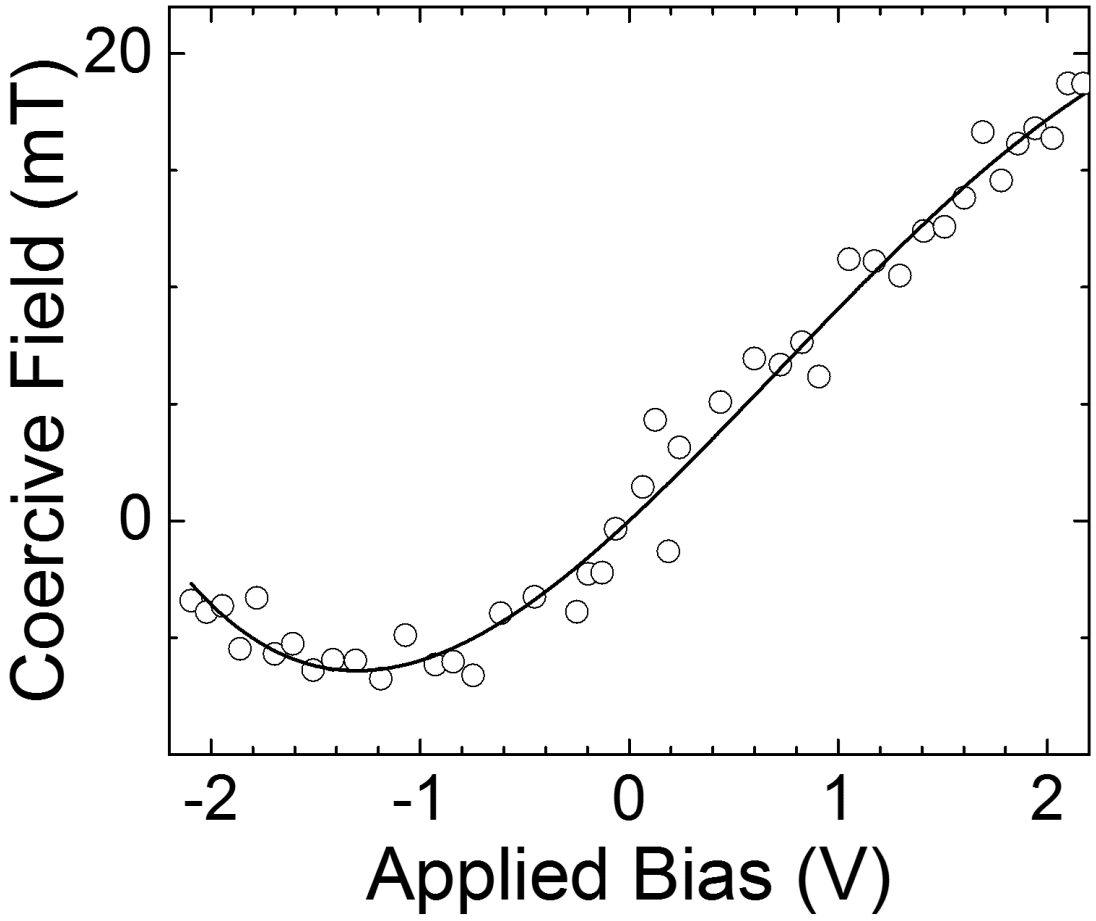

Figure 1.6: Coercive field extracted from magnetic field downsweeps in which the device switches from the high resistance state measured at maximum bias range. Solid curve is a guide for the eye suggesting coercive field shift saturation at high negative biases.

In addition to the coercive field measurements, we also measured the shift in the resonance field due to VCMA at the same high biases. Figure 1.7 shows the resonance field and VCMA energy density per unit area (like Figure 1.4) for voltages up to 2.1 V. These measurements were performed on a different MTJ (to show reproducibility of our data for different devices). At low biases (below ±1 V) we observed a linear dependence on the applied bias voltage with a slope of 14.2 mT-nm/V for the resonance field and corresponding 7.4 μJ-nm/V-m^2 slope for the magnetic anisotropy energy. These numbers are very similar to those in Figure 1.4 that corroborates the FMR-VCMA results for different MTJs.

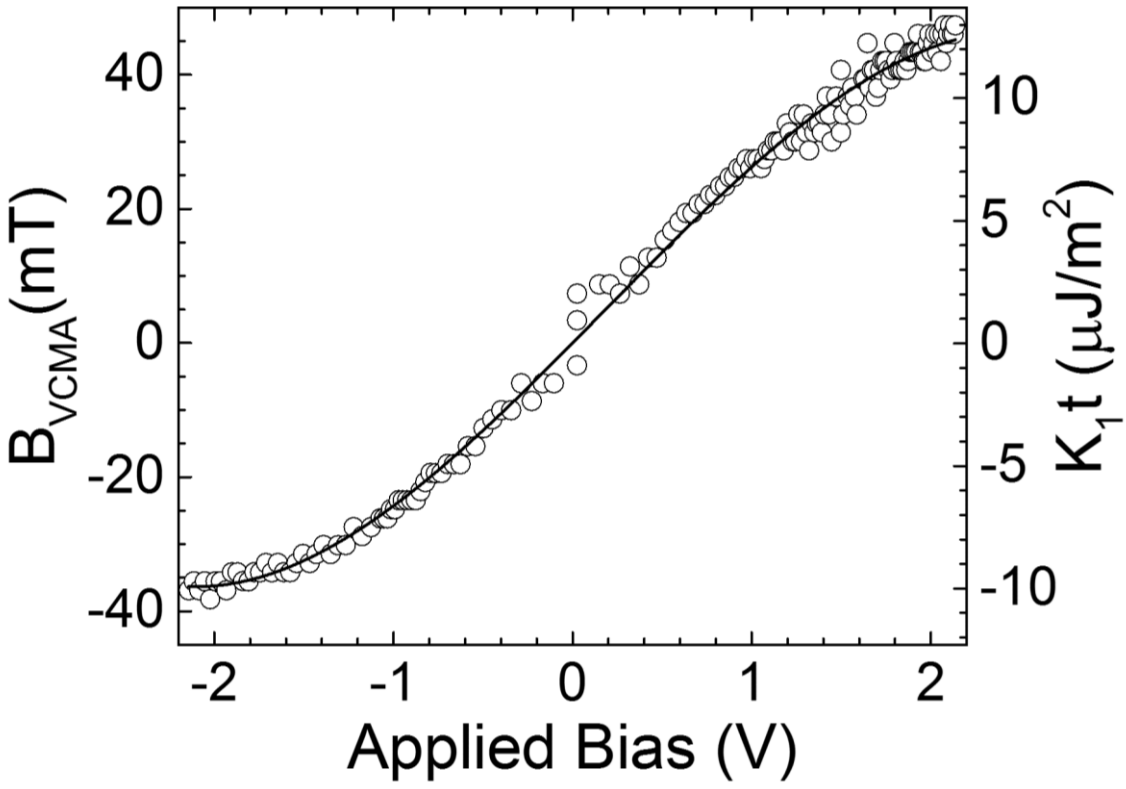

Figure 1.7: Shift of the resonant magnetic field for a pMTJ at 12.4 GHz (left scale) and the VCMA energy density per unit area (right scale) plotted as a function of applied bias. Solid curve is a guide for the eye.

A closer look at Figure 1.3 reveals that the amplitude of the resonance peak varies with respect to bias. The amplitude near zero bias takes on the expected positive/negative values corresponding to the positive/negative polarity of the applied bias. However, at biases higher than positive 1 V, conspicuously linked with VCMA saturation conditions, this trend is modified. As shown in Figure 1.8, at high negative biases the resonance amplitude unexpectedly exhibits positive polarity. In a similar manner, the resonance amplitude at high positive biases turns back toward zero, but remains at diminished positive value. Such bias dependent asymmetry could be the result of the slightly asymmetric geometries of the capping layers above and below the MTJ.

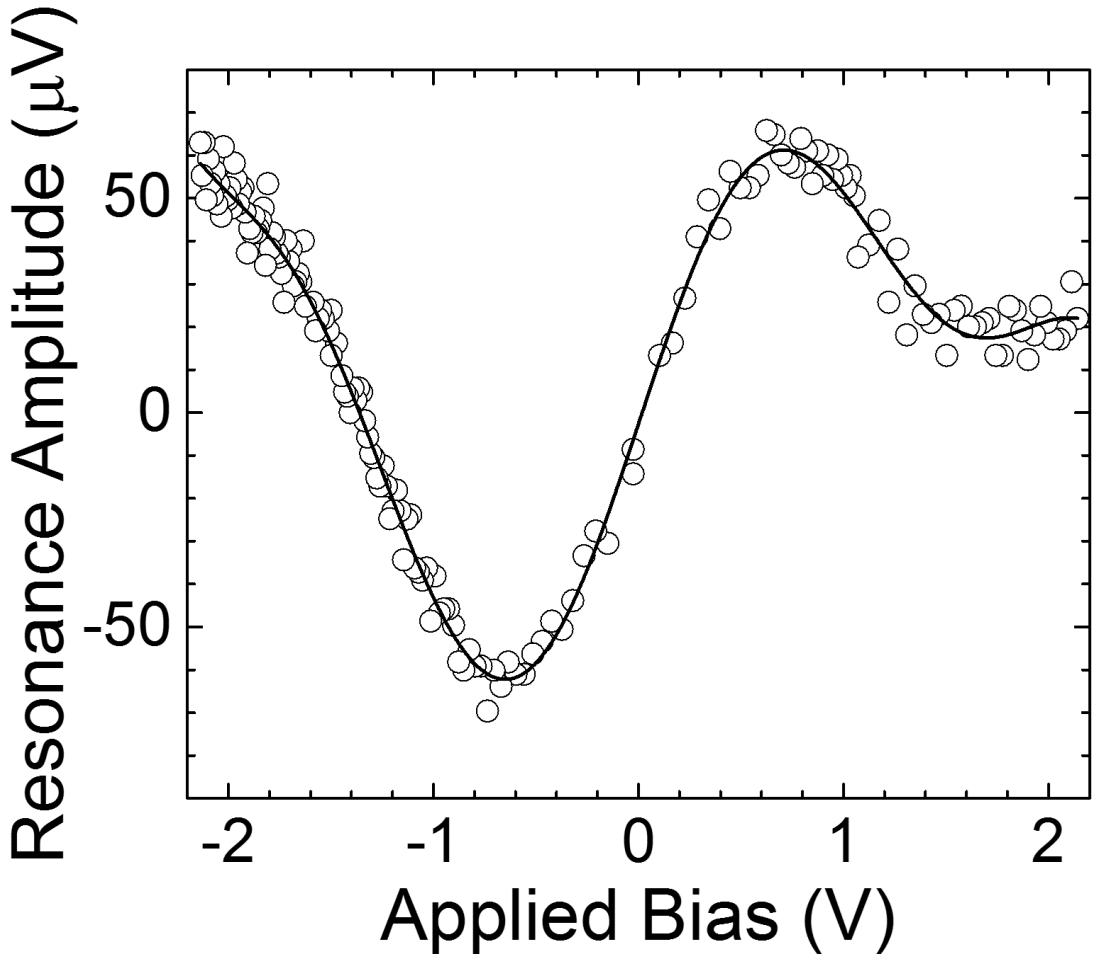

Figure 1.8: Resonance amplitude as a function of applied bias displaying linear behavior at biases near zero and nonlinear deviations at high biases. Solid curve is a guide for the eye.

1.4 Discussion

At biases beyond ±1 V we observe deviations from the linear behavior for both positive and negative bias polarities (see Figure 1.7). At the highest biases the resonance field seems to saturate. The latter may indicate a saturation of the VCMA effect which could be associated with a saturation of the electron migration[11–13] across the MgO/CoFeB interface at high biases. Some theoretical insight into this process can be found in the work

by Zhang et al.[23] who predicted a reduced VCMA at higher electrical biases. Further theoretical work is needed to provide a more quantitative picture of the saturation process in our FMR experiments.

1.5 Conclusions

In summary, we investigated voltage controlled magnetic anisotropy (VCMA) in perpendicularly magnetized CoFeB/MgO/CoFeB magnetic tunnel junctions (MTJs) using ferromagnetic resonance (FMR) technique. We observed a shift in the resonance field as a function of the bias voltage applied to MTJ which is linear for low biases (below ~1V). At higher biases we observed a deviation from the linear behavior which indicates a saturation of the VCMA effect. These results are important for the design of MTJ-based spintronic applications.

1.6 References

[1] J. C. Slonczewski, *J. Magn. Magn. Mater.* **159,** L1–L7 (1996).
[2] L. Berger, *Phys. Rev. B* **54,** 9353–9358 (1996).
[3] M. Tsoi, A. G. M. Jansen, J. Bass, W.-C. Chiang, M. Seck, V. Tsoi, and P. Wyder, *Phys. Rev. Lett.* **80,** 4281–4284 (1998).
[4] F. Matsukura, Y. Tokura, and H. Ohno, *Nat. Nanotechnol.* **10,** 209–220 (2015).
[5] W.-G. Wang, M. Li, S. Hageman, and C. L. Chien, *Nat. Mater.* **11,** 64–68 (2011).
[6] S. Kanai, M. Yamanouchi, S. Ikeda, Y. Nakatani, F. Matsukura, and H. Ohno, *Appl. Phys. Lett.* **101,** 122403 (2012).
[7] A. Okada, S. Kanai, M. Yamanouchi, S. Ikeda, F. Matsukura, and H. Ohno, *Appl. Phys. Lett.* **105,** 052415 (2014).
[8] J. Zhu, J. A. Katin, G. E. Rowlands, Y.-J. Chen, Z. Duan, J. G. Alzate, P. Upadhyaya, J. Langer, P. Khalili Amiri, K. L. Wang, and I. N. Krivorotov, *Phys. Rev. Lett.* **108,** 197203 (2012).
[9] K. Miura, S. Yabuuchi, M. Yamada, M. Ichimura, B. Rana, S. Ogawa, H. Takahashi, Y. Fukuma, and Y. Otani, *Sci. Rep.* **7**, 42511 (2017);
[10] H. Almasi, M. Xu, Y. Xu, T. Newhouse-Illige, and W. G. Wang, *Appl. Phys. Lett.* **109,** 032401 (2016)
[11] K. Nakamura, R. Shimabukuro, Y. Fujiwara, T. Akiyama, T. Ito, and A. J. Freeman, *Phys. Rev. Lett.* **102,** 187201 (2009).
[12] M. Tsujikawa, T. Oda, *Phys. Rev. Lett.* **102,** 247203 (2009).
[13] C.-G. Duan, J. P. Velev, R. F. Sabirianov, Z. Zhu, J. Chu. S. S. Jaswal, and E. Y. Tsymbal, *Phys. Rev. Lett.* **101,** 137201 (2008).
[14] A. A. Tulapurkar, Y. Suzuki, A. Fukushima, H. Kubota, H. Maehara, K. Tsunekawa, D. D. Djayaprawira, N. Watanabe, and S. Yuasa, *Nature* **438,** 339–342 (2005).
[15] J. C. Sankey, P. M Braganca, A. G. F. Garcia, I. N. Krivorotov, R. A. Buhrman, and D. C. Ralph, *Phys. Rev. Lett.* **96,** 227601 (2006).
[16] T. Staudacher and M. Tsoi, *J. Appl. Phys.* **109,** 07C912 (2011).
[17] H. Seinige, C. Wang, and M. Tsoi, *J. of Appl. Phys.* **117,** 17C507 (2015).
[18] L. Xu and S. Zhang, *J. Appl. Phys.* **111,** 07C501 (2012).
[19] S. E. Barnes, J. Ieda, and S. Maekawa, *Sci. Rep.* **4,** 4105 (2014).
[20] D. Odkhuu, W. S. Yun, S. H. Rhim, S. C. Hong, *J. Magn. Magn. Mater.* **414,** 126 (2016).
[21] U. Bauer, L. Yao, A. J. Tan, P. Agrawal, S. Emori, H. L Tuller, S. van Dijken, and G. S. D. Beach, *Nat. Mater.* **14,** 174–181 (2014).
[22] A. Rajanikanth, T. Hauet, F. Montaigne, S. Mangin, and S. Andrieu, *Appl. Phys. Lett.* **103,** 062402 (2013).
[23] J. Zhang, P. V. Lukashev, S. S. Jaswal, and E. Y. Tsymbal, *Phys. Rev. B* **96,** 014435 (2017).

C H A P T E R II

VCMA IN MAGNETIC TUNNEL JUNCTIONS WITH IN-PLANE MAGNETIZATION

2.1 iMTJs

In many systems, e.g. MTJs with out-of-plane magnetizations, VCMA can be probed experimentally using standard magnetoresistance measurements. By measuring the effective coercive field as a function of the applied voltage the VCMA field can be probed directly because it is parallel/antiparallel to the out-of-plane applied field and simply adds up to the MTJ's intrinsic coercivity at zero voltage bias.[7,8] This simple method, however, cannot be used in MTJs with in-plane magnetizations (iMTJs) because the in-plane switching is not controlled by a perpendicular (VCMA) field.[9] Instead, the perpendicular

anisotropy energy should be deduced from the integral of magnetic hysteresis loop[10,11] which quantifies the work done on the material by the applied field. In this chapter we show that the ferromagnetic resonance (FMR) technique can be used to provide direct information about VCMA in MTJs with in-plane magnetizations.

2.2 Experimental Setup

Our in-plane MTJs are made of CoFeB(2nm)/MgO(0.8nm)/CoFeB(2.4nm)/ Ru(0.85nm)/CoFe(2.5nm)/PtMn(15nm) multilayers deposited onto oxidized Si substrates by rf/dc magnetron sputtering at the University of Minnesota,[12] and then patterned (E-beam lithography) into pillars with elliptical cross-sections with sizes on the order of 100 nm and aspect ratios of about 2.5.[13] The top CoFeB layer serves as the free layer while the second CoFeB layer is the fixed layer. The CoFe layer, which is coupled to the antiferromagnetic material PtMn serves as the reference layer. The fixed and the reference layer with the Ru spacer between comprise the synthetic antiferromagnet. The resistance-area products for the MTJs were $4\,\Omega\cdot\mu m^2$.In total, we tested 25 MTJs. All samples demonstrate typical tunneling magnetoresistances (TMRs) of about 100% at room temperature.

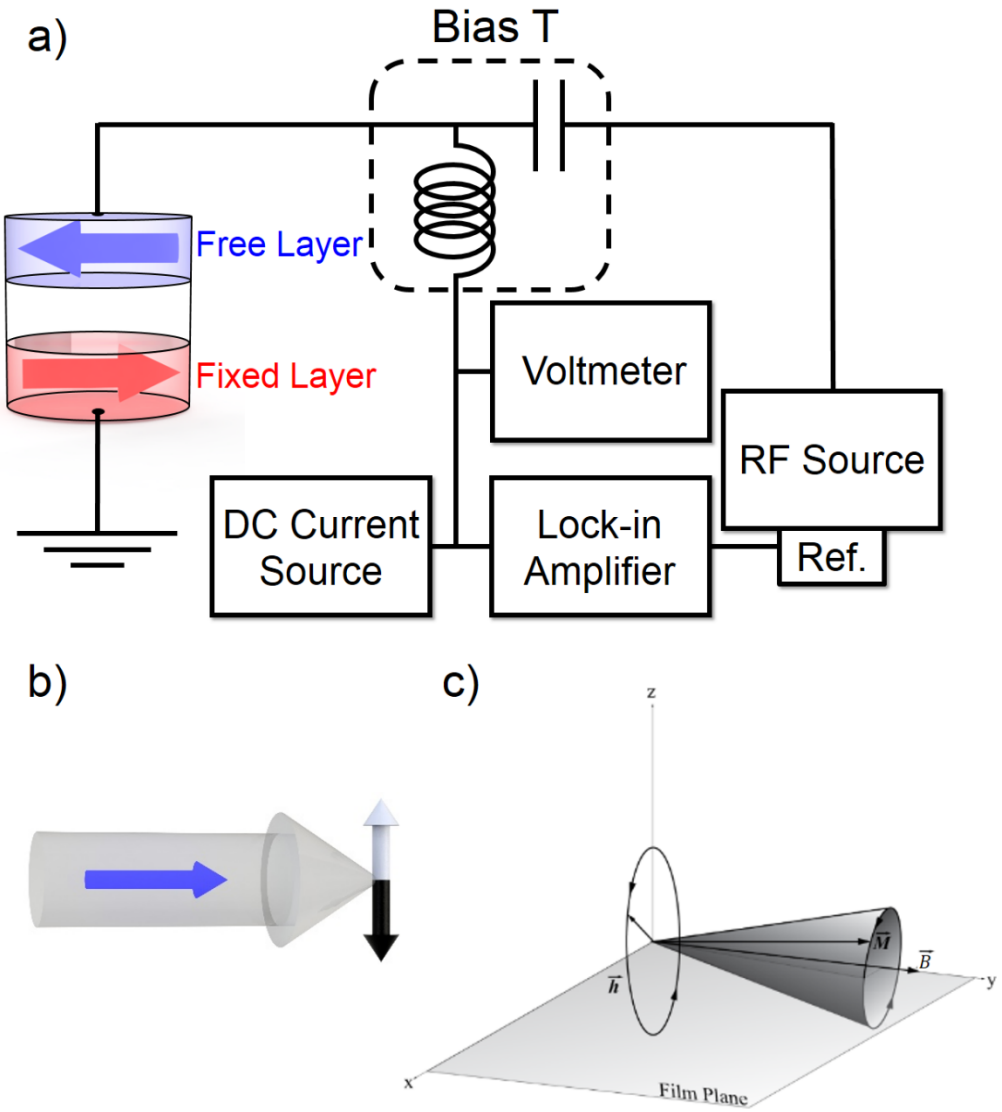

Figure 2.1: (a) Schematic of the experimental setup. (b) The relative orientation of the free-layer magnetization M, applied magnetic field B, and VCMA field. (c) FMR dynamics: the precessional M cone is shown relative to the film plane (xy-plane).

In our experiments, we apply both rf and dc currents to MTJs using a bias tee. The dc bias results in a maximum electric field developing across the tunneling barrier of MTJs of 0.6 V/nm. Amplitude modulated microwaves (20% modulation depth; frequency

range from 3-14 GHz) are supplied to the sample from an rf generator. As mentioned previously, the constant amplitude high frequency microwaves are constrained to an oscillating envelope determined by the low frequency amplitude modulation (< 1 kHz). The amplitude modulation is required as a reference signal for the lock-in amplifier, which serves as a voltmeter tuned precisely to the low frequency amplitude modulation. In this way the lock-in amplifier is able to reject vast amounts of noise resulting in a high signal to noise ratio useful for detecting FMR. The actual amplitude of rf current across MTJs can be determined by comparing the increase in the MTJ's resistance produced by Joule heating from the dc and microwave currents. We estimate the rf currents across our small samples to be about 0–4 mA when power output is set to -20–(17) dBm at the generator.

When a combined rf and dc bias is applied to the device, the resulting dc voltage across the contact includes V_{dc} produced by the dc bias and a small rectified V_{ω} produced by the microwaves. The latter provides a means to probe bias-driven magnetodynamics[3–5, 14–17] as $|V_{\omega}|$ peaks at resonance. We detect dc and rectified (resonance) voltage across the MTJs using techniques already described.[16, 17] At room temperature we have measured the rectified voltage V_{ω} as a function of an external magnetic field B applied in the plane of the in-plane MTJs. Such $V_{\omega}(B)$ spectra were measured at different frequencies and power levels of the applied microwaves and different dc bias currents.

Figure 2.1(a) shows a representative $V_{\omega}(B)$ spectrum measured at 10 GHz and small dc bias (3 mV) where VCMA is negligible. FMR (dip in V_{ω}) of the free layer is clearly visible at ±100 mT. Other dips/peaks are associated with FMR of the fixed layer and other resonance modes of the free layer as will be described later.

The frequency-field relationship for FMR of the MTJ's free layer can be modeled by Kittel's equation.

$$f = \frac{\gamma}{2\pi}\sqrt{B\left(B + M - \frac{2\mu_0 K_1}{M}\right)} \quad (2.1)$$

where M is the saturation magnetization and K_1 denotes the VCMA energy density modeled as (first order) uniaxial anisotropy.

2.3 Results

The grey density plot in Figure 2.2(b) shows the frequency dependence of the spectrum from Figure 2.2(a) (brighter color indicates larger V_ω). Using Eq. 2.1 we were able to successfully fit the first uniform free layer mode (see blue curve in Figure 2.2(b)). The free layer resonance modes (dark features) are concentrated at low fields (±150 mT) while the fixed layer resonances (light features) occur at higher fields (>100 mT).

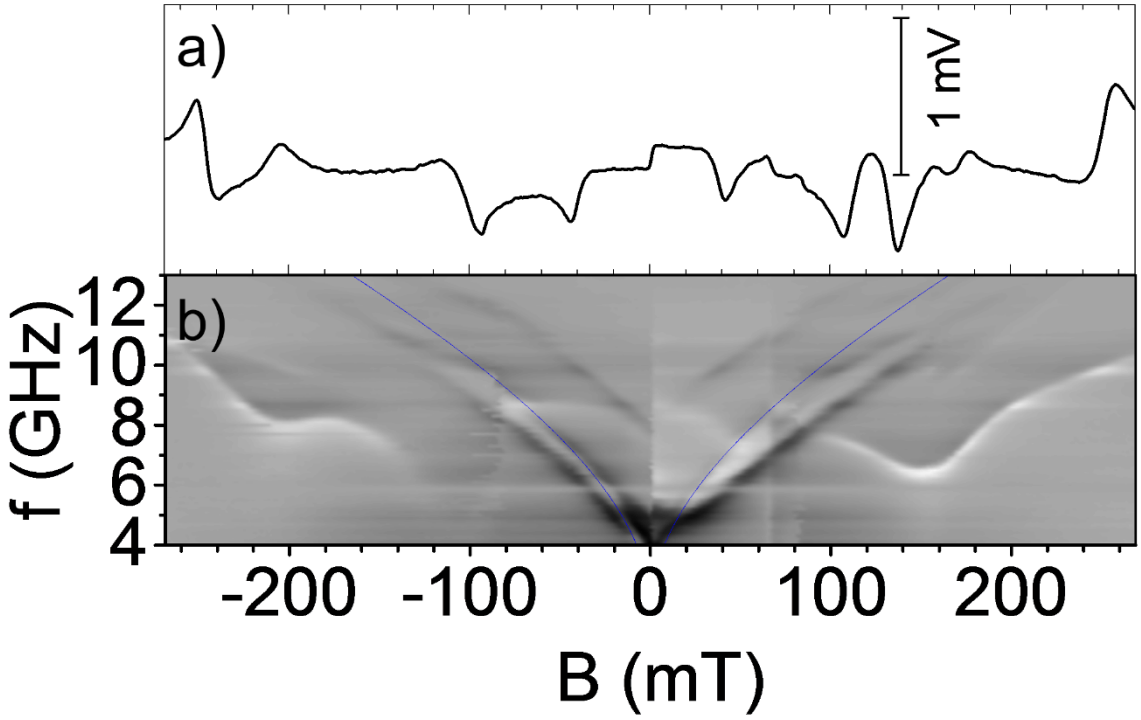

Figure 2.2: **(**a) FMR V_ω(B) spectrum recorded at 3 mV dc bias and 10 GHz rf current (14 dBm). (b) The grey density plot shows FMR spectra at different frequencies (brighter color indicates larger V_ω). Solid blue curve is the Kittel's fit (Eq. 1).

As discussed in the work by Helmer et al.[18], the lowest frequency free layer resonance most likely indicates excitations localized near the edge of the MTJ. The higher frequency free layer resonances represent the first and second uniform free layer resonance, respectively. We can see that at low magnetic fields (<20 mT), where intralayer dipole interactions become more significant the first uniform free layer mode and edge mode merge.

We observe a shift of the resonance field as a function of the dc bias applied to the MTJ. Figure 2.3 shows (a) the V_ω(B) spectrum measured at constant (3 mV) bias and (b) the bias dependence of this V_ω(B) spectrum as a grey density plot (brighter color indicates larger V_ω). The shift of the free layer FMR (at around ±100 mT) and of other resonances

is obvious. The shift is quadratic with respect to the bias and can be associated with the out-of-plane VCMA induced by the dc bias.[19-20]

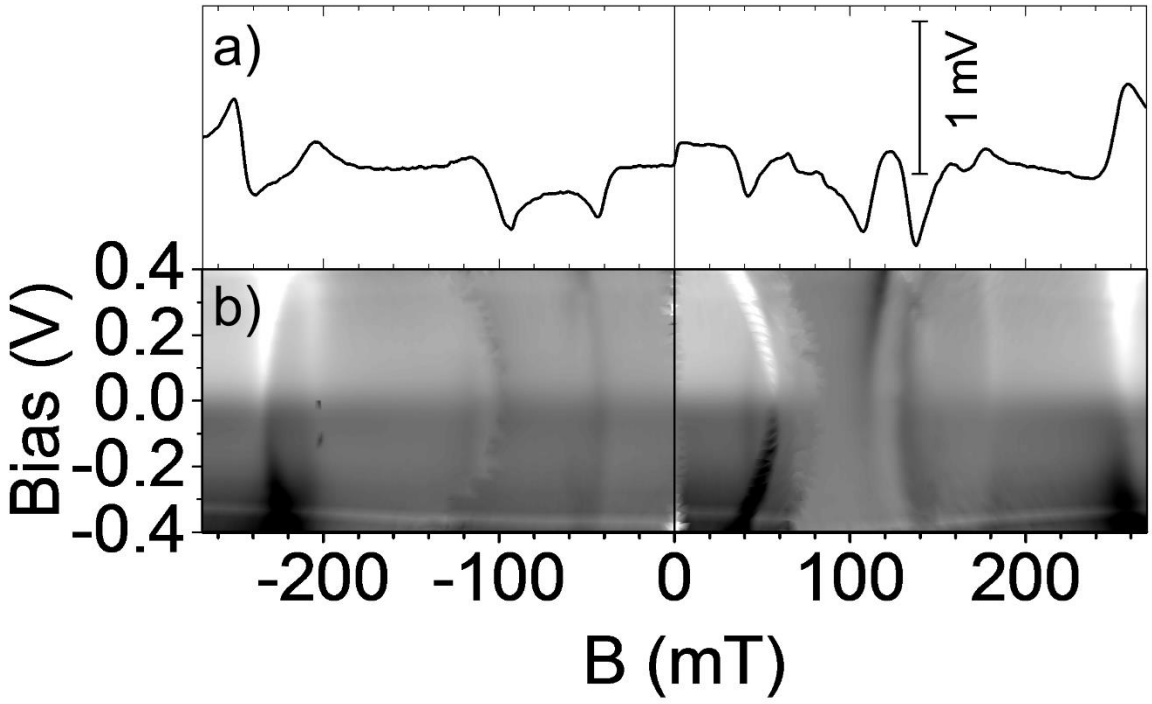

Figure 2.3: (a) $V_\omega(B)$ spectrum measured at constant (10 mV) bias and (b) the bias dependence of this $V_\omega(B)$ spectrum as a grey density plot (brighter color indicates larger V_ω). The frequency of applied microwaves is 10 GHz (14 dBm).

Figure 2.4 shows the dc bias dependence of the resonance field and VCMA energy density per unit area extracted from the bias dependent $V_\omega(H)$ spectra of Figure 2.3. The observed shift is quadratic with a maximum magnitude of approximately $4\ \mu J/m^2$ at 0.5 V. The quadratic fit is $K_1 t(E) = 8.2\ V^2 + 0.9V$.

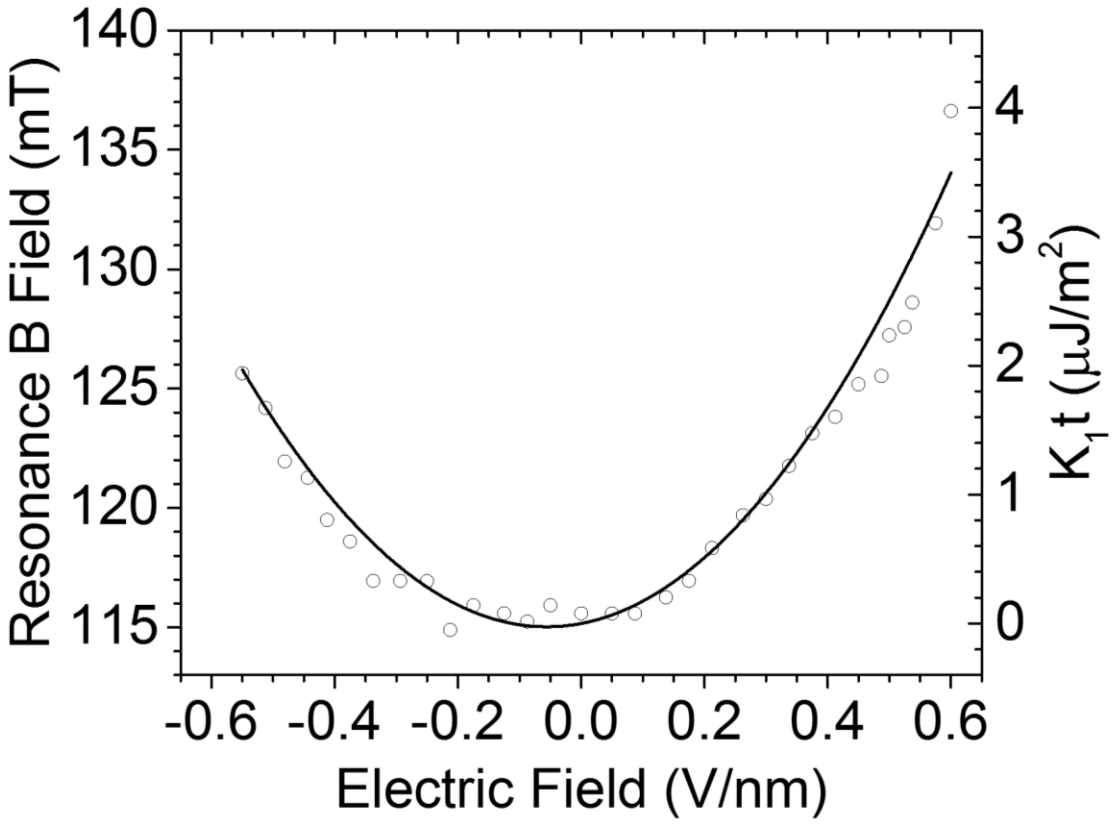

Figure 2.4: Shift of the resonance (left scale) and the VCMA energy density per unit area (right scale) plotted as a function of applied bias. Solid curve is the quadratic fit.

In addition to the shift of the resonance field, we also measured the amplitude of the free layer resonance peak with respect to the applied bias. As shown in Figure 2.5, the amplitude generally increases at both positive and negative bias, with a rapidly sloping region at positive biases near zero and a plateau region at negative biases near zero.

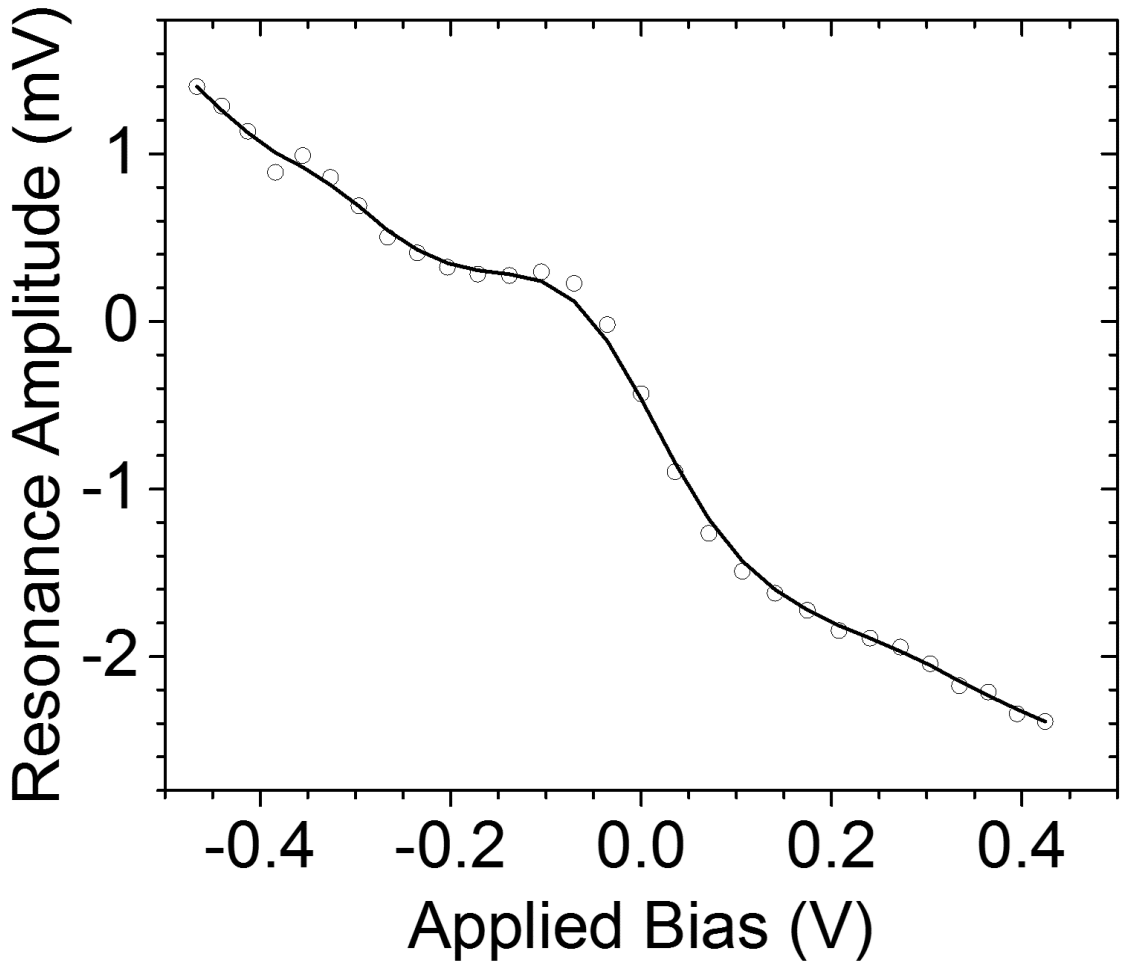

Figure 2.5: Amplitude of free layer FMR peak as function of bias. Solid curve is a guide for the eye.

Measuring the magnetoresistance of the MTJ enables us to extract important information for interpreting the FMR spectra. Figure 2.6(a) shows the magnetoresistance upsweep trace of the MTJ where the magnetic field remains in-plane. The step in resistance at zero field indicates the free layer switching to the parallel state at positive fields. At intermediate fields there is a reorienting of the fixed and reference layers as the system maintains minimum energy. Due to the antiferromagnetic coupling between the fixed and reference layers a spin flop occurs at intermediate fields forcing the device into a high

resistance, anti-parallel state. The tunneling barrier and magnetic spacer between the fixed and reference layers effectively make the device a MTJ-spin valve system in series. This is evidenced by the asymmetry of the magnetoresistance trace. At positive fields, both tunnel junction and the spin valve are in the high resistance states, while at negative fields only the tunnel junction is in the high resistance state. At extreme positive and negative fields the applied magnetic field overcomes the internal fields of the device and forces all the salient magnetizations along the applied direction, resulting in the resistance asymptotically approaching the low resistance value. It should be noted that although fresh devices show 100% magnetoresistance ratios, as shown in Figure 2.6(a) the ratio degrades as the device is subjected repeatedly to high biases. Degradation most likely comes from multiple sources not least of which would be the development of pinholes in the oxide layer.

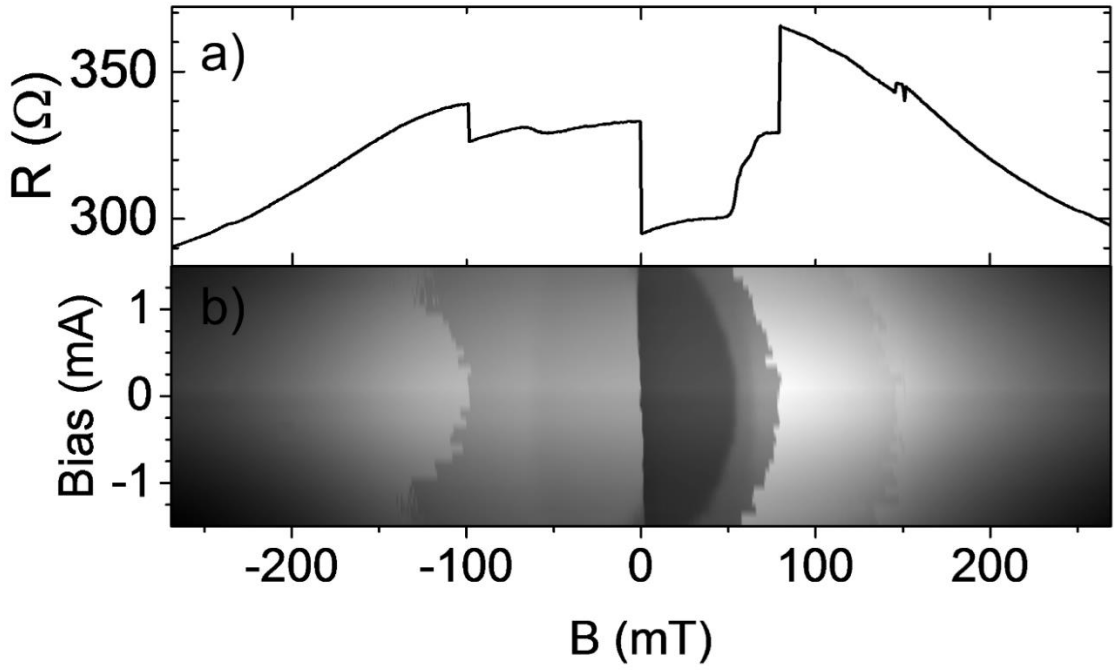

Figure 2.6: (a) Magnetoresistance upsweep trace at 3 mV bias highlighting the changes in device state by abrupt resistance changes. (b) Magnetoresistance gray density plot as a function of applied current bias of the same range as Figure 2.5. A slight linear shift of the free layer coercive field from spin transfer torque is observed as well as large quadratic shifts due to the effect of VCMA on the fixed layer.

Figure 2.7(b) shows the bias dependence of the magnetoresistance with higher resistance corresponding to the brighter areas. Around zero field, the transition from high to low resistance (coercive field) shifts slightly with respect to bias. The high current densities applied to our devices carry spin transfer torques comprised of both a field-like torque and an anti-damping torque. The slight linear shift of the coercive field is a result of the field-like spin transfer torque having a strength of $5.6 \times 10^{-4} \frac{\mathrm{mT}}{\mathrm{mA}}$. Additionally, effects of VCMA can be seen clearly in the shifting field positions of the abrupt resistance changes at intermediate fields which are associated with the switching fixed layer. Furthermore, the commonality of origin of the quadratic shifts in both the dc and FMR measurements is

bolstered by the relative consistency of curvature between the features in each measurement technique. However, interestingly, the curvature of the features changes direction. The quadratic shift associated with the fixed layer curves toward smaller fields, while the free layer shifts toward higher fields. It is possible that this discrepancy in behavior is due to the differing conditions of the electric field at each interface of the tunneling barrier. In that case, VCMA would make a useful tool for strongly diverging ferromagnetic resonances of the free and fixed layers in iMTJs.

2.4 Discussion

As indicated previously, we acknowledge the effect of spin transfer torque on our devices. And it is possible that the FMR shift observed in our experiments with MTJ nanopillars can also be caused by a field-like torque due to the spin-transfer torque (STT) effect. There were previous reports of a quadratic dependence of the field-like torque on bias voltage,[21,22] however we observe a shift in the resonance field that is larger by a factor of 5-10. Nevertheless, due to the high current density in our MTJ nanopillars STT and VCMA are likely to be combined.

2.5 Conclusions

In summary, we investigated voltage controlled magnetic anisotropy (VCMA) in CoFeB/MgO/CoFeB magnetic tunnel junctions (MTJs) with in-plane magnetizations using ferromagnetic resonance (FMR) technique. We observed a quadratic shift in the resonance field as a function of the bias voltage applied to MTJ. These measurements demonstrate the power of FMR to probe VCMA directly in situations where other methods cannot be used. These results are important for understanding magnetodynamics in MTJs with in-plane magnetizations in the presence of VCMA.

2.6 References

[1] F. Matsukura, Y. Tokura, and H. Ohno, *Nature Nanotechnology* **10,** 209–220 (2015).
[2] S. Kanai, M. Yamanouchi, S. Ikeda, Y. Nakatani, F. Matsukura, and H. Ohno, *Applied Physics Letters* **101,** 122403(2012).
[3] A. Okada, S. Kanai, M. Yamanouchi, S. Ikeda, F. Matsukura, and H. Ohno, *Applied Physics Letters* **105,** 052415 (2014).
[4] J. Zhu, J. A. Katine, G. E. Rowlands, Y. J. Chen, Z. Duan, J. G. Alzate, P. Upadhyaya, J. Langer, P. K. Amiri, K. L. Wang, and I. N. Krivorotov, *Physical Review Letters* **108,** 197203 (2012).
[5] K. Miura, *et al., Scientific Reports.* **7**, 42511 (2017).
[6] T. Nozaki, et al., *App. Phys. Lett.* **96,** 022506 (2010).
[7] W.-G. Wang, et al., *Nat. Mater.* **11,** (2012).
[8] J. G. Alzate, et al., *Proc. 2012 IEEE IEDM* 13384152 (2012).
[9] Y. Shiota, et al., *App. Phys. Express* **2,** (2009).
[10] T. Maruyama, et al., *Nat. Nanotechnol.* **4,** (2009).
[11] M. Endo, et al., *App. Phys. Lett.* **96,** 212503 (2010).
[12] H. Almasi, M. Xu, Y. Xu, T. Newhouse-Illige, and W. G. Wang, *Applied Physics Letters* **109,** 032401 (2016)
[13] H. Zhao, A. Lyle, Y. Zhang, P.K Amiri, G. Rowlands, Z. Zeng, J. Katine, H. Jiang, K. Galatsis, K. L. Wang, I. N. Krivorotov, and J.-P. Wang, *Journal of Applied Physics* **109,** 07C720 (2011)
[14] A. A. Tulapurkar, Y. Suzuki, A. Fukushima, H. Kubota, H. Maehara, K. Tsunekawa, D. D. Djayaprawira, N. Watanabe, and S. Yuasa, *Nature* **438,** 339–342 (2005).
[15] J. C. Sankey, P. M. Braganca, A. G. F. Garcia, I. N. Krivorotov, R. A. Buhrman, and D.C. Ralph, *Physical Review Letters***96,**227601(2006).
[16] T. Staudacher and M. Tsoi, *Journal of Applied Physics* **109,** 07C912(2011).
[17] H. Seinige, C. Wang, and M. Tsoi, *Journal of Applied Physics* **117,** 17C507 (2015).
[18] A. Helmer, S. Cornelissen, T. Devolder, J.-V. Kim, W. van Roy, L. Lagae, and C. Chappert, *Physical Review B* **81,** 094416 (2010).
[19] L. Xu and S. Zhang, *Journal of Applied Physics* **111,** 07C501 (2012).
[20] S. E. Barnes, J. Ieda, and S. Maekawa, *Scientific Reports* **4,** 4105 (2014).
[21] J. C. Sankey, *et al.*, *Nature Physics* **4,** 67–71 (2008)
[22] H. Kubota, *et al.*, *Nature Physics* **4,** 37–41 (2008)

C H A P T E R III

ENERGY LANDSCAPE OF RESISTIVE SWITCHING IN $Sr_3Ir_2O_7$

3.1 Thermal Activation over an Energy Barrier

Thermal activation is a well-known phenomenon that has been used extensively as a tool in material science to probe reaction kinetics such as oxidation, diffusion, and material band gaps. Methods that use thermal activation rely on the premise that under equilibrium conditions the state variable of a system sits in an energy well responding to small perturbations to its energy caused by temperature induced random fluctuations. An energy barrier associated with the specific process under study prevents the system from achieving a lower energy beyond the barrier. However, thermal fluctuations jostle the

system such that there is a nonzero probability that the random exchanges of energy add constructively so that the system overcomes the barrier. The undulations of the energy with respect to position characterized by barriers and wells constitute what is sometimes called the energy landscape.

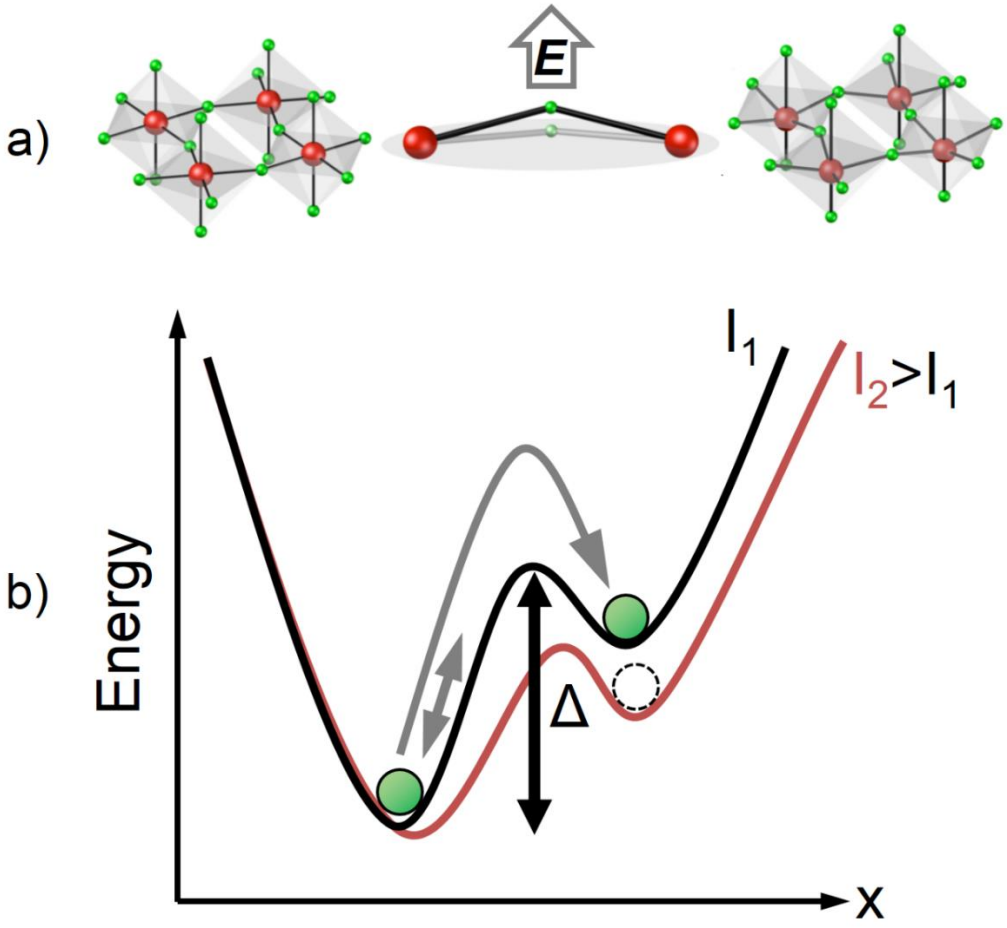

Figure 3.1: (a) In the presence of an electric field, *E*, applied along the crystal *c* axis the oxygen atoms are displaced such that the bonds between the oxygen (green) and iridium atoms (red) rotate from their equilibrium angle of ~12°. (b) In black: A general depiction of the potential energy variation as a function of position in a system exhibiting an energy barrier with height Δ. Gray arrows show small and large changes in the system state due to thermal fluctuations. The red curve depicts a nearby variation of the energy landscape achieved by changing a parameter I_1.

In the transition metal oxide under study, $Sr_3Ir_2O_7$, an electrical bias with an associated electric field, *E*, and current, I_1, distorts the crystal lattice by displacing the oxygen ions as depicted in Figure 3.1(a) enabling electrically tunable transport. Figure°3.1(b) shows a general picture of the thermal activation process, where an energy barrier with height, Δ, separates two local energy minima hosting the system state variable, in this case oxygen ion position, represented here as green circles. The gray double-ended arrow represents small ($E_{Thermal} << \Delta$) thermal fluctuations, while the large arrow denotes a successful crossing of the energy barrier ($E_{Thermal} > \Delta$). Variational shifts of the energy landscape, depicted here by the shift from the black curve associated with I_1 to the red curve associated with I_2, can be induced by changes in the system parameters. As a result, energy landscape variations can shift local minima as indicated by the dashed circle in Figure 3.1(b).

The probability for a system to overcome an energy barrier has the following form,

$$P = e^{\frac{-\Delta}{k_B T}} \tag{3.1}$$

where k_B is the Boltzmann constant and *T* is absolute temperature. From this equation, we can see that there is an exponential dependence of the probability on the energy barrier such that at constant temperature as the energy barrier increases the probability decreases. However, increasing the temperature can counteract the effect of a greater energy barrier. In chemical kinetics the probability can be translated to a reaction rate by multiplying by an attempt frequency *A*, also called the pre-exponential factor.

$$k = Ae^{\frac{-E_a}{k_B T}} \tag{3.2}$$

where k denotes the chemical rate constant, and E_a indicates the activation energy. For fitting purposes, this equation is typically written in its linear form,

$$ln\,k = ln\,A - \frac{E_a}{k_B}\left(\frac{1}{T}\right) \tag{3.3}$$

in order to plot $\ln k\, vs\, \frac{1}{T}$ and extract the slope and intercept to specify E_a and A. This technique is also regularly used to extract the band gap of semiconductors. At low temperatures the most significant carriers of current are thermally activated electrons (holes) which cross the band gap into the conduction (valence) band. The thermally excited carriers have a direct effect on the measured conductivity of the device and therefore the resistance, R. In that case, the associated thermal activation equations become,

$$R = Ae^{\frac{-E_g}{2k_B T}} \tag{3.4}$$

$$ln\,R = ln\,A - \frac{E_g}{2k_B}\left(\frac{1}{T}\right) \tag{3.5}$$

where E_g is the band gap and the factor of 1/2 in the exponent comes from the fact that both the conduction and valence bands are $E_g/2$ from the Fermi energy in an undoped semiconductor. Thermal activation measurements are typically made over a large range of temperatures in so-called Arrhenius plots, where varying the temperature allows one to fit the pre-exponential factor and the energy barrier.

In our measurements, instead of converting the probability into a chemical reaction rate or a resistance, we construct a delay time governed by the exponential probability dependence. Using this delay time measurement, we probe the energy barrier associated with the resistive switching transition. We observe an exponential dependence of the

switching probability on both electric bias and temperature consistent with thermal activation over an energy barrier. And we quantify the changes in the energy barrier height with respect to the applied bias to find a linear decrease of the barrier with increasing bias. Our observations elucidate the activation picture of resistive switching in Mott insulators and support the potential of antiferromagnetic transition metal oxides for spintronic applications.

3.2 Experimental Setup

Single crystals of $Sr_3Ir_2O_7$ were synthesized for this work using a self-flux technique.[1] The technique results in single crystalline flakes of $Sr_3Ir_2O_7$ with thicknesses of about 0.2-mm and the [001] c-axis oriented perpendicular to the flake's surface (area ~0.5×0.5 mm^2). Single crystal X-ray diffraction was employed to determine the crystal structure of the flakes. As shown in Figure 3.2, Ag paste and In metal contacts (area ~0.2×0.2 mm^2) on top and bottom surfaces of $Sr_3Ir_2O_7$ flakes were used to supply and sink electrical currents (up to 15 mA). The contacts were made by first preparing ~12 cm lengths of 39 AWG copper wire in which the final 3mm of insulation was stripped. The sample was then mounted to the inner conductor of the coaxial cable connecting the sample to the circuit on a small bed of Ag paste. A small drop of Ag paste was applied to the top of the sample and was allowed to dry with the prepared copper wire embedded in the Ag paste. In the case of In contacts, no adhesive chemical was used. The 39 AWG wire was simply sandwiched between two small In pads of sizes proportional to the Ag contacts. The natural softness of In provided the compliancy to adhere the wire to the sample. However, although such In contacts were used in data collection, the data we show in this chapter is exclusively using Ag paste contacts.

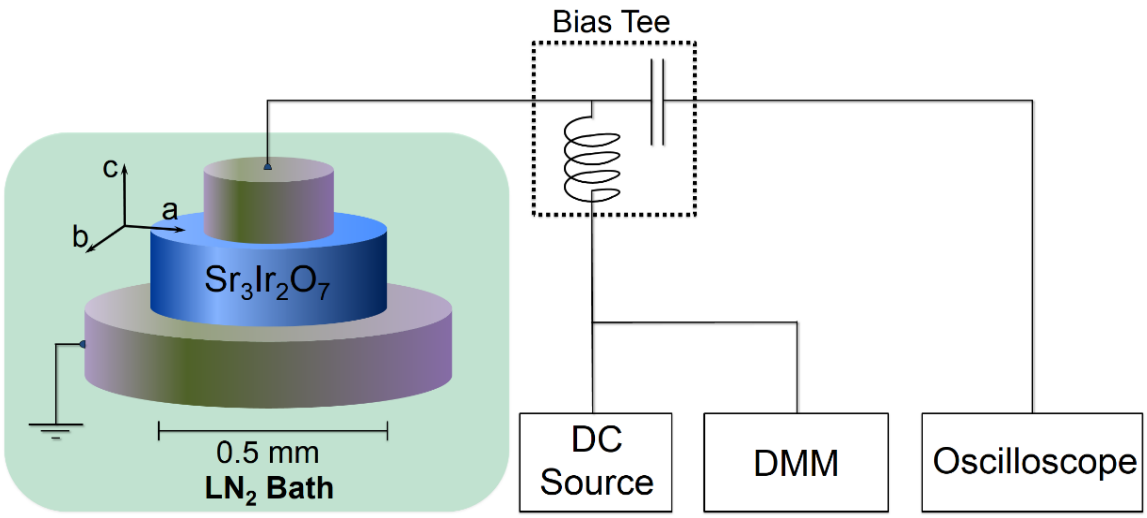

Figure 3.2: Experimental setup consists of the $Sr_3Ir_2O_7$ sample in liquid nitrogen with Ag paste electrical contacts connecting a current source and digital multimeter (DMM). An oscilloscope probes the time domain response of the application of abrupt steps in dc bias.

In such a 2-probe geometry the applied currents flow (primarily) along the [001] c-axis of the crystal and were shown previously[2, 3] to trigger a resistive switching at sufficiently high electrical bias. A wideband bias tee separates the ac and dc sides of the circuit. A dc current source (Keithley 2400) was used to bias the sample in order to initiate resistive switching while a digital multimeter (Keithley 2000) measures the voltage across the sample. On the ac side of the circuit a real-time (4GS/s) oscilloscope (Teledyne LeCroy Wavesurfer 3034) records the voltage signal across the sample with respect to time.

The sample is mounted on a sample holder and placed in a Janis STVP cryostat chamber. Liquid nitrogen is then pumped into the chamber until full. The cryostat is normally open to the atmosphere where nitrogen boil off permits the sample to be immersed for ~1.5 days. The switching is monitored by transport measurements– current-voltage (*I*-*V*) characteristics of the crystal were measured with the sample in liquid nitrogen

(LN_2) in the temperature range from 77-80 K. The temperature control in this range was achieved by varying the LN_2 pressure from 750-1020 Torr using an adjustable pressure relief valve (Straval 2-25 PSIG) on the LN_2 cryostat exhaust as shown in Figure 3.3. The pressure relief valve is controlled using a screw situated at the top that interfaces with a spring in contact with a membrane governing the flow of gaseous nitrogen.

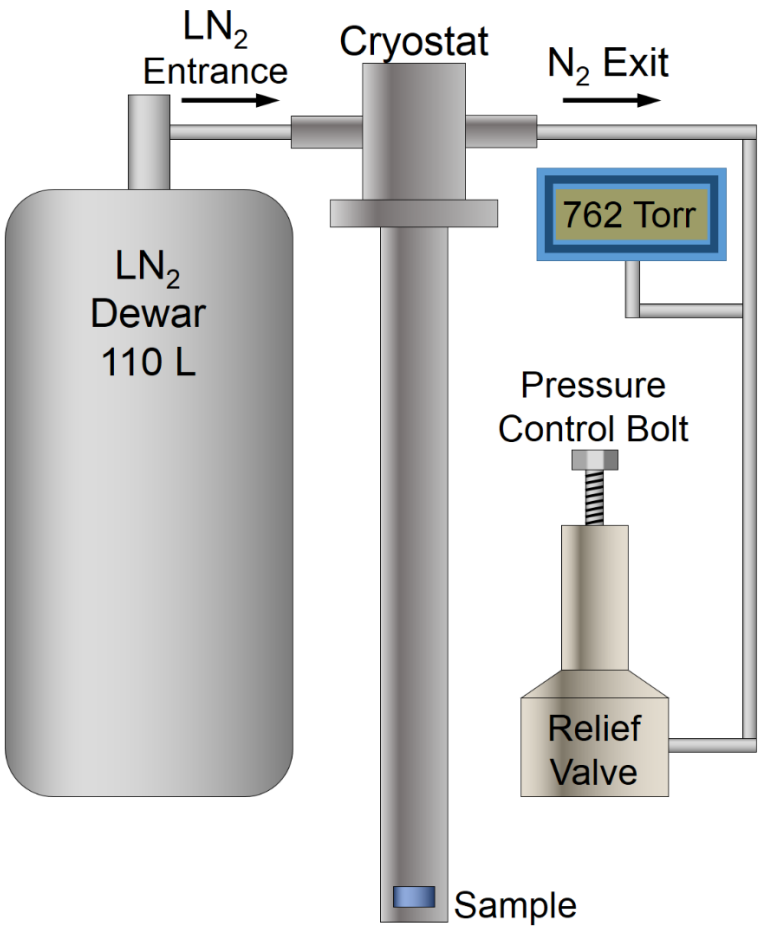

Figure 3.3: Pressure regulation of the cryostat system permits temperature control over the range 77-80 K. System is not exercised in a continuous flow condition. A valve on the LN_2 dewar allows the cryostat to be filled. The LN_2 flow is then stopped and measurements can be executed for ~1.5 days until the LN_2 surface level reaches the sample.

As shown in Figure 3.4, the relationship between the rotational angle of the screw and the resultant pressure is nonlinear, showing more resemblance to a sigmoidal function as opposed to a quadratic curve expected from the action of the spring regulator. The well-known relationship between LN_2 vapor pressure and temperature[4] was used to convert the regulated pressure to sample temperature, assuming convectively assisted thermal equilibrium between the sample and the surrounding LN_2.

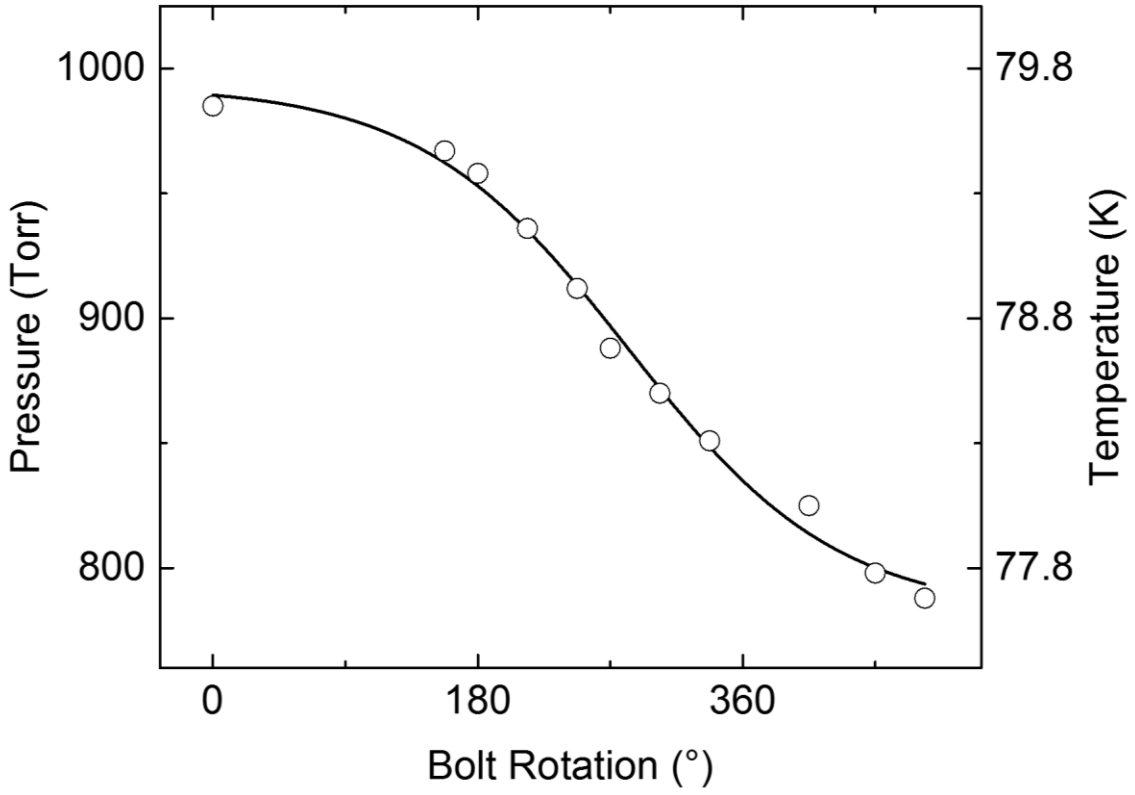

Figure 3.4: Calibration for the pressure relief valve shows nonlinear dependence on the control bolt rotational angle. Sigmoid curve is a guide for the eye. Vapor pressure is converted to temperature on the right axis. Care was taken to achieve a relatively uniform temperature spacing. The time dependent LN_2 column pressure is added to the pressure measured at the cryostat exit.

The pressure caused by the weight of the column of liquid nitrogen was not ignored. At a density of 808 kg/m^3 the maximum height of the column of 1.016 m results in an increase in pressure of 60 Torr, equating to 0.6 K increase in temperature at the sample. In the same sense, the gradual change in temperature due to LN_2 boil-off was also taken into account. These effects necessitated careful calibration in order to visit various temperatures with relatively uniform spacing.

A custom National Instruments LabView program coordinates the various instruments to supply current and measure voltage and signals with special care required for managing the oscilloscope concerning synchronization and data extraction. Figure 3.5 depicts the data collection process.

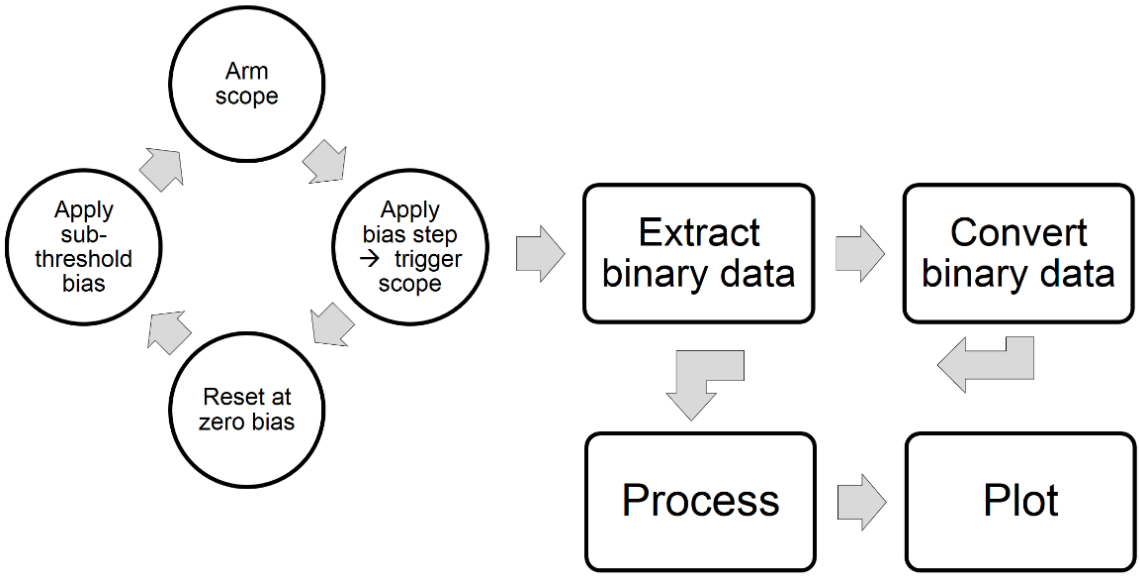

Figure 3.5: Process flow for data collection requiring current source/oscilloscope synchronization and binary data extraction, conversion, processing, and plotting. Synchronization, extraction, and conversion were implemented in LabView; MATLAB was used for processing while plotting was executed in OriginLab.

First, an electrical bias is applied to the sample that is slightly below the threshold bias required for switching. Then LabView sends a GPIB command to arm the oscilloscope to start recording when the voltage signal reaches the trigger level. The source supplies an abrupt step in bias that triggers the scope, then initiates resistive switching to the high resistance state after some delay time. The delay time conceptually represents a notion similar to the decay time associated with the probabilistic processes governing radioactive decay. The source then decreases the bias to zero to reset the sample to the low resistance state for the next data point ~1 second later. The oscilloscope is able to send the waveform to the computer for analysis, but normally uses an ascii type data file. With 10 kilopoint data sampling the ASCII file is ~10 MB, severely limiting the rate at which data can be taken since the data must be offloaded from the oscilloscope after every triggered trace, a ~5 second process. In order to increase the data collection rate, we instead send the waveform to the computer in a binary format which measured ~300 KB. This required a decoding step to be implemented after the completion of the measurement and the meticulous task of translating the particular Teledyne LeCroy binary format to a readable data file for processing in MATLAB. Once converted in LabView, the data is imported into MATLAB where a custom program (Appendix A) extracts the individual delay times accounting for the capacitive discharge effect associated with the AC coupling mode of the oscilloscope as shown in Figure 3.6. Data is then imported for analysis and graphing to OriginLab.

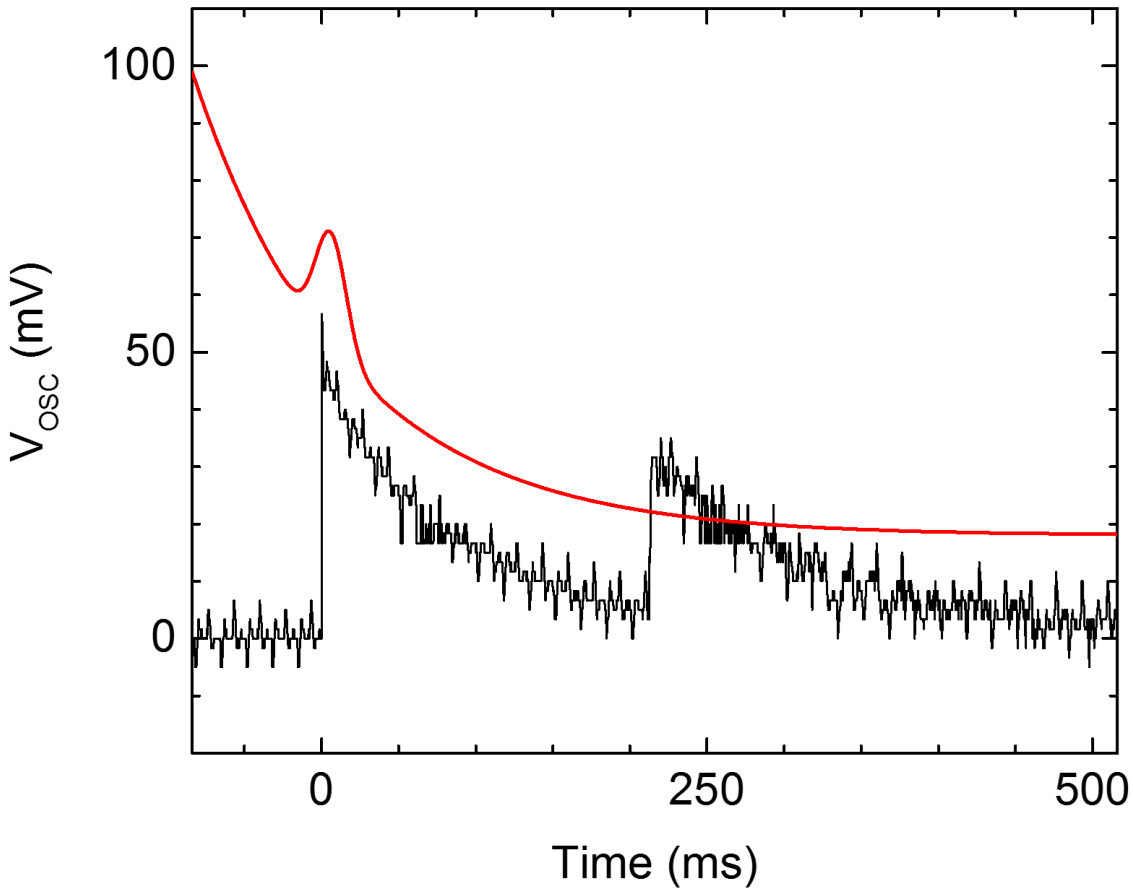

Figure 3.6: Example of the MATLAB processing method used for extracting the delay time at 8.415 mA of 215 ms. The black line is the raw voltage reading from the oscilloscope; the first (second) step is created by the applied current (resistive switching.) Additionally, we can see both a large 60 Hz line voltage noise and the charge decay from the AC coupling mode of the oscilloscope. The red curve serves as a "cutting" function, the intersection of the black and red lines denotes that resistive switching occurred. Note the bump in the "cutting" curve meant to avoid the applied current voltage step.

3.3 Bias Dependence Results

Figure 3.7 shows a representative current-voltage (*I*-*V*) characteristic of $Sr_3Ir_2O_7$ measured at 77 K – the crystal resistance *R*=*V*/*I* is shown as a function of the bias current *I*. Here the red and blue curves show the *R*(*I*) for up- and down-sweeps of *I*, respectively. For an increasing bias, both positive and negative, we observe a continuous decrease of the crystal resistance and two locally irreversible switching events to a higher resistance (indicated by arrows in Figure 3.7) at critical biases $I_C \approx \pm 8.5$ mA and ±12.7 mA. For a decreasing bias, only one switching back to a lower resistance is observed at around ±5 mA.

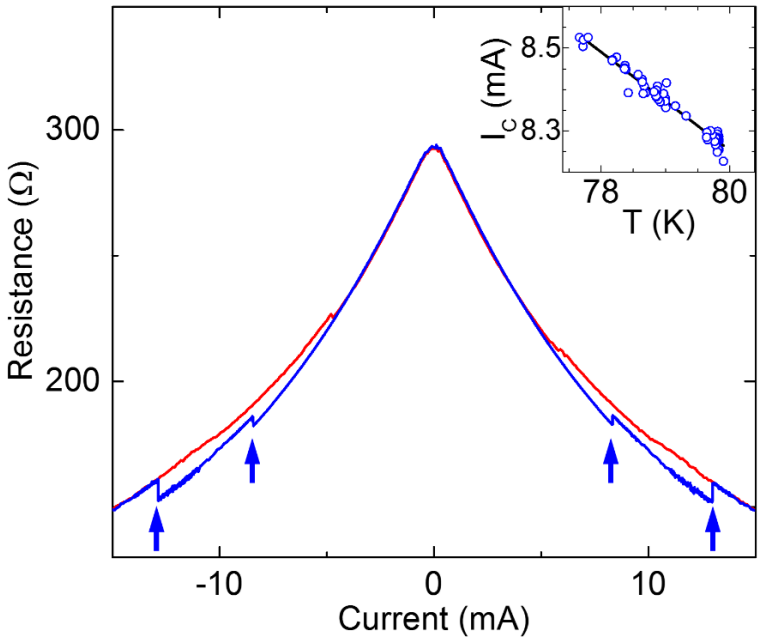

Figure 3.7: (a) Resistive switching in *R*(*I*) characteristic of $Sr_3Ir_2O_7$ (T = 78.6 K). Blue and red traces represent the up- and down-sweeps of *I*, respectively. Arrows indicate switching events. Two switching events to a higher resistance for increasing bias (at I_c=±8.5 mA and ±12.7 mA) and one to a lower resistance for decreasing bias are clearly visible. The inset shows the temperature dependence of the critical current associated with the first switching event at positive bias.

Similar switching characteristics were previously observed in both Sr_2IrO_4 and $Sr_3Ir_2O_7$[2, 3] where the continuous/irreversible changes in resistance were associated with electric-field driven lattice distortions/structural transition. The inset to Figure 3.7 shows the temperature dependence of the critical current associated with the lower-bias switching event at around 8.5 mA. Increasing the temperature of the sample has the effect of decreasing the critical bias current with a linear dependence quantified by 119 ± 3 μA/K.

Next we investigate the onset of the resistive switching in the time domain. We will focus on the lower-bias switching event around 8.5 mA (see Figure 3.7). The procedure for triggering the switching consisted of slowly increasing the applied electrical bias from zero to a value (usually 8 mA) well below I_C and then abruptly (~150 μs) increasing the applied bias to a value above I_C. This abrupt jump in bias naturally produces an increase in the voltage across the crystal which has been used to trigger the oscilloscope. Figure 3.8(b) shows the resulting time evolution of voltage V_{OSC} across the sample measured by oscilloscope for a bias jump from 8 mA to 9.17 mA. Here the first rise in the oscilloscope voltage V_{OSC} at 0 ms is associated with the abrupt current jump from 8 to 9.17 mA; the current jumps and produces the rise in V_{OSC} but the switching has not yet occurred. The switching is delayed and will happen a little later. We can clearly see a second rise in V_{OSC} at about 50 ms which is produced by an increase in the sample resistance (switching) which occurs with a delay $\tau \approx 50$ ms after the current jump. The time signature of such salient events are depicted in Figure 3.8(a). This increase in resistance corresponds to the increase in *R(I)* at 8.5 mA in Figure 3.7. We thus conclude that the resistive switching requires a certain time τ at a given bias ($I = 9.17$ mA). We have repeated the above measurement 600 times and found a distribution of delay times shown in Figure°3.8(c). The associated Poisson fit (solid curve in Figure 3.8(c)) suggests that on average the switching at $I = 9.17$ mA is delayed by about 50 ms.

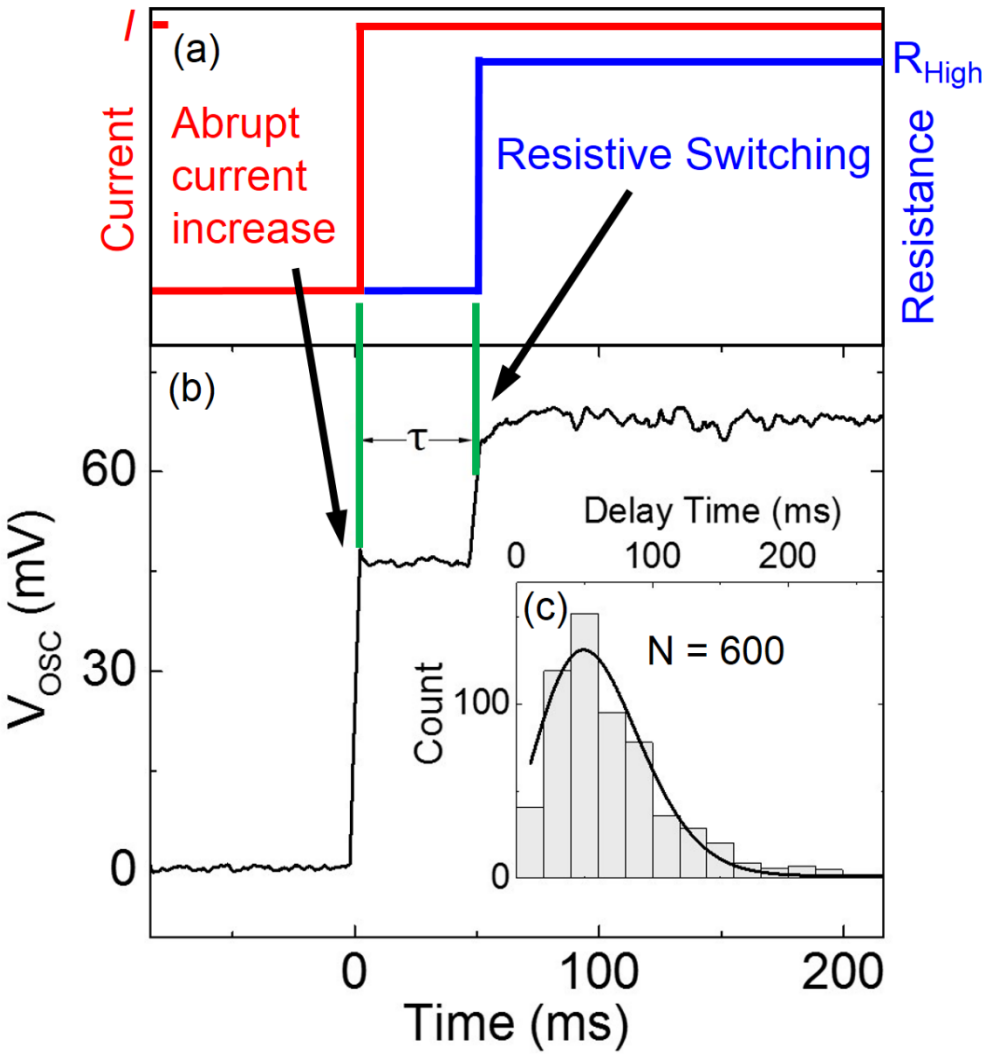

Figure 3.8: (a) A graph of the salient events capturing one data point including the current increase in red and resistive switching in blue. (b) A time trace of the process of switching from low bias to the '1st high-resistance' state. The vertical axis plots the voltage across the sample captured with an oscilloscope where the first abrupt increase is caused by a sudden rise in applied current. After a time, τ, the switching occurs resulting in a second abrupt rise in measured voltage due to an increase in sample resistance indicating that switching has occurred. (c) The results of the mentioned measurement repeated 600 times. A histogram corresponding to the relative frequency of measured delay time values is plotted with a Poisson fit.

3.4 Bias Dependence Discussion

We can use the measured delay time to determine the activation energy of switching. As discussed before, a simple model where the switching is associated with overcoming an energy barrier Δ implies the Arrhenius equation for the delay time:

$$\tau = \tau_0 \, e^{\frac{\Delta}{k_B T}} \tag{3.6}$$

with τ_0 the attempt time (reciprocal of the attempt frequency), k_B Boltzmann constant, and T temperature. Assuming τ_0 = 1 ns and using T = 77 K in our experiment, this analysis yields Δ = 50 meV. While the exact value of τ_0 in our system is unknown, this analysis provides a reasonable estimation of Δ, since decreasing τ_0 by as much as three orders of magnitude (to 1 ps) would increase Δ by only 20 meV. In contrast, the variation of the energy barrier Δ with respect to the applied bias current I can be characterized exactly as we show next.

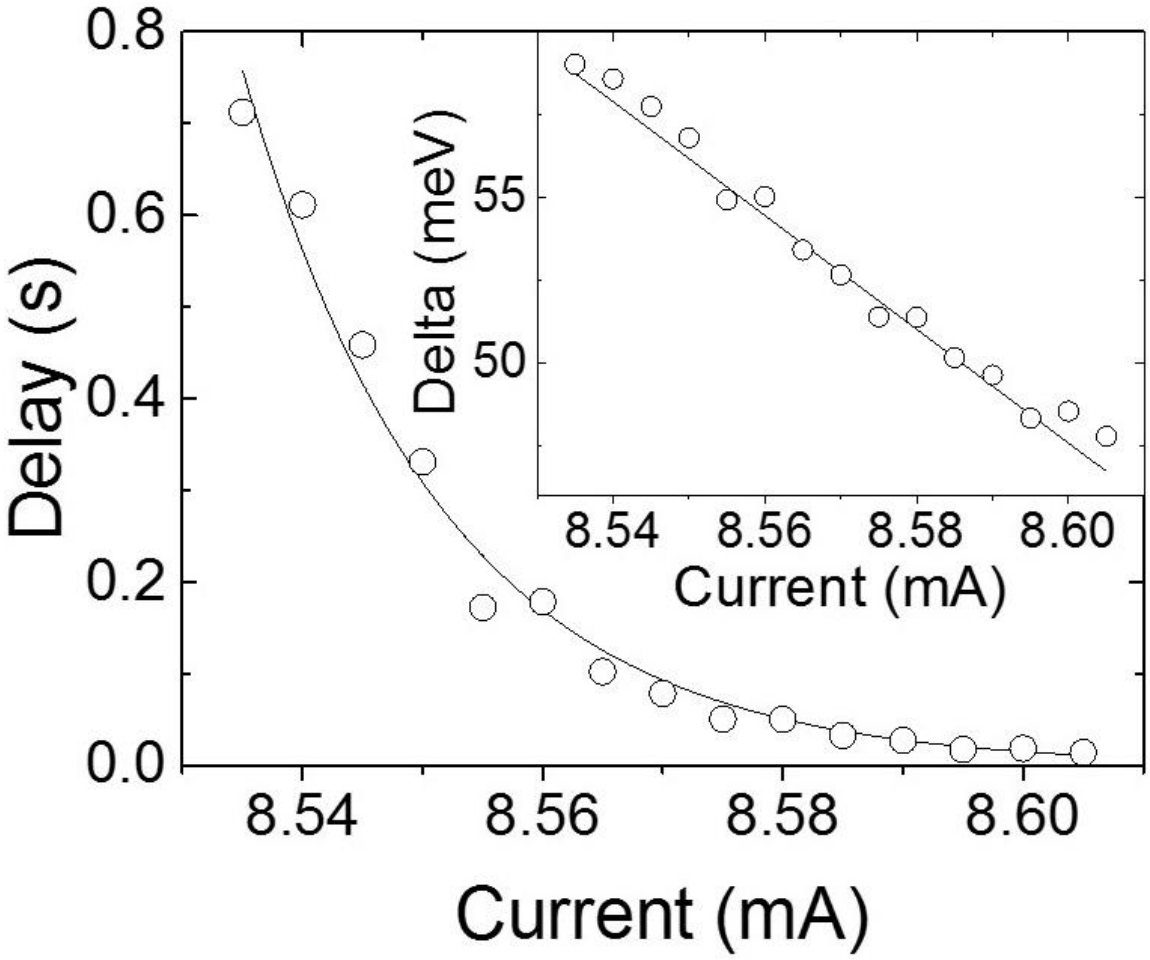

Figure 3.9: (a) Average delay time between application of current step and resistive switching as a function of the final bias measured at 77 K, repeated 20 times at each bias. All switching events were executed from a beginning bias of 8.0 mA. Solid line shows exponential fit. The inset depicts the change in the barrier height, Δ, as a function of the final bias with a linear fit corresponding to a modulation of 172 meV/mA.

The procedure for finding the average delay time at a given switching current *I* was repeated for different *I*'s. These measurements have provided the *τ(I)* dependence displayed in Figure 3.9. Here open symbols show that the delay time increases significantly with decreasing bias current *I*. By applying Eq. 3.1 to every τ data point in Figure 3.9 we have reconstructed the dependence of Δ on *I*. The inset to Figure 3.9 shows that the energy

barrier Δ decreases approximately linearly with the applied bias current *I* (see the linear fit in Figure 3.9 inset). This result correlates with the field-effect model, which was used to explain the linear relationship between the activation energy and applied electrical bias observed in $Sr_3Ir_2O_7$.[3] The field-effect model suggests that the switching barrier in Eq. 1 can be expressed as a function of the applied bias as:

$$\Delta = \Delta_0 - \gamma I \qquad (3.7)$$

where Δ_0 is the barrier at zero *I* and γ is the parameter which characterizes the strength of the field effect. From the linear data fit in Figure 3.9 inset we now define the γ parameter – 172 eV/A. Using this parameter, we have successfully fitted the *τ(I)* data in Figure 3.9 (see solid curve) by an exponential function which combines Eqs. 1 and 2:

$$\tau = \tau_0 \, e^{\frac{\Delta_0 - \gamma I}{k_B T}} \qquad (3.8)$$

Note that the effect of Joule heating can be ruled out as a possible source of Δ-variations in our experiment. In Figure 3.9 we observe a strong variation of the delay time τ as a function of the bias current – the delay time changes by a factor of ≈50. If triggered by temperature alone, the 50-fold decrease of τ requires an increase in temperature by about 50% (Eq. 1). The actual increase of the bias current (<0.8% in Figure 3.9) increases the Joule heating power by less than 0.64% and can only increase the sample temperature by less than ~1%. We thus conclude that Joule heating cannot explain our observations in Figure 3.9; it is in fact due to the effect of electric bias on τ.

We have also verified experimentally that the resistive switching (Figure 3.7) and its thermal-activation behavior (Figures 3.8 and 3.9) are not affected by an externally

applied magnetic field up to 0.25 T (maximum field available in our experiments). This result is in agreement with previous observations of zero magnetotransport response in $Sr_3Ir_2O_7$.[3]

3.5 Temperature Dependence

Now we can verify Eq. 3.3 by performing our experiment at different temperatures. In our set-up the sample is immersed in liquid nitrogen to maximize the heat removal and minimize any Joule heating from high bias currents. The sample temperature can be accurately controlled in the range from 77-80 K by controlling the pressure (from 750-1020 Torr) in the nitrogen cryostat using an adjustable pressure relief valve.

Figure 3.10(a) shows the average switching delay vs applied bias (as in Figure 3.9) measured at eleven different temperatures in the range from 77-80 K. Eq. 3 was successfully used to fit the data at different temperatures (see solid curves); the curves shift to the left with increasing temperature. Using Eq. 3.1 we have reconstructed $\Delta(I)$ for different temperatures which are shown in Figure 3.10(b) with the corresponding linear fits. Using the fits for Δ, we can define an effective current, I_{eff}, that represents the temperature variation of an average delay time associated with a particular value of Δ. Figure 3.10(c) shows $I_{eff}(T)$ for $\Delta = 50$ meV.

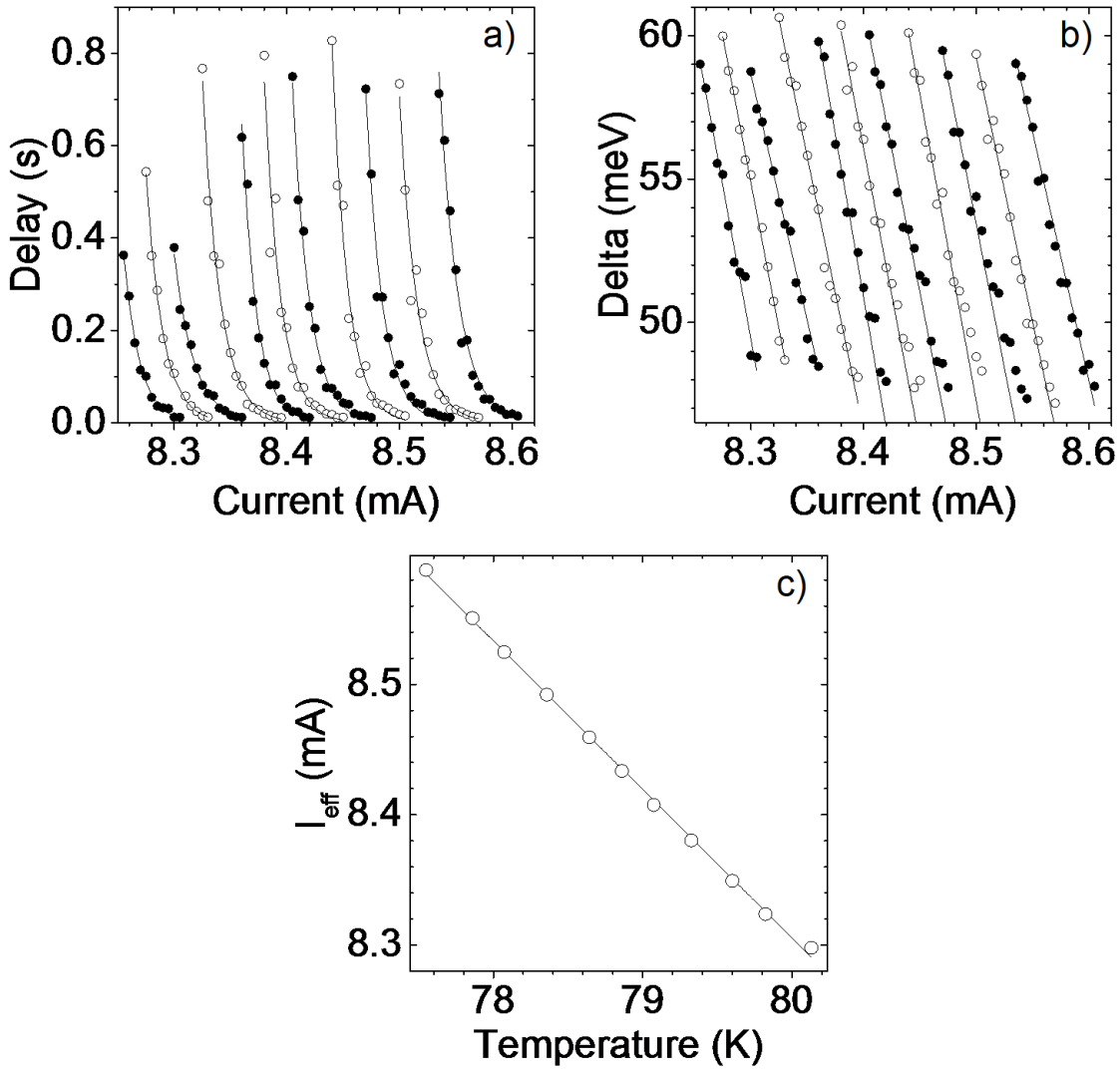

Figure 3.10: (a) Temperature effects of the average delay measurement shown in Figure 3.9. Temperatures range from 77 K at the rightmost curve to 80 K at the leftmost curve. Black and white symbols serve to separate data associated with neighboring temperatures. (b) Delta calculated as a function of temperature (τ_0 = 1 ns). (c) The change in the current, I_{eff} associated with delta equal to 50 meV, as a function of temperature with a linear fit corresponding to a variation of 110 ± 1 μA/K.

The temperature dependent variation of I_{eff} is analogous to the previous temperature-dependent measurement of the critical switching current I_C. Indeed, the slope of $I_{eff}(T)$ – 110 ± 1 μA/K, is comparable to the slope of $I_C(T)$ – 119 ± 3 μA/K. We should note that our method to control the temperature may cause some of the observed effects to be associated with the pressure variations. It is possible that the changes we observed in transport properties of our samples are caused directly by the pressure. However, given a very large magnitude of pressure (on the order of GPa) needed to induce transport effects in iridates,[5-8] we estimate the effects from pressure on the order of an atmosphere to be negligible. Therefore, we attribute the changes observed in Fig. 3.10 in Δ to the effect of temperature on Δ_0 while the bias-dependent component of Δ characterized by γ varies very little in the above temperature range (77–80 K).

3.6 Conclusions

In summary, we have investigated the energy landscape of bias induced resistive switching in antiferromagnetic $Sr_3Ir_2O_7$. Using time-based transport measurements, a bias and temperature dependent switching delay time was observed. A model based on thermally assisted transitions over an energy barrier was used to explain the observed behavior. The energy barrier's dependence on applied bias and temperature was quantified. An electric field effect model describing induced structural modifications can be used to explain both discontinuous changes in $Sr_3Ir_2O_7$[9] resistance and well as previously demonstrated electrically tunable transport in $Sr_3Ir_2O_7$ and Sr_2IrO_4.[2, 10]

3.7 References

[1] G. Cao, Y. Xin, C. S. Alexander, J. E. Crow, P. Schlottmann, M. K. Crawford, R. L. Harlow, and W. Marshall, *Phys. Rev. B* **66**, 214412 (2002).

[2] C. Wang, H. Seinige, G. Cao, J.-S. Zhou, J. B. Goodenough, and M. Tsoi, *Phys. Rev. B* **92**, 115136 (2015).

[3] H. Seinige, M. Williamson, S. Shen, C. Wang, G. Cao, J.-S. Zhou, J. B. Goodenough, and M. Tsoi, *Phys. Rev. B* **94**, 214434 (2016).

[4] J. E. Jensen, W. A. Tuttle, R. B. Stewart, H. Brechna, and A. G. Prodell, *Brookhaven National Laboratories Selected Cryogenic Data Notebook* (BNL, New York, 1980)

[5] D. Haskel, G. Fabbris, Mikhail Zhernenkov, P. P. Kong, C. Q. Jin, G. Cao, and M. van Veenendaal, *Phys. Rev. Lett.* **109**, 027204 (2012)

[6] Y. Ding, L. Yang, C.-C. Chen, H.-S. Kim, M. J. Han, W. Luo, Z. Feng, M. Upton, D. Casa, J. Kim, T. Gog, Z. Zeng, G. Cao, H. Mao, and M. Veenendaal, *Phys. Rev. Lett.* **116**, 216402 (2016)

[7] D. A. Zocco, J. J. Hamlin, B. D. White, B. J. Kim, J. R. Jeffries, S. T. Weir, Y. K. Vohra, J. W. Allen, and M. B. Maple, *J. Phys. Condens. Matter* **26**, 255603 (2014).

[8] C. Donnerer, Z. Feng, J. G. Vale, S. N. Andreev, I. V. Solovyev, E. C. Hunter, M. Hanfland, R. S. Perry, H. M. Rønnow, M. I. McMahon, V. V. Mazurenko, and D. F. McMorrow, *Phys. Rev. B* **93**, 174118 (2016).

[9] M. Williamson, S. Shen, G. Cao, J.-S. Zhou, J. B. Goodenough, and M. Tsoi, *Phys. Rev. B* **97**, 134431 (2018).

[10] C. Hahn, G. de Loubens, V. V. Naletov, J. B. Youssef, O. Klein and M. Viret, *Europhys. Lett.* **108**, 57005 (2014).

C H A P T E R IV

NOISE MEASUREMENTS IN $Sr_3Ir_2O_7$

4.1 Introduction to Electronic Noises

Electronic noise is generally undesirable randomly fluctuating currents and/or voltages that fundamentally limit the accuracy and sensitivity of measurement systems. It is a concept that was generalized from the audible hissing sound in loudspeakers to inaudible high and low frequency electronic fluctuations that interfere with circuits. Noise is quantified by the power spectral density (PSD), also called the noise spectrum. The power spectral density is the relative distribution of signal power of a stationary random process throughout the spectrum.[1] More technically, the PSD is a real, even, nonnegative

function which yields the total average power per ohm when integrated over the frequency domain, and is typically derived computationally from the Fourier transform of the time domain autocorrelation of the random signal. Although noise is generally seen as an impediment to reading electronic signals, when studied as its own phenomenon it can contain useful information about physical mechanisms which enables the noise signature to be used as a diagnostic tool.[2, 3]

Noise spectra can be categorized by the functional dependence of the amplitude on the frequency into so-called "colors." Noise with equal amplitude over all frequencies is designated as white noise. The naming convention mimics the production of white light from the addition of light of various frequencies at equal intensities. A decreasing (increasing) noise amplitude at higher frequencies designates pink and red (blue and violet) noises where the designations parallel the associated relative intensities of light at the extreme ends of the visible spectrum. The dependence of colored noise as a function of frequency has the form f^{β}, where β takes on the values -2, -1, 0, 1, and 2 for red, pink, white, blue, and violet noises, respectively.

Many sources of noise in electronic systems exist and have been thoroughly investigated, including thermal, shot, flicker, generation-recombination, avalanche, partition, random telegraph, and burst noise. Of these, RTS and burst noise possess a $1/f^2$ dependence corresponding to red noise which is important for our $Sr_3Ir_2O_7$ measurements.

Figure 4.1 shows depictions of the time and frequency domain signatures of RTS and burst noise. RTS noise is so called due to its resemblance to telegraph signals, which encode information using two discrete states as in Morse code. Systems that display RTS noise vacillate between two states, but unlike information-bearing telegraph signals they switch between the two states at random time intervals. It has been shown with standard signal processing statistical methods that the frequency dependence of such a signal

displays a Lorentzian behavior, leading to $1/f^2$ dependence at high frequencies and a cutoff frequency at f_{RTS}. As the number of accessible states is increased from two as in RTS noise to an infinite number of accessible states, the result successively and more accurately exhibits burst noise, which also shows a $1/f^2$ dependence.

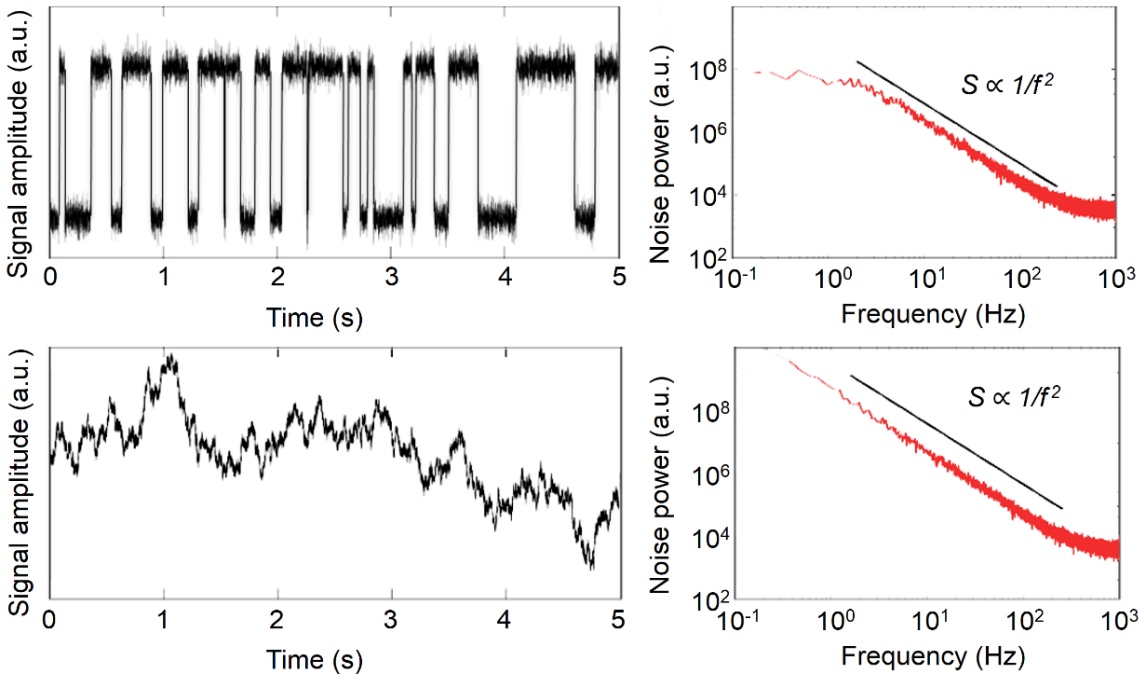

Figure 4.1: Time and frequency domain examples of $1/f^2$ dependent noise. RTS noise (top) is a particular type of burst noise (bottom) that possesses only two permitted states. Figure adapted from ref. 4.

In this chapter we study the resistive switching between the low-resistance state at low electric biases and high-resistance state at high biases in $Sr_3Ir_2O_7$ single crystals. As mentioned previously, the switching occurs above a threshold bias current (I_C) but was also found to initiate an increased noise pattern in the high-bias switching state which might be indicative of high-frequency dynamics of the switching. We employed a spectrum analyzer to delve deeper into the noise pattern and investigated the dependence of the noise spectrum

on the magnitude of the applied bias and magnetic field. While it was found to be magnetic-field independent, we find a clear correlation between the noise amplitude and hysteretic switching behavior as a function of the applied bias. Based on the observed $1/f^2$ frequency dependence of the noise power density we argue that it can be associated with a random switching between different resistance states at high biases.

4.2 Experimental Setup

As mentioned previously, single crystals of $Sr_3Ir_2O_7$ were synthesized for this work using a self-flux technique.[5] The technique results in single crystalline flakes of $Sr_3Ir_2O_7$ with thicknesses of about 0.2-mm and the [001] c-axis oriented perpendicular to the flake's surface (area ~0.5×0.5 mm^2). Single crystal X-ray diffraction was employed to determine the crystal structure of the flakes. As shown in Figure 4.2, Ag paste contacts (area ~0.2×0.2 mm^2) on top and bottom surfaces of $Sr_3Ir_2O_7$ flakes were used to supply and sink dc electrical currents (up to 15 mA). The contacts were made by first preparing ~12 cm lengths of 39 AWG copper wire in which the final 3mm of insulation was stripped. The sample was then mounted to the inner conductor of the coaxial cable connecting the sample to the circuit on a small bed of Ag paste. A small drop of Ag paste was applied to the top of the sample and was allowed to dry with the prepared copper wire embedded in the Ag paste.

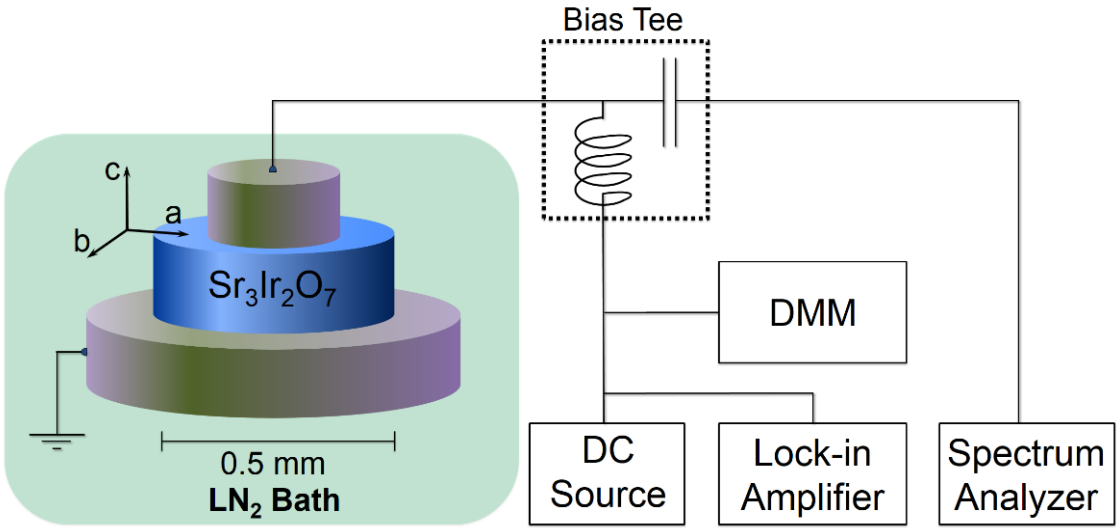

Figure 4.2: Experimental setup consists of the $Sr_3Ir_2O_7$ sample in liquid nitrogen with Ag paste electrical contacts connecting a current source and digital multimeter (DMM). The lock-in amplifier (no reference signal) is sensitive to low frequency (570 Hz) ac signals. A spectrum analyzer records the noise power spectral density (PSD).

In such a 2-probe geometry the applied currents flow (primarily) along the [001] c-axis of the crystal and were shown previously[6,7] to trigger a resistive switching at sufficiently high electrical bias. A wideband bias tee separates the ac and dc sides of the circuit. A dc current source (Keithley 2400) was used to bias the sample in order to initiate resistive switching while a digital multimeter (Keithley 2000) measures the voltage across the sample. Attached to the dc side of the circuit, a lock-in amplifier (Stanford Research SR830) is used to probe the resulting dc and low ac voltage signals across the sample while a spectrum analyzer (Tektronix RSA306) was employed to probe the signal's spectrum on the ac side.

The sample is mounted on a sample holder and placed in a Janis STVP cryostat chamber. Liquid nitrogen was then pumped into the chamber until full. The cryostat is open to the atmosphere where nitrogen boil off permits the sample to be immersed for ~1.5 days.

A custom National Instruments LabView program coordinates the various instruments to supply current and measure associated voltages and signals. Spectral data is captured using the Tektronix software SignalVu-PC, then saved in a spreadsheet format which is imported for analysis and graphing to OriginLab.

4.3 Results

Figure 4.3 shows a representative current-voltage (*I*-*V*) characteristic of $Sr_3Ir_2O_7$ measured at 77 K – the crystal resistance $R=V/I$ is shown as a function of the bias current *I*. Here the blue and red curves show the *R(I)* for increasing and decreasing absolute value of the bias current *I*, respectively.

For an increasing absolute bias we observe a continuous decrease of the crystal resistance and a locally irreversible switching event to a higher resistance at a critical bias $I_C \approx \pm 12.4$ mA. For a decreasing absolute bias, a small decrease in resistance state at $\approx \pm 8$ mA reveals the process of switching back to a lower resistance state.

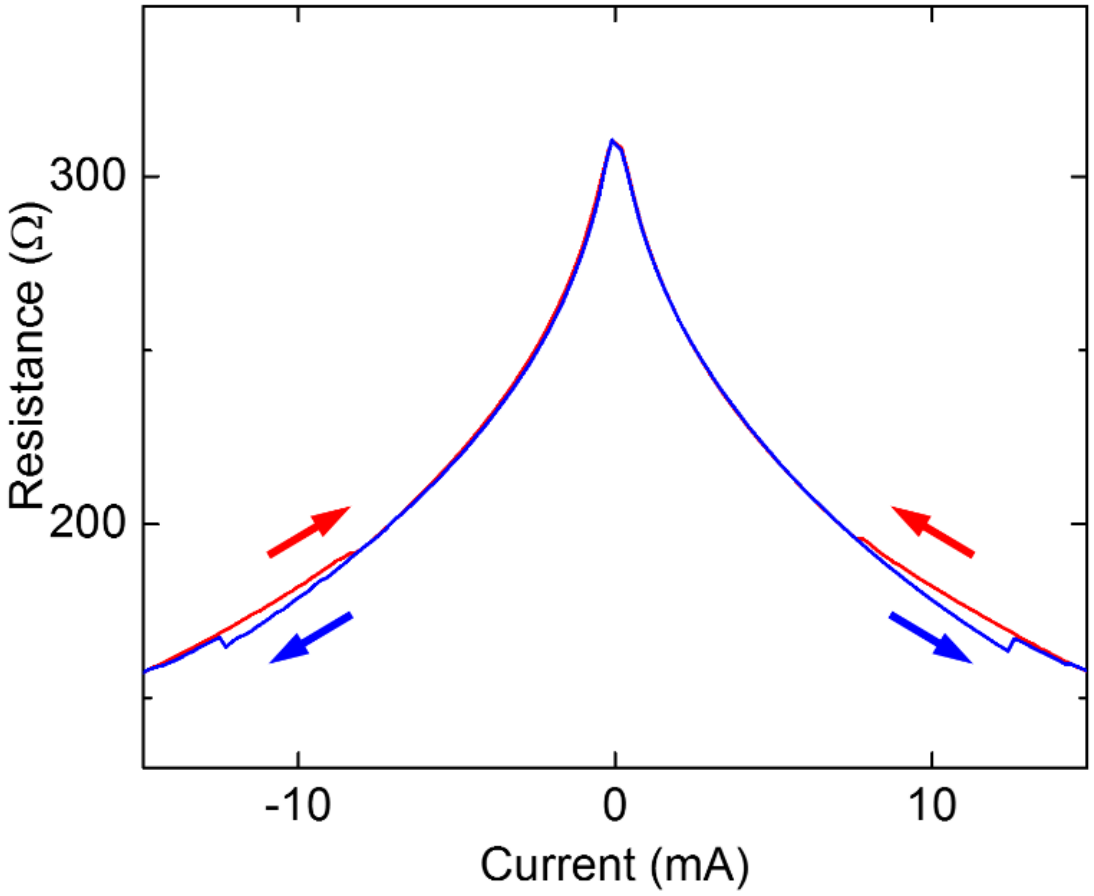

Figure 4.3: Resistive switching in *R(I)* characteristic of $Sr_3Ir_2O_7$ (T = 77 K). Blue and red traces represent the increasing and decreasing absolute current bias, *I*, respectively. After a gradual decrease in *R* with increasing |*I*| the switching to a higher resistance (blue curve) at $I_C \approx \pm 12.4$ mA is clearly visible. For a decreasing |*I*| (red curve), the resistance goes back to a lower resistance state at ≈ ±8 mA.

A closer look at the resistive switching shown in Figure 4.4 reveals that the switching behavior is qualitatively identical with respect to bias polarity, clearly exhibiting hysteretic behavior. At negative (positive) bias an increase in resistance of 2.8 (3.6) Ω occurs at -12.5 (12.6) mA. Switching back to the low resistance state for negative (positive) bias occurs at -8.2 (7.6) mA. Also, a comparatively small, but observable switching to a second higher resistance state occurs for negative (positive) bias at -14.6 (14.4) mA.

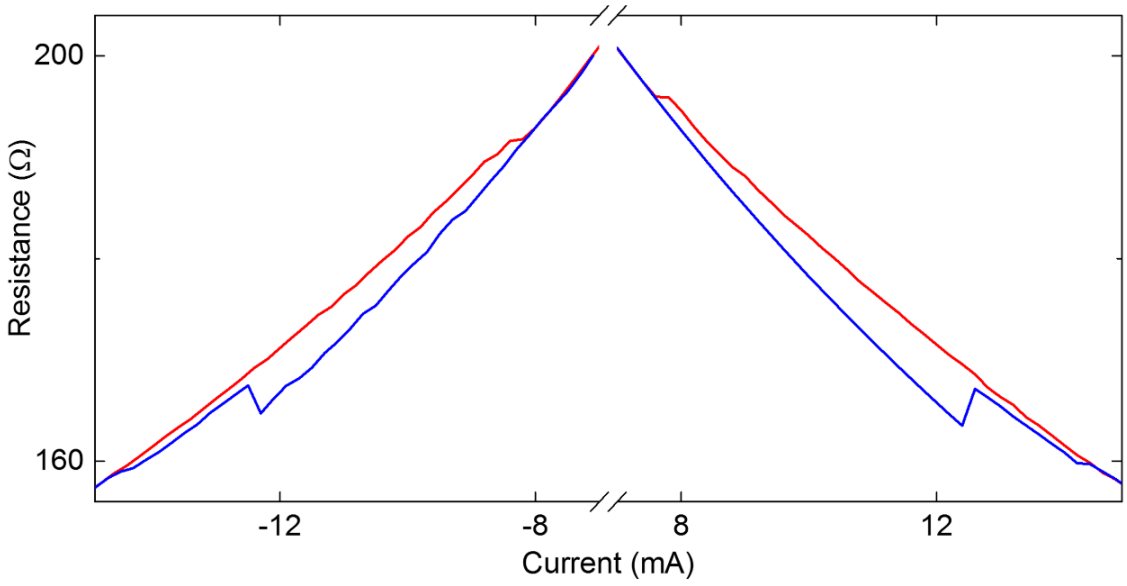

Figure 4.4: Zoomed in portion of *R*(*I*) shows the hysteretic switching behavior more closely at negative and positive bias, respectively. At negative (positive) bias the resistance abruptly increases 2.8 (3.6) Ω, and shows a hysteretic opening spanning ≈ 4 mA. At both negative and positive bias the system switches back into the same low resistance state.

Similar switching characteristics were previously observed in both Sr_2IrO_4[6] and $Sr_3Ir_2O_7$[7] where the continuous/irreversible changes in resistance were associated with electric-field driven lattice distortions/structural transition. The energy barrier associated with the locally irreversible change in resistance (switching) was recently measured in $Sr_3Ir_2O_7$.[8]

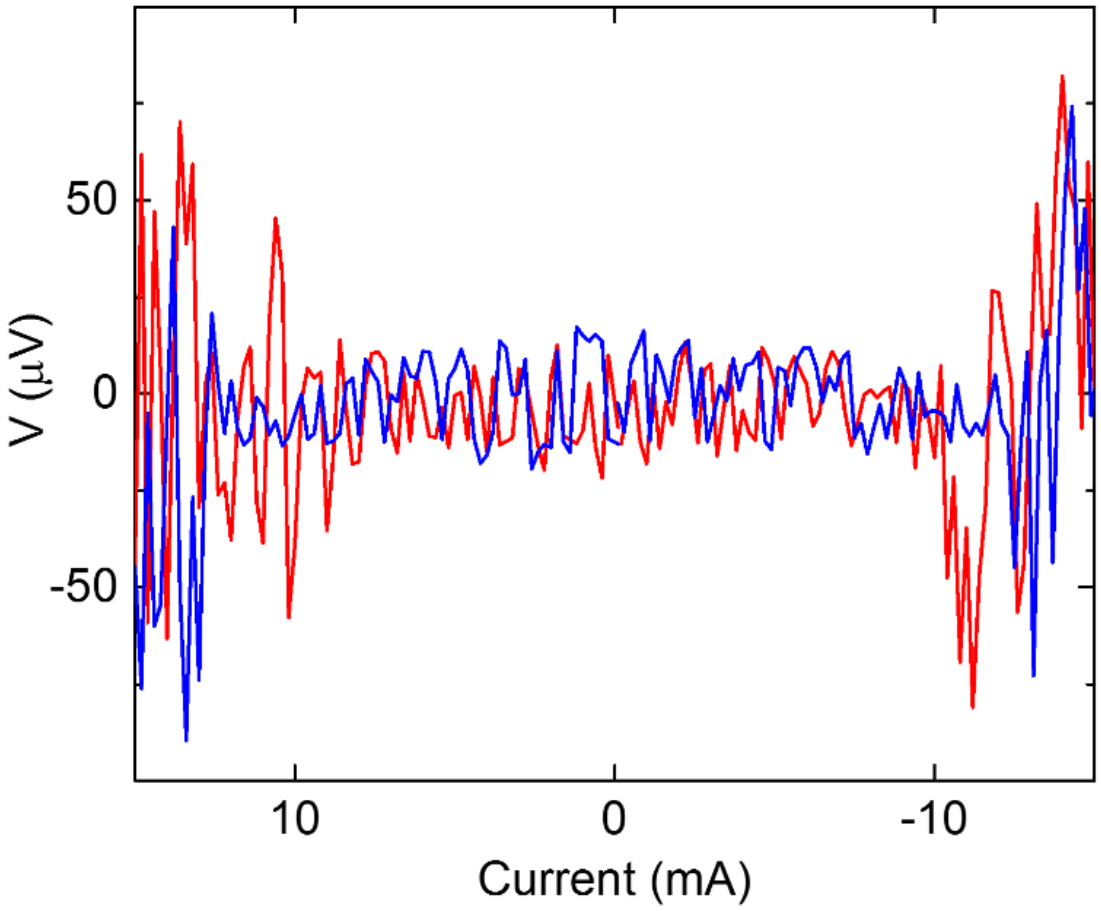

Figure 4.5: Rectified voltage across the sample measured using a lock-in amplifier. The increased noise in the lock-in signal correlates with the hysteretic switching behavior in *R* (blue and red curves use the same convention).

Figure 4.5 shows the rectified voltage across the sample measured using a lock-in amplifier (locked to a frequency of 570 Hz) depicted in blue and red corresponding to increasing and decreasing $|I|$. At applied biases exceeding the critical bias we observe an abrupt increase in the lock-in noise. Moreover, the presence of increased noise correlates with the resistance hysteresis in the *R(I)* measurement. As we increase the bias (denoted by the blue curve) there is an abrupt increase in the noise at $\approx \pm 12.4$ mA. As we decrease

the absolute bias (denoted by the red curve) the additional noise abates at the current value where the resistance switches back into the low resistance state (≈ ±8 mA).

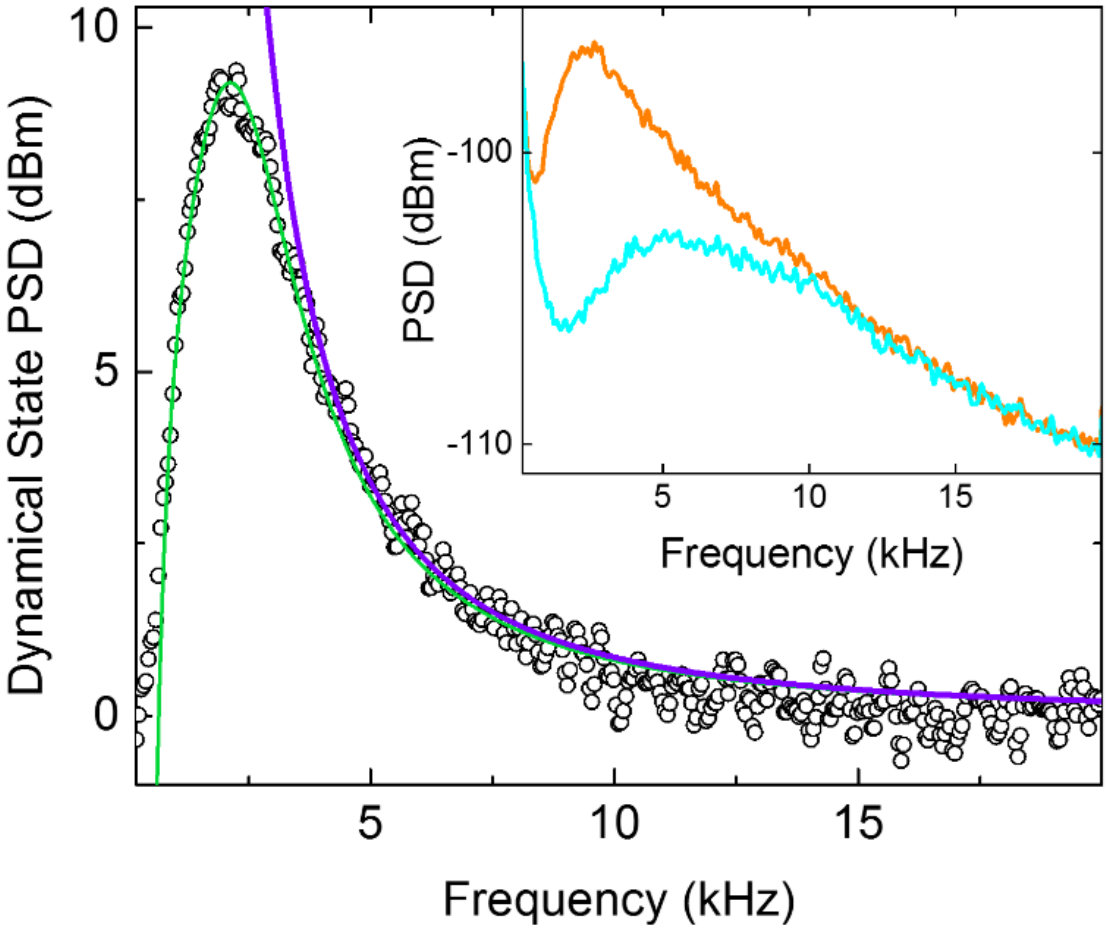

Figure 4.6: PSD of the noise in the high-bias (dynamical) resistance state. The inset shows the PSDs measured by the spectrum analyzer (row data) in the low-resistance state (I=12 mA; cyan curve) and the high-resistance state (I=14 mA; orange curve). Open symbols in the main panel is the difference between the orange and cyan curves. The violet curve represents a $1/f^2$ fit. The green curve represents the same $1/f^2$ fit with a high-pass filter applied, which is associated with a low-frequency cutoff of the spectrum analyzer. The orange curve in the inset represents a background noise pattern of the spectrum analyzer which was measured to be the same without bias or in the presence of a small applied bias ($I < I_C$).

The power spectrum of the noise emerging above I_C was characterized using a Tektronix RSA306 spectrum analyzer. We have measured the power spectrum at different bias currents starting from 0 mA up to 14 mA (in steps of 2 mA) at which point the sample switched to the high resistance state. The measured PSD remained effectively unchanged in the bias range from 0 mA to 12 mA where the sample remains in the low resistance state. An example of such a low-bias ($I < I_C$) behavior is shown in the inset to Figure 4.6 (cyan curve recorded at I =12 mA) which represents a background noise pattern of the spectrum analyzer; for verification purposes, the same functional dependence was observed when the spectrum analyzer was isolated from the sample and its input was shorted with a 50 Ω termination.

Recording the PSD at room temperature with a 50 Ω termination allows us to further validate that the noise spectrum associated with the low-bias resistance state can be treated as a subtractable background. The Figure 4.7 inset displays the largely frequency invariant amplitude of the difference (in blue) between the noise spectra of the sample at low bias, 77 K, and the 50 Ω termination at room temperature. The flat frequency response to the difference of the PSDs suggests that thermal noise, which is frequency invariant (white) noise, is the most significant contributor as expected from a 216 K difference in temperature. The similarity in the functional dependence of the noise spectral data gives credence to the idea that the unique shape of the PSD at low biases is not driven by the sample, but by the circuit. In this way, we can be more confident that we are able to designate the low bias PSDs as subtractable backgrounds.

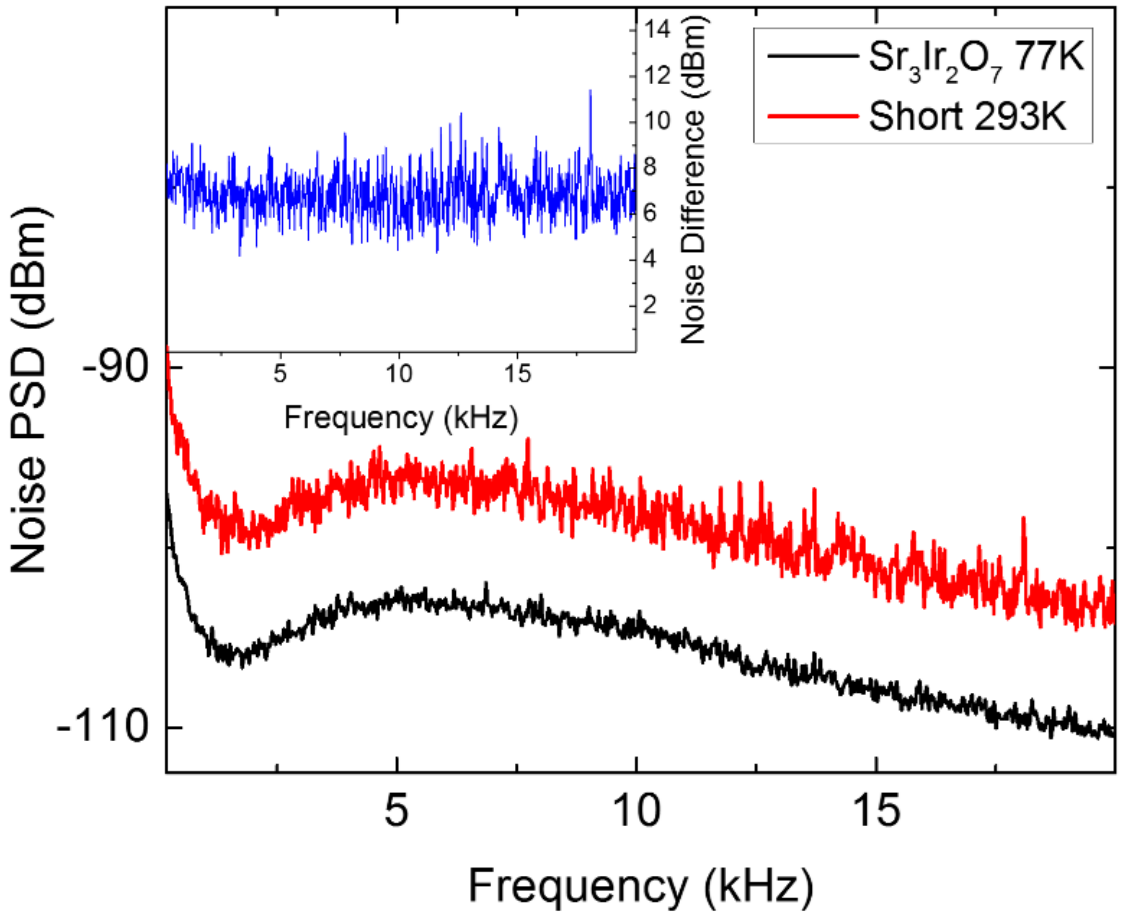

Figure 4.7: PSD of the noise in the low-bias resistance state for increasing bias at 77 K in black. A calibration PSD measured with a 50 Ω short at room temperature is shown in red. The inset shows the difference in noise between the two PSDs in blue. The flat profile of the noise difference (white noise) suggests thermal (Johnson) noise as responsible for the difference of the PSDs. The consistency of the functional dependence of the noise across devices and temperature supports the designation of the low bias PSD as a subtractable background.

When the applied bias was increased above I_C the sample resistance switched into the high resistance state and the noise pattern had changed (see Figure 4.6 inset orange curve recorded at I =14 mA). The resulting PSD of the noise in the high resistance state is shown in Figure 4.6 (open symbols) as obtained by subtracting the PSD measured at 12 mA from the PSD at 14 mA. The PSD at frequencies around 2 kHz is almost a factor of 10

larger in the high resistance state (at 14 mA) compared to that in the low resistance state (at 12 mA). With increasing frequency the PSD increases rapidly at low frequencies, peaks around 2 kHz, and then decreases with a long tail toward higher frequencies. The high-frequency tail can be successfully fitted by a $1/f^2$ dependence (see violet curve in Figure 4.6). The green curve represents the same $1/f^2$ fit but also includes a low-frequency cutoff associated with the finite bandwidth of the spectrum analyzer.

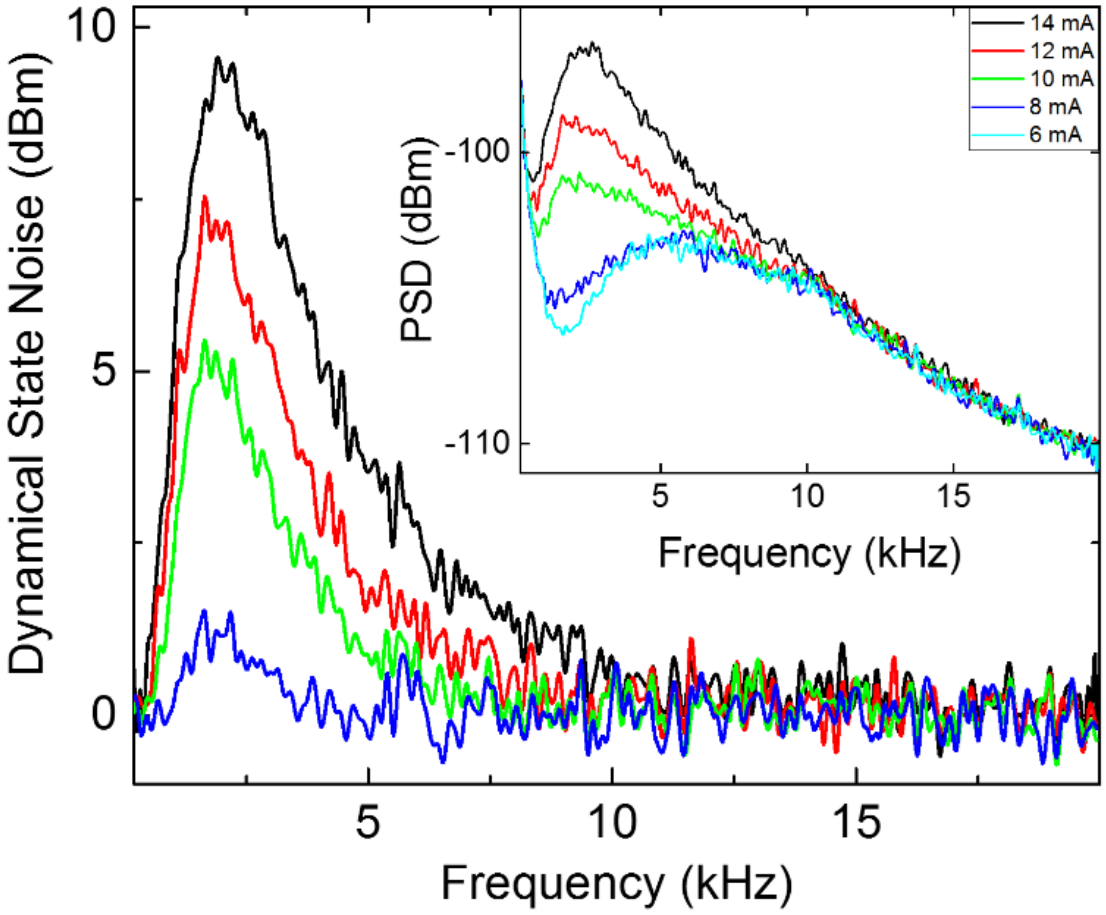

Figure 4.8: PSD of the noise in the high-bias (dynamical) resistance state for decreasing bias. Black, red, green and blue curves show PSDs for 14, 12, 10, 8 mA, respectively. The inset shows the raw-data PSDs; cyan curve (recorded at 6 mA) represents the background noise pattern of the low-resistance state.

When the applied bias was decreased from 14 mA down to 8 mA, the peak value of the noise PSD in the high resistance state had decreased gradually from about 9 dBm to about 1 dBm; see Figure 4.8 where black, red, green and blue curves show PSDs at I = 14, 12, 10, and 8 mA, respectively. When the sample resistance switched back to the low resistance state, the PSD (cyan curve in Figure 4.8 inset recorded at I = 6 mA) had changed back to the background noise pattern observed before for $I < I_C$. No changes in the PSD were observed at any bias when an external magnetic field up to 0.25 T was applied in the basal plane or in the perpendicular direction.

4.4 Discussion

From the above measurements we conclude that (i) the onset of the high-resistance state is accompanied by an emergence of $1/f^2$ noise, and (ii) the noise amplitude in the high-resistance state increases with increasing bias. This noise is indicative of a dynamical high-resistance state and can be tentatively associated with a random switching between different resistance states at high biases as we show next.

The bias-induced variations in resistance of iridates were previously attributed to bias-driven lattice distortions[6, 7] where an applied electric field results in displacements of oxygen ions. In this picture the resistive switching could be associated with a thermally assisted transition (ion migration) over an energy barrier. Such an energy barrier was recently measured in $Sr_3Ir_2O_7$.[8] It is natural to assume that after a bias-driven transition into the high resistance state the system has a finite probability to switch back into the low resistance state or yet into another configuration. Fast excursions into different resistance states are expected to generate an additional noise – random telegraph signal (RTS) noise.[9] The $1/f^2$ PSD observed in our experiments (Figure 4.6) is consistent with RTS noise and

establishes an upper bound for the RTS frequency, f_{RTS}, of 2 kHz. The increase of the noise amplitude with increasing bias can be tentatively attributed to a bias-dependent RTS dwelling time. The observed $1/f^2$ noise is also known as red noise; it is often associated with effects of electromigration,[10–12] i.e. consistent with the field-driven migration of oxygen ions in our $Sr_3Ir_2O_7$ samples.

We should note that the lattice and magnetic degrees of freedom are strongly coupled in AFM iridates like Sr_2IrO_4[6] and $Sr_3Ir_2O_7$[7, 8]. Therefore it is natural to expect that any lattice distortions produced by an applied electric field should result in changes to its magnetic order parameter, i.e. magnetic switching. This opens up interesting opportunities for studying the magnetic switching in AFMs. Such a switching is expected to be much faster than in FM materials thanks to high natural frequencies in AFMs. With an appropriate probe of the magnetic order parameter our present experimental setting provides a useful test bed for studying the magnetic properties of AFM materials, such as the exchange constant, anisotropy, etc., under fast switching conditions between different states.

4.5 Conclusions

In summary, we have investigated the resistive switching between low and high resistance states in antiferromagnetic $Sr_3Ir_2O_7$ single crystals. In particular we characterized the noise associated with the onset of the high resistance state. We observed a clear correlation between the noise amplitude and hysteretic (as a function of applied bias) resistive switching. We tentatively attribute the noise to a random switching between different states at high biases. The observed $1/f^2$ PSD of the noise is consistent with random telegraph signal (RTS) and red noises.

4.6 References

[1] G. Vasilescu, *Electronic Noise and Interfering Signals Principles and Applications* (Springer, Germany, 2005).

[2] A. V. Ziel, *Noise: Sources, characterization, measurement* (Prentice-Hall, New Jersey, 1971).

[3] B. Schiek, I. Rolfes, H.-J. Siweris, *Noise in High-Frequency Circuits and Oscillators* (Wiley, New Jersey, 2006).

[4] B. W. Youngblood, *Two-level noise and stochastic resonance in individual permalloy nanoscale magnets*, PhD dissertation, University of Minnesota, 2015.

[5] G. Cao, Y. Xin, C. S. Alexander, J. E. Crow, P. Schlottmann, M. K. Crawford, R. L. Harlow, and W. Marshall, *Phys. Rev. B* **66**, 214412 (2002).

[6] C. Wang, H. Seinige, G. Cao, J.-S. Zhou, J. B. Goodenough, and M. Tsoi, *Phys. Rev. B* **92**, 115136 (2015).

[7] H. Seinige, M. Williamson, S. Shen, C. Wang, G. Cao, J.-S. Zhou, J. B. Goodenough, and M. Tsoi, *Phys. Rev.* **94**, 214434 (2016).

[8] M. Williamson, S. Shen, G. Cao, J.-S. Zhou, J. B. Goodenough, and M. Tsoi, *Phys. Rev. B* **97**, 134431 (2018).

[9] M. J. Kirton and M. J. Uren, *Advances in Physics* **38**, 367 (1989).

[10] B. M. Wilamowski and J. D. Irwin, *The Industrial Electronics Handbook* (CRC, Boca Raton, 2011) Chap. 11, pp. 11-4–11-6, 1st ed.

[11] D. M. Liou, J. Gong, and C. C. Chen, *Jpn. J. Appl. Phys.* **29**, 7 (1990).

[12] L. K. J. Vandamme, *IEEE Trans. Trans. Electron Devices* **41**, 11 (1994).

C H A P T E R V

MAGNETICALLY PROBED RESISTIVE SWITCHING IN MAGNETITE

5.1 Magnetite

Previous measurements on the transition metal oxide (TMO) $Sr_3Ir_2O_7$ discussed in Chapters 3 and 4 have established an interesting resistive switching phenomenon, which we tentatively attributed to an electrically-driven transition in the material's magnetic order. On one hand the antiferromagnetic order in $Sr_3Ir_2O_7$ is an advantageous property, e.g. for high speed/high density magnetic memory devices. On the other hand, however, the very property that constitutes these advantages also hinders the experimental detection and examination of the magnetic order. Moreover, the strong spin orbit coupling is

generally thought to be responsible for the lattice instigated change in magnetic order, but without a direct magnetic probe this claim has a speculative nature. In what follows, we propose to explore a TMO material, which displays similar resistive-switching characteristics but, at the same time, possesses a non-zero net magnetization. The latter should allow for a direct probing of the TMO's magnetic order, e.g. by the ferromagnetic resonance (FMR) technique, such a material would thus provide an accessible test bed for further insights into interconnections between TMO resistive switching phenomena and changes in their magnetic order. Below we focus our attention on single crystals of Fe_3O_4, otherwise known as magnetite.

In ancient times natural magnetite, also called lodestone (lode meaning "way"), was used in compasses for its magnetic properties. Magnetite is a half-metallic ferrimagnetic material (Figure 5.1) with a cubic inverse spinel structure[1] and a high degree of spin polarization for Fermi level electrons. Its half-metallicity entails that one spin species of electrons is conducting while the other is insulating, generating its highly spin polarized transport properties. Extensively used for microwave devices, magnetite has proven to be a pivotal ferrite for electrical applications but is now being considered for its spintronic fitness touting a robust 858 K Curie temperature.[2–6]

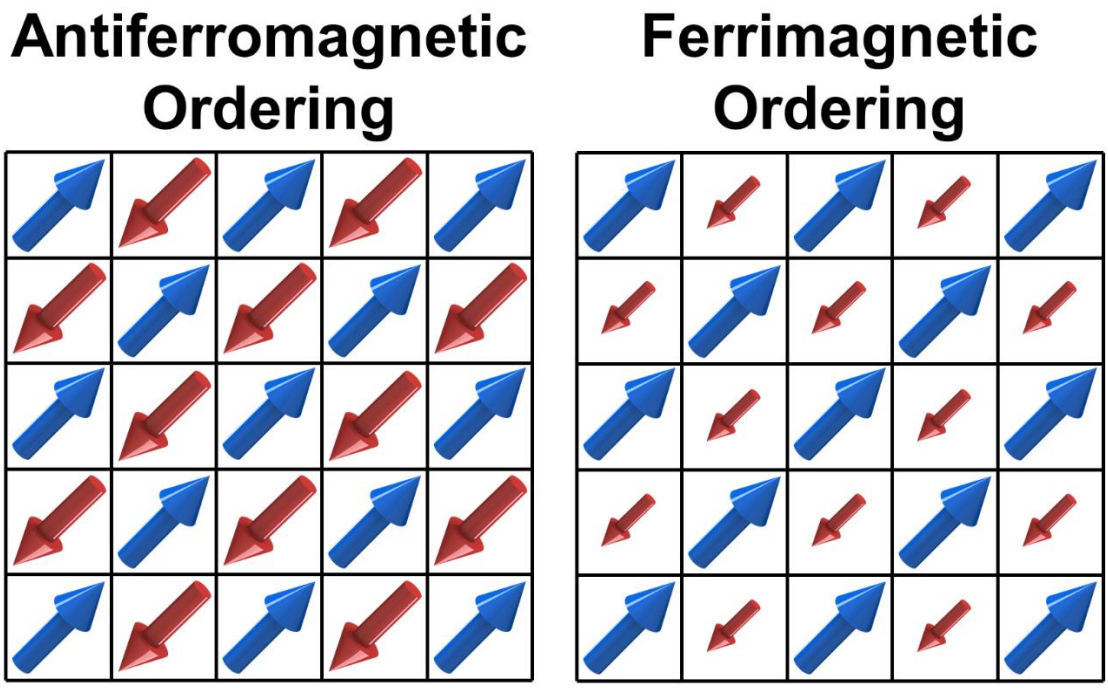

Figure 5.1: Magnetic ordering of antiferromagnetic and ferrimagnetic materials. Ferrimagnetic materials have opposing moments of unequal magnetic strengths, therefore possessing a nonzero net magnetization, which can be probed by ferromagnetic resonance.

5.2 Experimental Setup

A single crystal of magnetite was grown using an image furnace at the University of Texas at Austin. Counter-rotating feed and seed rods of Fe_3O_4 were sintered in an oxygen rich atmosphere.[7] Nearly ideal chemical stoichiometry was confirmed by both X-ray diffraction and a sharp Verway transition at 122 K.[8] The sample, grown along the [100] direction, is a triangular plate roughly 1 mm thick with area (~5×3 mm^2) mounted using Ag epoxy between the inner and outer conductors of a coaxial cable. In this way, the currents flow primarily in the (100) plane constituting a 2-probe measurement as shown in Figure 5.2. The magnetite sample lies in an applied magnetic field that can be rotated (360°)

also in the (100) plane with strengths up to 650 mT. The measurement apparatus for capturing FMR behavior has been disclosed in Chapters 3 and 4 of this work.

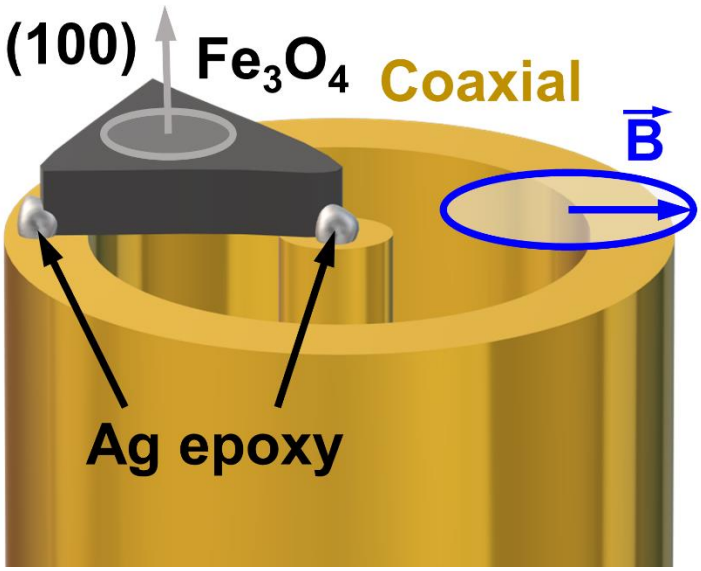

Figure 5.2: Diagram of the sample mounted on a coaxial cable between the inner and outer conductors with Ag epoxy. Magnetic field strength and direction (blue) is azimuthally varied in the (100) plane.

5.3 Results

Figure 5.3 shows the frequency dependence of the FMR spectrum for magnetite where the applied magnetic field is constrained to the (100) plane with an arbitrary azimuthal angle. Dark areas corresponding to FMR absorption on the grayscale plot are highlighted by red circles and fitted using Kittel's equation (Eqn. 5.1) shown in blue.[9–12]

$$f = \frac{\gamma}{2\pi}\sqrt{(B + (N_y - N_z)M)(B + (N_x - N_z)M)} \qquad (5.1)$$

where γ is the gyromagnetic ratio ($2\pi \times 28$ GHz/T), B is the applied field, M is the saturation magnetization (578 mT) and K_1 denotes the magnetocrystalline anisotropy energy density (11 kJ/m^3). N_x (0.045), N_y (0.225), and N_z (0.73) are shape anisotropy factors that not only reflect the triangular shape of the sample, but also integrate the separate components of magnetocrystalline anisotropy. Since the azimuthal angle of our sample is arbitrary (thus taken to be $\phi = 0$), further measurements are conducted later to estimate the angular orientations pertaining to the [010] and [001] directions within the sample plane.

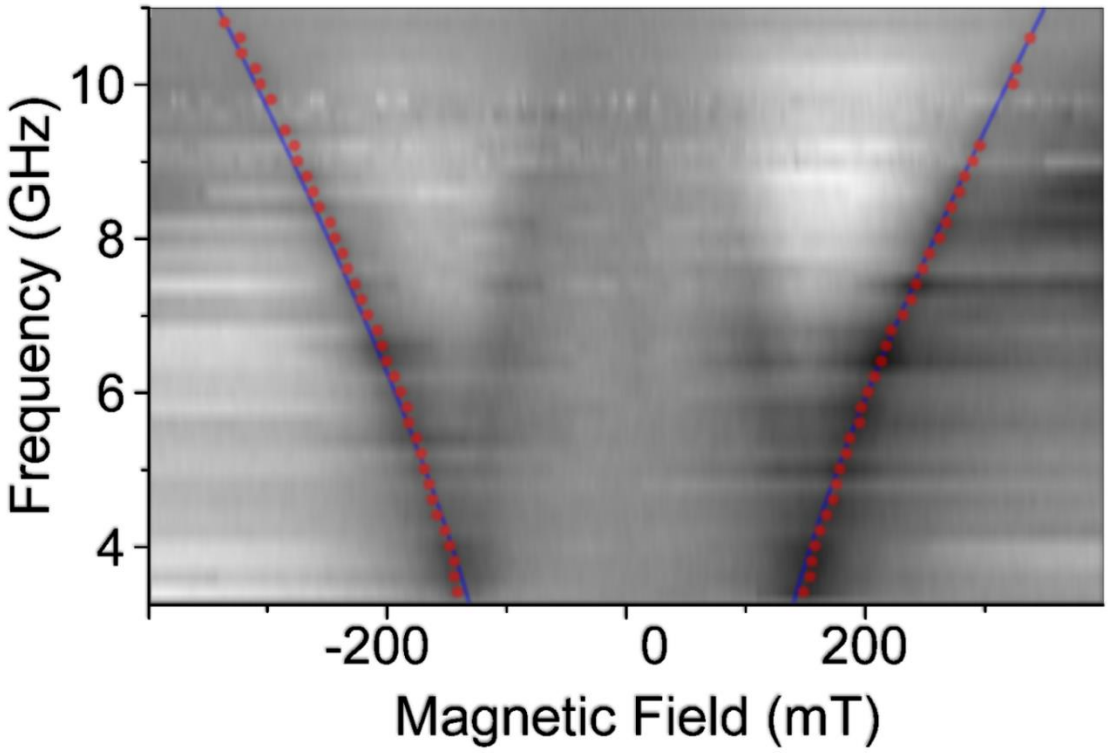

Figure 5.3: Grayscale plot of FMR spectra at different frequencies under low bias of 0.5 mA (~0.5 V). Darker regions represent FMR absorption. Resonance fields were extracted (red circles), and Kittel fit (blue) is shown with the following shape factors: $N_x = 0.045$, $N_y = 0.225$, $N_z = 0.73$.

After we verify ferromagnetic resonance and parameterized anisotropy from Figure 5.3, we home in to a particular frequency and sample orientation that optimizes the signal to noise ratio for the lock-in amplifier. We achieve this by applying an 8 GHz amplitude modulated carrier wave to the sample with an applied magnetic field oriented at a ϕ = -85°. Figure 5.4 shows the result: the background subtracted FMR spectrum as a function of the magnetic field upsweep. We clearly observe two symmetric peaks ~45 mV in amplitude at ~±100 mT that are a rather wide ~100 mT in resonance linewidth, characteristic of Fe_3O_4 due to its exchange conductivity and intrinsic damping.[4–6, 13–15]

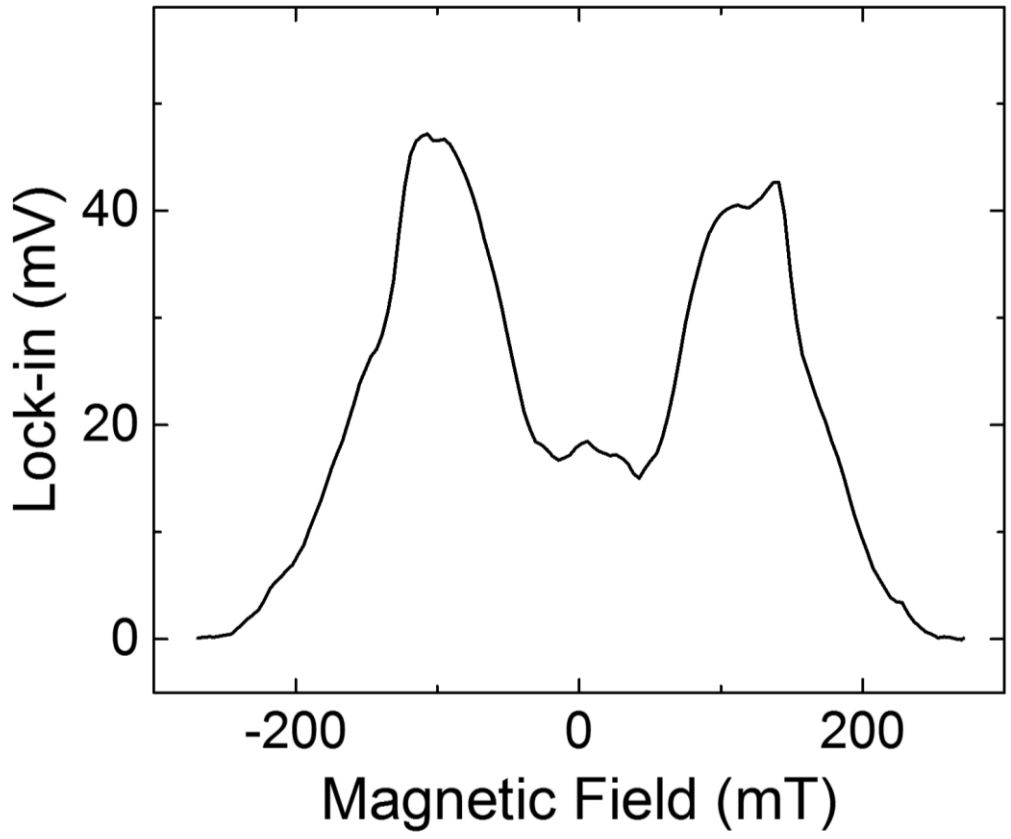

Figure 5.4: Single upsweep trace of the FMR spectrum at an angle of ϕ = -85° at 10.3 mA. Spectrum clearly shows two peaks, each associated with the magnitude of the resonance B field. Large linewidth typical in Fe_3O_4 is observed.

Having tuned the parameters necessary for an adequate FMR signal representing the probe of magnetic order in our system, we turn to bias dependent measurements to establish the signature of resistive switching in our sample. Figure 5.5 shows resistance as a function of applied current starting at 45 mA and decreasing to -45 mA in black, where near zero bias a high resistance of ~70 Ω is demonstrated and at ~-25 mA an anomalous bump in resistance is shown, which corresponds to a resistive-switching event. On the current upsweep (in red) the resistance raises smoothly at ~-25 mA, increases to a resistance lower than previously at zero bias (~50 Ω), then undergoes a similar anomalous bump at ~20 mA until returning to a resistance similar to the start at 45 mA.

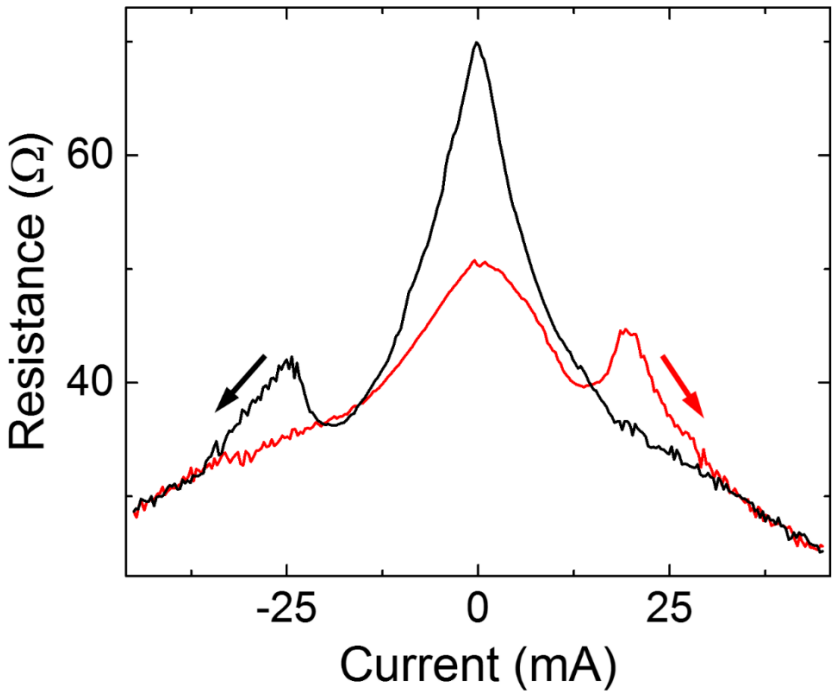

Figure 5.5: Resistance as a function of current establishing resistive switching in Fe_3O_4. Downsweep starts at positive bias and progresses (black) to a high resistance at zero bias then exhibits an anomalous bump in resistance at negative bias. The current then sweeps up (red) to a resistance at zero bias lower than the downsweep resistance. A similar anomalous bump in resistance is observed at positive bias.

Let us designate two states: R_{High} = 70 Ω and R_{Low} = 50 Ω at near zero bias producing a resistance ratio of 40%. The anomalous bumps in resistance constitute the transitions from R_{High} to R_{Low} at negative bias and from R_{Low} to R_{High} at positive bias and represent a bipolar resistive switching.

Simultaneous to our resistance measurements in Figure 5.5, a magnetic field of 105 mT was applied in order to maximize the positive field FMR amplitude as shown in Figure 5.4. The amplitude of the FMR peak (isolated from the raw lock-in signal) was measured as a function of applied bias as shown in Figure 5.6 in order to discern any effects of the resistive switching on the ferromagnetic precession and therefore the magnetic order. Figure 5.6 shows some interesting features that are worth mentioning. First, anomalous bumps can be observed in the FMR lock-in signal and their positions coincide with positions of the bumps in our resistance measurements (Figure 5.5). Second, the sweep associated with R_{Low} (red) generally elicits a larger amplitude than R_{High} at a given bias. Not only does this demonstrate a bipolar hysteresis, but this fact defies the response expected if the amplitude change were merely an increased voltage caused by an increased resistance at constant current. Indeed, the reverse is true, namely, R_{High} (black) generally has a lower associated amplitude. This behavior may be indicative of changes in direction of the Fe_3O_4 magnetization, producing more or less conducive orientations for FMR excitation with respect to the applied magnetic field. At this time, it is unclear if the modulation of FMR amplitude is a straightforward resonance absorption variation or modulation associated with a resonance field shift induced by the resistive switching. In the latter case, such amplitude variation may be caused by sliding up or down the side of the Lorentzian FMR peak in Figure 5.4.

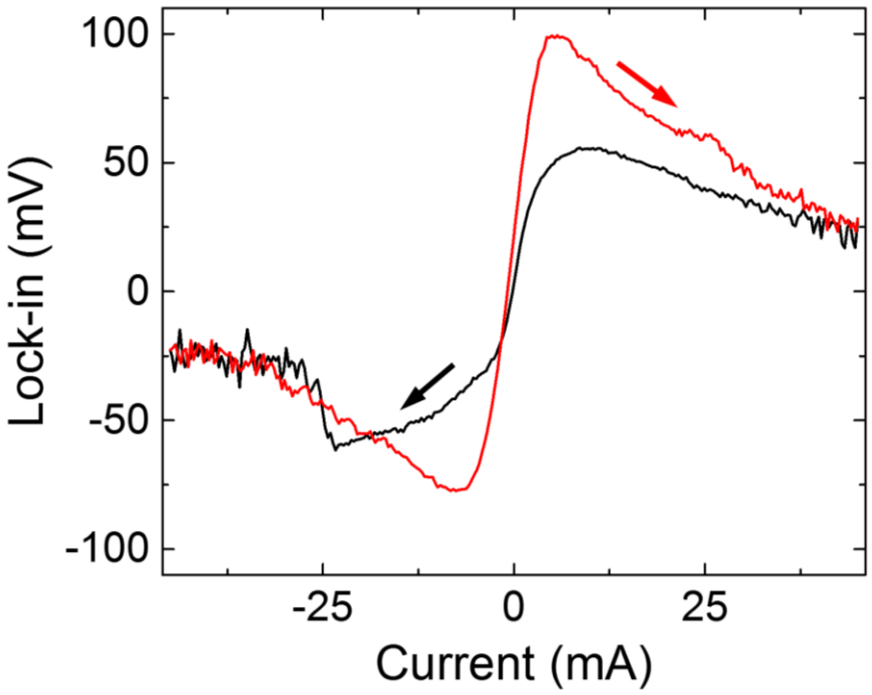

Figure 5.6: Effect of resistive switching on ferromagnetic resonance amplitude in Fe_3O_4. Anomalous bumps in resistance correspond with Figure 5.4. Bipolar type signature is reinforced with characteristics suggesting more than simple electrical effects, rather, magnetic order changes are suggested.

Lastly, we inspect the azimuthal angular dependence of FMR in Fe_3O_4 at 8 GHz in Figure 5.7. The grayscale plot illustrates the FMR spectra measured as a function of azimuthal angle as we sweep magnetic field. We observe a full 360° rotation of rich patterns of resonances. On the left, curves with $1/\cos(\phi)$ dependence are depicted following the contours of individual resonances. On the right, the corresponding resonances can be seen more clearly. As the sample is single crystal Fe_3O_4, the multiple resonance lines are most likely due to magnetic moments associated with different lattice sites in the crystal and not different domains. As there are two groups of resonances, it may be that the blue and magenta resonance are associated with the tetrahedral and octahedral lattice sites and either the [010] or [001] directions. And conversely, this may be the case with the green

and cyan resonances. In any case, ϕ = -30° and ϕ = 60° seem to be the cardinal crystal directions.

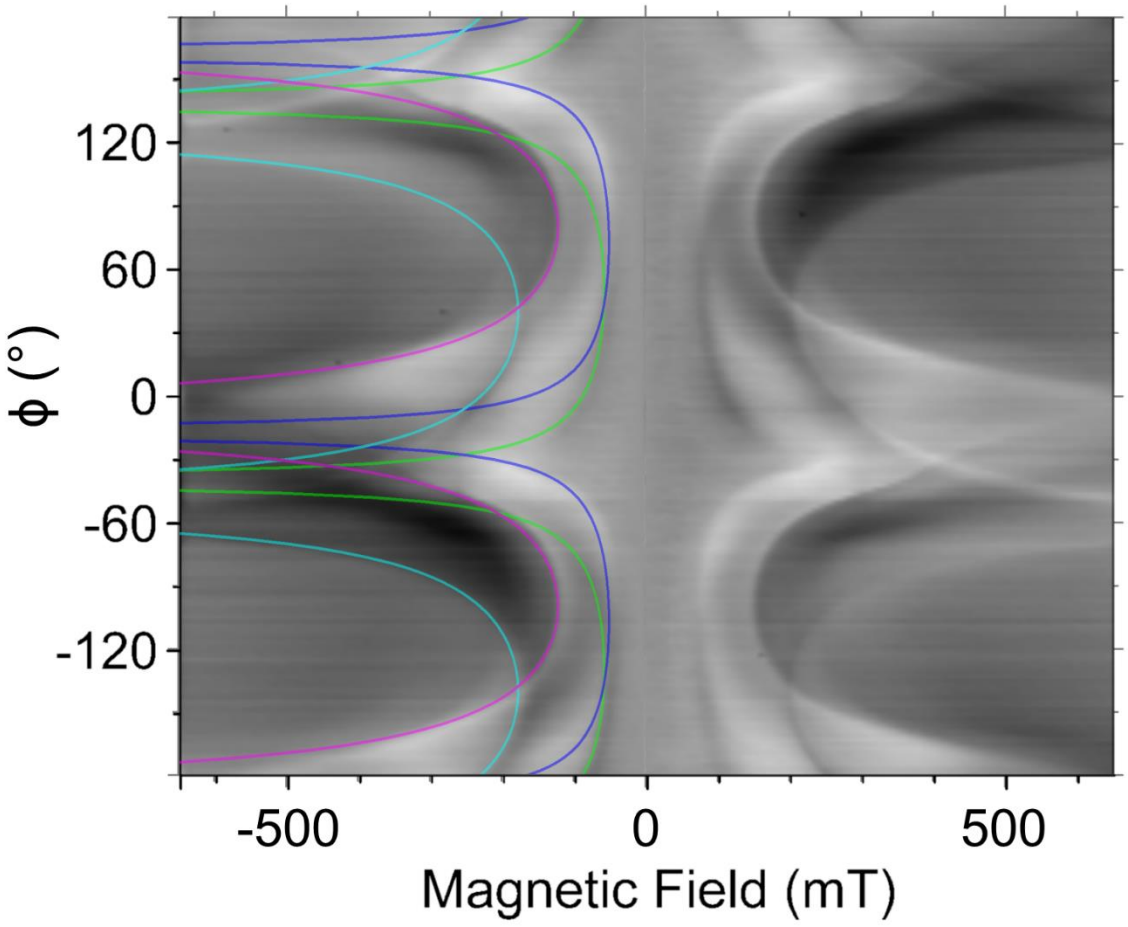

Figure 5.7: Angular dependence of ferromagnetic resonance in Fe_3O_4 at 3 mA (0.8 V). Blue, magenta, green and cyan curves highlight different resonance and have a 1/cos(ϕ) dependence, thus, indicating that the resonance field shows a sizable two-fold anisotropy and is largely dependent on the component of magnetic field pointing in the ϕ = 60° direction.

5.4 Discussion

We have conducted simulations of equilibrium magnetization (Appendix B) and ferromagnetic resonance (Appendix C) in Mathematica in order to elucidate the strong anisotropy with two-fold symmetry observed in our angular dependent FMR measurements. The observed $1/\cos(\phi)$ behavior could be replicated only by introducing a strong magnetic anisotropy. Instead of the singularities in FMR field magnitude at $\phi = -30° \pm 180°$, we arrive at a more or less $\cos(\phi)$ dependence as we integrate the effective shape anisotropies and magnetocrystalline anisotropy into the simulation. This result suggests that the strong anisotropy is functioning at a possibly significant bias of 3 mA that is worth investigating further.

5.5 Conclusions

In summary, we investigated the effects of resistive switching on ferromagnetic resonance (FMR) in Fe_3O_4 single crystals. Most significantly, we found that our experimental method of measuring the resistive switching while probing the magnetic order by using FMR was successful. Furthermore, Fe_3O_4 was instrumental in elucidating the mechanism which modulates the FMR amplitude as a function of applied electrical bias. Also, we found a strong magnetic anisotropy in Fe_3O_4 crystals that dominates the angular-dependent FMR measurements. Overall, Fe_3O_4 has proven to be an essential material for microwave applications but may be especially important in clarifying the spin-lattice interactions[15] among many TMOs connecting crystal lattice transitions and magnetic order for spintronic applications.

5.6 References

[1] Y. Kojima, *Scientific Reports of the Research Institutes of Tohoku University* **A6**, 614 (1954).

[2] V. G. Harris, A. Geiler, Y, Chen, S. D. Yoon, M. Wu, A. Yang, Z. Chen, P. He, P. V. Parimi, X. Zuo, C. E. Patton, M. Abe, O. Acher, C. Vittoria, *J. of Magn. And Magn. Mater.* **321**, 2035 (2009).

[3] G. P. Rodrigue, *Proc. of the IEEE* **76**, 2 (1988)

[4] M. Y. Song, J. G. Lin, M. G. Samant, and S. S. P. Parkin, *IEEE Trans. on Magn.* **50**, 11 (2014).

[5] Z. C. Huang, X. F. Hu, Y. X. Xu, Y. Zhai, Y. B. Xu, J. Wu, and H. R. Zhai, *J. of Appl. Phys.* **111**, 07C108 (2012).

[6] J. R. Fermin, A. Azevedo, F. M. de Aguiar, B. Li, and S. M. Rezende, *J. of Appl. Phys.* **85**, 10 (1999).

[7] J.-F. Lin, J. Wu, J. Zhu, Z. Mao, A. H. Said, B. M. Leu, J. Cheng, Y. Uwatoko, C. Jin, and J. Zhou, *Sci. Rep.* **4**, 6282 (2014).

[8] J. G. Lin, M. Y. Song, J. W. Lin M. G. Samant, and S. S. P. Parkin, *IEEE Trans. on Magn.* **49**, 7 (2013).

[9] L. R. Bickford Jr., *Phys. Rev.* **75**, 1298 (1949).

[10] L. R. Bickford Jr., *Phys. Rev.* **76**, 137 (1949).

[11] L. R. Bickford Jr., *Phys. Rev.* **78**, 4 (1950).

[12] N. Bloembergen, *Proc. of the IRE*, **44**, 10 (1956).

[13] N. Bloembergen and R. W. Damon, *Phys. Rev.* **85**, 699 (1952).

[14] L. G. van Uiter, *Proc. of the IRE*, **44**, 10 (1956).

[15] R. W. Damon, *Rev. Mod. Phys.* **25**, 239 (1953).

C O N C L U S I O N

In this work, we investigated three physical systems relevant to spintronic memory applications. The first was a ferromagnetic device called a magnetic tunnel junction, while the second was a bulk, single crystal antiferromagnetic material, and the third was a single crystal ferrimagnetic material.

In magnetic tunnel junctions we investigated voltage controlled magnetic anisotropy (VCMA) for its ability to assist the present switching mechanism for MRAM: spin-transfer torque. VCMA has the potential to increase the energy efficiency of modern MRAM devices. In perpendicularly magnetized MTJs, we found that devices show a marked saturation of the normally linearly dependent VCMA effect above 2 V, denoting a practical limit of utility. For in-plane magnetized MTJs, we observed a quadratic dependence of VCMA and reinforced the distinctive advantages of FMR for elucidating anisotropy in magnetic systems.

In our measurements of the transport properties of the antiferromagnetic transition metal oxide, $Sr_3Ir_2O_7$, we found not only continuous resistance changes, but also abrupt resistive switching displaying a threshold type behavior. We quantified the energy barrier associated with the switching as a function of applied bias and temperature, attributing the effect to electric field induced lattice distortions influencing the band structure of the material. Furthermore, we observed a dynamical state at biases higher than the critical switching current and measured the attendant noise spectrum as having a $1/f^2$ power spectral density which was associated with random telegraph noise. Due to the strong spin-orbit coupling locking the magnetic order and crystal lattice together in $Sr_3Ir_2O_7$, finite changes in the lattice caused by transport mechanisms such as bias may be an effective means of controlling the magnetic order in antiferromagnetic spintronic devices.

Lastly, we investigated the effect of bipolar resistive switching on magnetic order in Fe_3O_4 using the FMR technique. We found that the FMR method was successful in extracting an evidence of the bias-induced variations in the FMR amplitude. Our experiments demonstrated a clear change in the FMR signal for different resistance states of the sample. Also, we characterized the rich angular dependence of FMR in Fe_3O_4 and corroborated the observed two-fold symmetry of the strong magnetic anisotropy using simulations.

The continuing refinement of spintronic technology to increase its energy efficiency and the exploration of novel ways to control the magnetic order in antiferromagnetic materials will be needed to ensure the viability and manifest the potential of spintronic applications.

APPENDICES

Appendix A

```
%170228 Catch SIO 327 switching analysis of current
%step size dependence on time delay of switching
%Upgrade to importing multiple converted files at once.
repeat = 20;
A = zeros(10000*repeat,2);
%[filename,pathname] = uigetfile('D:\170227 1322 SIO Catch Switch Data/*.dat');
[filename,pathname] = uigetfile('C:\DATA01\170515_170719\170515_1339
combine\*.dat');
A = importdata(strcat(pathname,filename));


time=zeros(10000,1);
amp=zeros(repeat,10000);
origtime=zeros(repeat,10000);
shifttime=zeros(repeat,10000);
cuttingf=zeros(repeat,10000);
cutlist=zeros(repeat,4);
shiftlist=zeros(repeat,1);
k=1;


disp('step 0 complete')
%put data in to useable organization
for i=1:repeat
    %time = E0(1:10000);
    time = A(:,1);
   for j=1:10000
        %amp(i,j) = E3(j+(i-1)*10000);
        %origtime(i,j) = E0(j+(i-1)*10000);
        amp(i,j) = A(j+(i-1)*10000,2);
%         disp('j')
%         disp(j)
%         disp('i-1')
%         disp(i-1)
%         disp('size')
%         size(A)
        origtime(i,j) = A(j+(i-1)*10000,1);
   end
end
disp('step 1 complete')
%find first crossing of 0.015 in order to collapse
%trigger timing
```

```
for i=1:repeat
   ifirst=0; %keeps track of number of times trace is above threshold
   for j=1:10000
        if amp(i,j) >= 0.015 && ifirst ~= 1
            ifirst=1;
            shiftlist(k)=j;
            k=k+1;
        end
   end
end
disp('step 2 complete')
%shift original time
for i=1:repeat
   for j=1:10000
%        disp(i)
%        disp(j)
%        disp(A(1,1))
%        disp(shiftlist(1))
       shifttime(i,j) = origtime(i,j)-origtime(i,shiftlist(i));

   end
end
disp('step 3 complete')

%subtract exponential function in order to get timing of
%switching from the crossover
k=1;
for i=1:repeat
    jcross = 0;
   for j=1:10000
        %cuttingf(i,j) = 0.13*exp(-50*(shifttime(i,j)+0.012))+0.02;
        %cuttingf(i,j) = 20*exp(-5*(shifttime(i,j)+0.04))+0.02;
        cuttingf(i,j) = 0.085*exp(-10*(shifttime(i,j)+0.08))+0.018 + 0.02*exp(-
(shifttime(i,j)+0.0008)^2/(2*0.0020^2));


        %ampcut(i,j) = amp(i,j)-cuttingf(i,j);
        if amp(i,j)>cuttingf(i,j) && jcross ~= 1
            jcross = 1;
            cutlist(k,1) = shifttime(i,j);
            cutlist(k,2) = amp(i,j);
            cutlist(k,3) = i;
            cutlist(k,4) = j;
            k=k+1;
        end
```

```
   end
end
disp('step 4 complete')
%display data and cutting line to ensure that the analysis is
%doing the right thing.

figure;
%plot(shifttime(1:10:end),amp(1:10:end),'.',shifttime(1:10:end),cuttingf(1:10:e
nd),'-')
plot(shifttime(1:1:end),amp(1:1:end),'.',shifttime(1:2:end),cuttingf(1:2:end),'
-')
%axis([-0.5,2,-0.025,0.12])
%axis([-0.5,10,-0.025,0.12])
axis([-0.005,0.02,-0.025,0.12])

figure;
plot(shifttime(1:1:end),amp(1:1:end),'.',shifttime(1:2:end),cuttingf(1:2:end),'
-')
axis([-0.005,2,-0.025,0.12])

disp('step 5 complete')
%create meaningful save file name and save it as .dat file
savename = strcat(pathname, strcat(filename(1:end-4),'Switches.dat'));

save(savename,'cutlist', '-ascii')
disp('step 6 complete')



% mean = mean(cutlist(1:end,1));
% disp('mean = ',mean)
% stderror = std( cutlist(1:end,1) ) / sqrt( length( cutlist(1:end,1) ));
% disp('standard error = ',stderror)
```

Appendix B

```
B1 = .; B2 = .; B3 = .; B = .; θ = .; ϕ = .; Nx = .; Ny = .; Nz = .; M = .; K1 = .; γ = .; θM = .; ϕM = .;
θH = .; ϕH = .;
K2 = .;


B1 = .; B2 = .; B3 = .; B = 0.05 ; θ = .; ϕ = .; Nx = 0.045 ; Ny = 0.225 ; Nz = 0.73 ; M = 4.6 × 10^5 ; K1 = -1.1 10^4; γ
θM = .; ϕM = .;
θH = 90 * π/180 ; ϕH = 0;
K2 = 0 ;

F = -M B (Sin [θM] Cos [ϕM] Sin [θH] Cos [ϕH] + Sin [θM] Sin [ϕM] Sin [θH] Sin [ϕH] + Cos [θM] Cos [θH] ) +
    1/2 4 π 10^-7 M^2 (Nx Cos [ϕM]^2 Sin [θM]^2 + Ny Sin [ϕM]^2 Sin [θM]^2 + Nz Cos [θM]^2) +
    K1 (Cos [ϕM]^2 Sin [ϕM]^2 + Sin [ϕM]^2 Cos [θM]^2 + Cos [ϕM]^2 Cos [θM]^2) + K2 (Cos [ϕM]^4 Sin [ϕM]^4 Cos [θM]^4) ;
F2 = -M B (Sin [θM] Cos [ϕM] Sin [θH] Cos [ϕH] + Sin [θM] Sin [ϕM] Sin [θH] Sin [ϕH] + Cos [θM] Cos [θH] ) ;
F3 = 1/2 4 π 10^-7 M^2 (Nx Cos [ϕM]^2 Sin [θM]^2 + Ny Sin [ϕM]^2 Sin [θM]^2 + Nz Cos [θM]^2) ;
F4 = K1 (Cos [ϕM]^2 Sin [ϕM]^2 + Sin [ϕM]^2 Cos [θM]^2 + Cos [ϕM]^2 Cos [θM]^2) + K2 (Cos [ϕM]^4 Sin [ϕM]^4 Cos [θM]^4) ;

Minimize [F, {ϕM, θM}]
Plot3D [F, {ϕM, 0, 2 π}, {θM, 0, π}, AxesLabel → Automatic , PlotLegends → Automatic ]
Print ["polar "]
θM = 0 * π/180 ;
θH = 0 * π/180 ;

Plot [F, {ϕM, 0, 2 π}]
Print ["in plane "]
θM = 90 * π/180 ;
θH = 90 * π/180 ;
Plot [F, {ϕM, 0, 2 π}]
θM = .;
{-17017.2, {ϕM → -8.4262 × 10^-17, θM → 1.5708}}
```

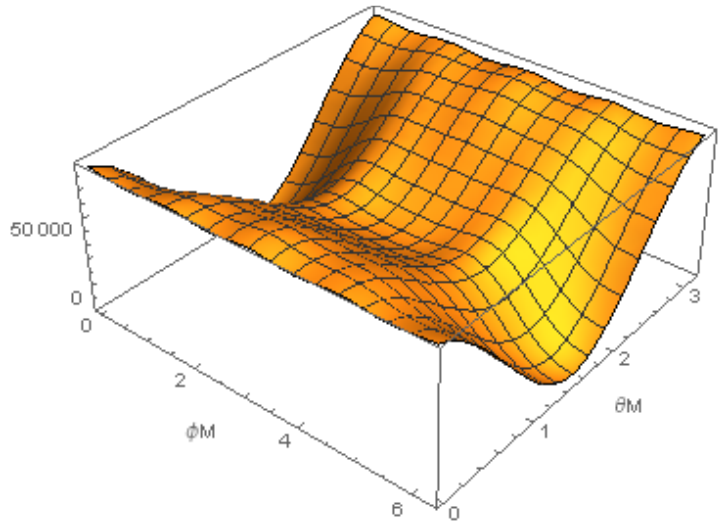

polar

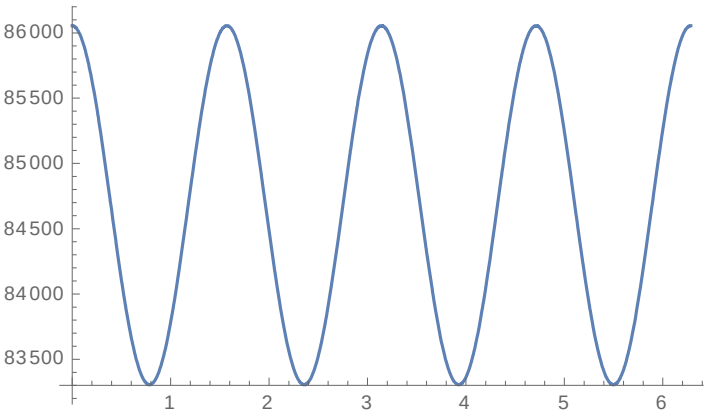

in plane

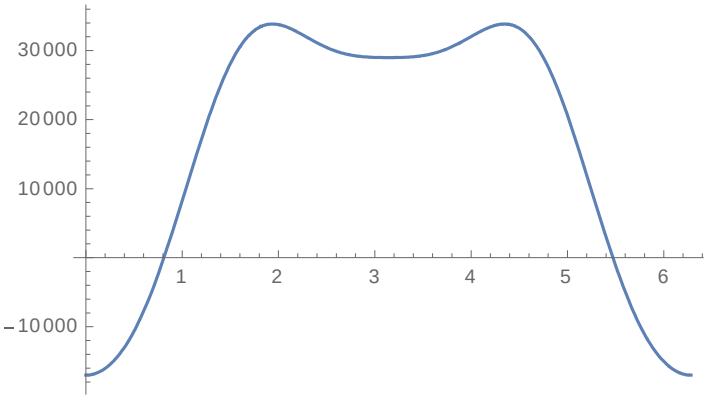

Appendix C

```
(*All Variables are free*)
Manipulate [B=.; Nx=.; Ny=.; Nz=.; M=.; K1=.; γ=.; μ0=.; K2=.;
 θM=.; ϕM=.; θB=.; ϕB=.; ϕsh=.;


 F = -M B (Sin[θM] Cos[ϕM - ϕsh] Sin[θB] Cos[ϕB] + Sin[θM] Sin[ϕM - ϕsh] Sin[θB] Sin[ϕB] + Cos[θM] Cos[θB]) +
   1/2 μ0 M^2 (Nx Cos[ϕM - ϕsh]^2 Sin[θM]^2 + Ny Sin[ϕM - ϕsh]^2 Sin[θM]^2 + Nz Cos[θM]^2) +
   K1 (Cos[ϕM - ϕsh]^2 Sin[θM]^2 Sin[ϕM - ϕsh]^2 Sin[θM]^2 + Sin[ϕM - ϕsh]^2 Sin[θM]^2 Cos[θM]^2 + Cos[ϕM - ϕsh]^2 Sin[θM]^2 Cos[θM]^2) +
   K2 (Cos[ϕM - ϕsh]^2 Sin[θM]^2 Sin[ϕM - ϕsh]^2 Sin[θM]^2 Cos[θM]^2);


 Fθ∂θM = D[F, {θM, 2}];
 Fϕ∂ϕM = D[F, {ϕM, 2}];
 Fϕ∂M = D[F, ϕM];
 Fϕ∂θM = D[Fϕ∂M, θM];

 f2 = γ 1/(1 M Sin[θM]) Sqrt[(Fθ∂θM Fϕ∂ϕM - Fϕ∂θM^2)];

 Nz = Nza; Nx = 1 - Nza; Ny = 0 (*1-Nza-Nxa*); ϕsh = ϕsha;

 K1 = K1a; K2 = K2a; γ = 28; μ0 = 4 π 10^-7; M = Ma;

 (*min = Minimize [F,{θM,ϕM}];
 Print ["min"];
 Print [min];*)

 θM = θMa; ϕM = .; θB = θMa; ϕB = ϕM;

 (*Print [f2];*)
 f1 = γ Sqrt[B (B + μ0 M)];
 f2 = γ 1/(1 M Sin[θM]) Sqrt[(Fθ∂θM Fϕ∂ϕM - Fϕ∂θM^2)];
 num = Solve[f == γ 1/(1 M Sin[θM]) Sqrt[(Fθ∂θM Fϕ∂ϕM - Fϕ∂θM^2)], B];

 Plot[{num[[1, 1, 2]], num[[2, 1, 2]]}, {ϕM, 0, 2 π}, PlotRange → {-1, 1},
  Prolog → Inset[ReliefPlot [Transpose [b], ColorFunction → GrayLevel, ImageSize → Large, AspectRatio → 1/1.6], {0, -1}, {0, 0}, 7], AspectRatio → 1/1.6]

 (*Plot[{f1,f2},{B,-1,1}, PlotRange → {0,12}]*),

 Grid[{
   {"Nz", Nza}, {"Nx", Nxa}, {"Ny", Ny}, {" ", " "}}], {{Ma, 4.6 × 10^5}, 0.1, 10^6}, {{K1a, -1.1 10^4}, -10^5, 10^5}, {{K2a, 0}, -10^5, 10^5}, {{θMa, π/2}, 0.01, π},
 {{f, 8}, 1, 12}, {{Nza, 0.364}, 0, 1}(*,{{Nxa,0.16},0,1}*), {{ϕsha, 0.194}, -π/2, π/2}]
```

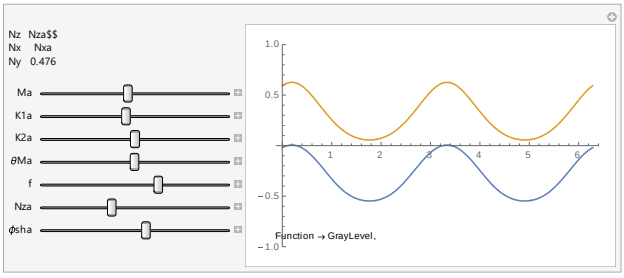

REFERENCES

Introduction

[1] M. N. Baibich, J. M. Broto, A. Fert, F. Nguyen Van Dau, F. Petroff, P. Etienne, G. Creuzet, A. Friederich, and J. Chazelas, *Phys. Rev. Lett.* **61**, 2472 (1988).

[2] M. Flatte, *IEEE Transactions on Electron Devices* **54**, 5 (2007).

[3] V. Baltz, A. Manchon, M. Tsoi, T. Moriyama, T. Ono, and Y. Tserkovnyak, *Rev. Mod. Phys.* **90**, 015005 (2018).

[4] A. H. MacDonald and M. Tsoi, *Phil. Trans. R. Soc. A* **369**, 3098-3114 (2011).

[5] C. Chappert, A. Fert, F. N. Van Dau, *Nat. Mater.* **6**, 813–823 (2007).

[6] J. C. Slonczewski, *J. Magn. Magn. Mater.* **159**, (1996).

[7] M. Tsoi, A. G. M. Jansen, J. Bass, W.-C. Chiang, M. Seck, V. Tsoi, and P. Wyder, *Phys. Rev. Lett.* **80**, 42 (1998).

[8] M. Tsoi, A. G. M. Jansen, J. Bass, W.-C. Chiang, M. Seck, V. Tsoi, and P. Wyder, *Nature* **406** (1998).

[9] H. Seinige, *Current-driven Non-linear Magnetodynamics in Magnetic Nano-devices.* Austin: U of Texas, 2016.

[10] M. Williamson, *Ferromagnetic Resonance in Magnetic Tunnel Junctions under High DC Biases*. Austin: U of Texas, 2016

[11] C. Kittel, Phys. Rev. **73**, 2 (1948).

[12] A. A. Tulapurkar, Y. Suzuki, A. Fukushima, H. Kubota, H. Maehara, K. Tsunekawa, D. D. Djayaprawira, N. Watanabe, and S. Yuasa, *Nature* **438,** 339–342 (2005).

[13] F. Matsukura, Y. Tokura, and H. Ohno, Nature Nanotechnology 10 (2015).

[14] T. Nozaki, Y. Shiota, S. Miwa, S. Murakami, F. Bonell, S. Ishibashi, H. Kubota, K. Yakushiji, T. Saruya, A. Fukushima, S. Yuasa, T. Shinjo and Y. Suzuki, Nature Physics 8 (2012).

[15] T. Maruyama, Y. Shiota, T. Nozaki, K. Ohta, N. Toda, M. Mizuguchi, A. A. Tulapurkar, T. Shinjo, M. Shiraishi, S. Mizukami, Y. Ando, and Y. Suzuki, *Nature Nanotechnology* **4** (2009).

[16] W. G. Wang, C. L. Chien, *J. Phys. D: Appl. Phys.* **46** (2013).

[17] D. Odkhuu, W. S. Yun, S. H. Rhim, S. C. Hong, *J. Magn. Magn. Mater*. **414,** 126 (2016).

[18] H. Lee, A. Lee, S. Wang, F. Ebrahimi, P. Gupta, P. Khalili Amiri, K. L. Wang, *IEEE Transactions on Magnetics* **54**, 4 (2018).

[19] P. Khalili Amiri, J. G. Alzate, X. Q. Cai, F. Ebrahimi, Q. Hu, K. Wong, C. Grèzes, H. Lee, G. Yu, X. Li, M. Akyol, Q. Shao, J. A. Katine, J. Langer, B. Ocker, and K. L. Wang, *IEEE Transactions on Magnetics* **51**, 11 (2015).

[20] K. L. Wang, H. Lee, P. Khalili Amiri, *IEEE Transactions on Nanotechnology* **14**, 6 (2015).

[21] C. Kittel, *Phys. Rev* **82**, 565 (1951).

[22] P. Wadley, B. Howells, J Železný, C. Andrews, V. Hills, R. P. Campion, V. Novák, K. Olejník, F. Maccherozzi, S. S. Dhesi, S. Y. Martin, T. Wagner, J. Wunderlich, F. Freimuth, Y. Mokrousov, J. Kuneš, J. S. Chauhan1, M. J. Grzybowski, A. W. Rushforth, K. W. Edmonds, B. L. Gallagher, T. Jungwirth, *Science* **351**, 6273 (2016).

[23] G. Cao *at al.*, *Phys. Rev. B* **66**, 214412 (2002).

[24] N. F. Mott, *Adv. Phys.* **13**, 325 (1964).

[25] C. Wang, H. Seinige, G. Cao, J.-S. Zhou, J. B. Goodenough, and M. Tsoi, *Phys. Rev. B* **92**, 115136 (2015).

[26] H. Seinige, M. Williamson, S. Shen, C. Wang, G. Cao, J.-S. Zhou, J. B. Goodenough, and M. Tsoi, *Phys. Rev. B* **94**, 214434 (2016).

[27] C. Wang, H. Seinige, G. Cao, J.-S. Zhou, J. B. Goodenough, and M. Tsoi, *Phys. Rev. X* **4**, 041034 (2014).

[28] B. Kim, P. Liu, and C. Franchini, *Phys. Rev. B* **95**, 024406 (2017).

[29] G. Cao, J. Terzic, H.D. Zhao, H. Zheng, L. E. De Long, and P. S. Riseborough, *Phys. Rev. Lett.* **120**, 017201 (2018).

Chapter I

[1] P. A. Cox, Transition Metal Oxides (Oxford University Press, 2010).

[2] B. J. Kim et al., Phys. Rev. Lett. 101, 076402 (2008).

[3] F. Wang, T. Senthil, Phys. Rev. Lett. 106, 136402 (2011).

[4] D. Pesin, L. Balents, Nature Physics 6, 376 (2010).

[5] Y. Okamoto et al., Phys. Rev. Lett. 99, 137207 (2007).

[6] M. Bibes, A. Barthélémy, IEEE Trans. Electron Devices 54, 1003 (2007).

[7] H. Akinaga, H. Shima, Proc. IEEE 98, 2237 (2010).

[8] H.-S. P. Wong et al., Proc. IEEE 100, 1951 (2012).

[9] A. H. MacDonald, M. Tsoi, Phil. Trans. R. Soc. A 369, 3098 (2011).

[10] V. Baltz et al., Rev. Mod. Phys. 90, 015005 (2018).

[11] C. Wang, H. Seinige, G. Cao, J.-S. Zhou, J. B. Goodenough, and M. Tsoi, Phys. Rev. X **4**, 041034 (2014).

[12] C. Wang, H. Seinige, G. Cao, J.-S. Zhou, J. B. Goodenough, and M. Tsoi, Phys. Rev. B **92**, 115136 (2015).

[13] G. Cao, Y. Xin, C. S. Alexander, J. E. Crow, P. Schlottmann, M. K. Crawford, R. L. Harlow, and W. Marshall, Phys. Rev. B **66**, 214412 (2002).

[14] H. Seinige, M. Williamson, S. Shen, C. Wang, G. Cao, J.-S. Zhou, J. B. Goodenough, and M. Tsoi, Phys. Rev. B 94, 214434 (2016).

[15] J. E. Jensen, W. A. Tuttle, R. B. Stewart, H. Brechna, and A. G. Prodell, *Brookhaven National Laboratories Selected Cryogenic Data Notebook* (BNL, New York, 1980)

[16] D. Haskel, G. Fabbris, Mikhail Zhernenkov, P. P. Kong, C. Q. Jin, G. Cao, and M. van Veenendaal, Phys. Rev. Lett. **109**, 027204 (2012)

[17] Y. Ding, L. Yang, C.-C. Chen, H.-S. Kim, M. J. Han, W. Luo, Z. Feng, M. Upton, D. Casa, J. Kim, T. Gog, Z. Zeng, G. Cao, H. Mao, and M. Veenendaal, Phys. Rev. Lett. **116**, 216402 (2016)

[18] D. A. Zocco, J. J. Hamlin, B. D. White, B. J. Kim, J. R. Jeffries, S. T. Weir, Y. K. Vohra, J. W. Allen, and M. B. Maple, J. Phys. Condens. Matter **26**, 255603 (2014).

[19] C. Donnerer, Z. Feng, J. G. Vale, S. N. Andreev, I. V. Solovyev, E. C. Hunter, M. Hanfland, R. S. Perry, H. M. Rønnow, M. I. McMahon, V. V. Mazurenko, and D. F. McMorrow, Phys. Rev. B **93**, 174118 (2016).

[20] C. Hahn, G. de Loubens, V. V. Naletov, J. B. Youssef, O. Klein and M. Viret, Europhys. Lett. **108**, 57005 (2014).

Chapter II

[1] "*Handbook of Spin Transport and Magnetism*", 2nd edition, Eds.: E. Y. Tsymbal, I. Žutić (Chapman and Hall/CRC).

[2] V. Baltz et al. Rev. Mod. Phys. 90, 015005 (2018).

[3] C. Wang et al. Phys. Rev. B 92, 115136 (2015).

[4] H. Seinige et al. Phys. Rev. 94, 214434 (2016).

[5] M. Williamson et al. Phys. Rev. B 97, 134431 (2018).

[6] G. Cao, Y. Xin, C. S. Alexander, J. E. Crow, P. Schlottmann, M. K. Crawford, R. L. Harlow, and W. Marshall, Phys. Rev. B **66**, 214412 (2002).

[7] M. J. Kirton and M. J. Uren, Advances in Physics 38, 367 (1989).

[8] B. M. Wilamowski and J. D. Irwin, The Industrial Electronics Handbook (CRC, Boca Raton, 2011) Chap. 11, pp. 11-4–11-6, 1st ed.

[9] D. M. Liou, J. Gong, and C. C. Chen, Jpn. J. Appl. Phys. 29, 7 (1990).

[10] L. K. J. Vandamme, IEEE Trans. Trans. Electron Devices 41, 11 (1994).

Chapter III

[1] J. C. Slonczewski, *J. Magn. Magn. Mater.* **159,** L1–L7 (1996).

[2] L. Berger, *Phys. Rev. B* **54,** 9353–9358 (1996).

[3] M. Tsoi, A. G. M. Jansen, J. Bass, W.-C. Chiang, M. Seck, V. Tsoi, and P. Wyder, *Phys. Rev. Lett.* **80,** 4281–4284 (1998).

[4] F. Matsukura, Y. Tokura, and H. Ohno, *Nat. Nanotechnol.* **10,** 209–220 (2015).

[5] W.-G. Wang, M. Li, S. Hageman, and C. L. Chien, *Nat. Mater.* **11,** 64–68 (2011).

[6] S. Kanai, M. Yamanouchi, S. Ikeda, Y. Nakatani, F. Matsukura, and H. Ohno, *Appl. Phys. Lett.* **101,** 122403 (2012).

[7] A. Okada, S. Kanai, M. Yamanouchi, S. Ikeda, F. Matsukura, and H. Ohno, *Appl. Phys. Lett.* **105,** 052415 (2014).

[8] J. Zhu, J. A. Katin, G. E. Rowlands, Y.-J. Chen, Z. Duan, J. G. Alzate, P. Upadhyaya, J. Langer, P. Kahlili Amiri, K. L. Wang, and I. N. Krivorotov, *Phys. Rev. Lett.* **108,** 197203 (2012).

[9] K. Miura, S. Yabuuchi, M. Yamada, M. Ichimura, B. Rana, S. Ogawa, H. Takahashi, Y. Fukuma, and Y. Otani, *Sci. Rep.* **7**, 42511 (2017);

[10] H. Almasi, M. Xu, Y. Xu, T. Newhouse-Illige, and W. G. Wang, *Appl. Phys. Lett.* **109,** 032401 (2016)

[11] K. Nakamura, R. Shimabukuro, Y. Fujiwara, T. Akiyama, T. Ito, and A. J. Freeman, *Phys. Rev. Lett.* **102,** 187201 (2009).

[12] M. Tsujikawa, T. Oda, *Phys. Rev. Lett.* **102,** 247203 (2009).

[13] C.-G. Duan, J. P. Velev, R. F. Sabirianov, Z. Zhu, J. Chu. S. S. Jaswal, and E. Y. Tsymbal, *Phys. Rev. Lett.* **101,** 137201 (2008).

[14] A. A. Tulapurkar, Y. Suzuki, A. Fukushima, H. Kubota, H. Maehara, K. Tsunekawa, D. D. Djayaprawira, N. Watanabe, and S. Yuasa, *Nature* **438,** 339–342 (2005).

[15] J. C. Sankey, P. M Braganca, A. G. F. Garcia, I. N. Krivorotov, R. A. Buhrman, and D. C. Ralph, *Phys. Rev. Lett.* **96,** 227601 (2006).

[16] T. Staudacher and M. Tsoi, *J. Appl. Phys.* **109,** 07C912 (2011).

[17] H. Seinige, C. Wang, and M. Tsoi, *J. of Appl. Phys.* **117,** 17C507 (2015).

[18] L. Xu and S. Zhang, *J. Appl. Phys.* **111,** 07C501 (2012).

[19] S. E. Barnes, J. Ieda, and S. Maekawa, *Sci. Rep.* **4,** 4105 (2014).

[20] D. Odkhuu, W. S. Yun, S. H. Rhim, S. C. Hong, *J. Magn. Magn. Mater*. **414,** 126 (2016).

[21] U. Bauer, L. Yao, A. J. Tan, P. Agrawal, S. Emori, H. L Tuller, S. van Dijken, and G. S. D. Beach, *Nat. Mater.* **14,** 174–181 (2014).

[22] A. Rajanikanth, T. Hauet, F. Montaigne, S. Mangin, and S. Andrieu, *Appl. Phys. Lett.* **103,** 062402 (2013).

[23] J. Zhang, P. V. Lukashev, S. S. Jaswal, and E. Y. Tsymbal, *Phys. Rev. B* **96,** 014435 (2017).

Chapter IV

[1] F. Matsukura, Y. Tokura, and H. Ohno, *Nature Nanotechnology* **10,** 209–220 (2015).

[2] S. Kanai, M. Yamanouchi, S. Ikeda, Y. Nakatani, F. Matsukura, and H. Ohno, *Applied Physics Letters* **101,** 122403(2012).

[3] A. Okada, S. Kanai, M. Yamanouchi, S. Ikeda, F. Matsukura, and H. Ohno, *Applied Physics Letters* **105,** 052415 (2014).

[4] J. Zhu, J. A. Katine, G. E. Rowlands, Y. J. Chen, Z. Duan, J. G. Alzate, P. Upadhyaya, J. Langer, P. K. Amiri, K. L. Wang, and I. N. Krivorotov, *Physical Review Letters* **108,** 197203 (2012).

[5] K. Miura, *et al., Scientific Reports.* **7**, 42511 (2017).

[6] T. Nozaki, et al., *App. Phys. Lett.* **96,** 022506 (2010).

[7] W.-G. Wang, et al., *Nat. Mater.* **11,** (2012).

[8] J. G. Alzate, et al., *Proc. 2012 IEEE IEDM* 13384152 (2012).

[9] Y. Shiota, et al., *App. Phys. Express* **2,** (2009).

[10] T. Maruyama, et al., *Nat. Nanotechnol.* **4,** (2009).

[11] M. Endo, et al., *App. Phys. Lett.* **96,** 212503 (2010).

[12] H. Almasi, M. Xu, Y. Xu, T. Newhouse-Illige, and W. G. Wang, *Applied Physics Letters* **109,** 032401 (2016)

[13] H. Zhao, A. Lyle, Y. Zhang, P.K Amiri, G. Rowlands, Z. Zeng, J. Katine, H. Jiang, K. Galatsis, K. L. Wang, I. N. Krivorotov, and J.-P. Wang, *Journal of Applied Physics* **109,** 07C720 (2011)

[14] A. A. Tulapurkar, Y. Suzuki, A. Fukushima, H. Kubota, H. Maehara, K. Tsunekawa, D. D. Djayaprawira, N. Watanabe, and S. Yuasa, *Nature* **438,** 339–342 (2005).

[15] J. C. Sankey, P. M. Braganca, A. G. F. Garcia, I. N. Krivorotov, R. A. Buhrman, and D.C. Ralph, *Physical Review Letters***96,**227601(2006).

[16] T. Staudacher and M. Tsoi, *Journal of Applied Physics* **109,** 07C912(2011).

[17] H. Seinige, C. Wang, and M. Tsoi, *Journal of Applied Physics* **117,** 17C507 (2015).

[18] A. Helmer, S. Cornelissen, T. Devolder, J.-V. Kim, W. van Roy, L. Lagae, and C. Chappert, *Physical Review B* **81,** 094416 (2010).

[19] L. Xu and S. Zhang, *Journal of Applied Physics* **111,** 07C501 (2012).

[20] S. E. Barnes, J. Ieda, and S. Maekawa, *Scientific Reports* **4,** 4105 (2014).

[21] J. C. Sankey, *et al.*, *Nature Physics* **4,** 67–71 (2008)

[22] H. Kubota, *et al.*, *Nature Physics* **4,** 37–41 (2008)

Chapter V

[1] Y. Kojima, *Scientific Reports of the Research Institutes of Tohoku University* **A6**, 614 (1954).

[2] V. G. Harris, A. Geiler, Y, Chen, S. D. Yoon, M. Wu, A. Yang, Z. Chen, P. He, P. V. Parimi, X. Zuo, C. E. Patton, M. Abe, O. Acher, C. Vittoria, *J. of Magn. And Magn. Mater.* **321**, 2035 (2009).

[3] G. P. Rodrigue, *Proc. of the IEEE* **76**, 2 (1988)

[4] M. Y. Song, J. G. Lin, M. G. Samant, and S. S. P. Parkin, *IEEE Trans. on Magn.* **50**, 11 (2014).

[5] Z. C. Huang, X. F. Hu, Y. X. Xu, Y. Zhai, Y. B. Xu, J. Wu, and H. R. Zhai, *J. of Appl. Phys.* **111**, 07C108 (2012).

[6] J. R. Fermin, A. Azevedo, F. M. de Aguiar, B. Li, and S. M. Rezende, *J. of Appl. Phys.* **85**, 10 (1999).

[7] J.-F. Lin, J. Wu, J. Zhu, Z. Mao, A. H. Said, B. M. Leu, J. Cheng, Y. Uwatoko, C. Jin, and J. Zhou, *Sci. Rep.* **4**, 6282 (2014).

[8] J. G. Lin, M. Y. Song, J. W. Lin M. G. Samant, and S. S. P. Parkin, *IEEE Trans. on Magn.* **49**, 7 (2013).

[9] L. R. Bickford Jr., *Phys. Rev.* **75**, 1298 (1949).

[10] L. R. Bickford Jr., *Phys. Rev.* **76**, 137 (1949).

[11] L. R. Bickford Jr., *Phys. Rev.* **78**, 4 (1950).

[12] N. Bloembergen, *Proc. of the IRE*, **44**, 10 (1956).

[13] N. Bloembergen and R. W. Damon, *Phys. Rev.* **85**, 699 (1952).

[14] L. G. van Uiter, *Proc. of the IRE*, **44**, 10 (1956).

[15] R. W. Damon, *Rev. Mod. Phys.* **25**, 239 (1953).

VITA

Morgan Williamson was born and raised in Austin, TX. He earned a Bachelor of Science in physics from The University of Texas at Austin in 2014 while working in Dr. E.L. Florin's biophysics lab investigating fission yeast cytoplasm mechanics. Also at UT Austin, in 2016 he completed his Master of Arts in physics in Dr. Maxim Tsoi's lab studying ferromagnetic resonance in magnetic tunnel junctions. He will be graduating with a PhD in physics along with the NASCENT Nanomanufacturing portfolio in 2019. For recreation Morgan enjoys astrophotography, philosophy, hermeneutics, mythology, and spending time with his family.

Email: williamson@utexas.edu

This dissertation was typed by Morgan Cole Williamson.